Journal of Biomedical Photonics & Engineering

by Samara National Research University

Volume 2, Issue 4 (December 2016)

Editorial Board

Postal address:

39B Lukacheva st., room #301

Samara 443086, Russian Federation

Contents

Experimentally testing the role of blood vessels in the full scattering profile: solid phantom measurements

Idit Feder, Hamootal Duadi, Moti Fridman, Tamar Dreifuss, and Dror Fixler
Faculty of Engineering and the Institute of Nanotechnology and Advanced Materials, Bar Ilan University, Israel

e-mail: Dror.Fixler@biu.ac.il

Abstract. Optical methods for biomedical purposes mostly use reflected light, while few of them use the transmitted light. The blood vessels pose a challenge to these methods due to their high absorption and scattering coefficients as well as their change in size during respiration, and they are also naturally distributed in size within the body and between individuals. We suggest the full scattering profile (FSP) method in order to investigate the light at every possible exit angle. Our model of FSP successfully describes the role of the blood vessel diameter in light-tissue interaction. By means of the new point of view of FSP, we found the isobaric point, which is non-dependent on the optical properties. The uniqueness of the isobaric point is that it overcomes the shielding effect, which has known influence on the reflected light, for various vascular diameters of the same volume. We present these findings experimentally by measuring cylindrical phantoms with blood vessels in different diameters, and compare the results to our simulation results. The importance of the immunity to the shielding effect is that it allows self-calibration in clinical measurements and decreases the calibration error. In addition, by using the isobaric point we can cope with changes in blood vessel diameters and not assume microcirculation only.

Keywords: absorption, light impulse, biophotonics, medical physics.

Paper #3096 received 2016.09.15; revised manuscript received 2016.10.28; accepted for publication 2016.10.31; published online 2016.12.23. doi: 10.18287/JBPE16.02.040301

References

1. S. L. Jacques, "Optical properties of biological tissues: a review," Physics in medicine and biology 58(11), R37 (2013).
2. B. Xiong, L. Peng, X. Cao, Y. He, and E. S. Yeung, "Optical analysis of biological hydrogen sulphide: an overview of recent advancements," Analyst 140(6), 1763-1771 (2015).
3. D. I. Ellis, D. P. Cowcher, L. Ashton, S. O'Hagan, and R. Goodacre, "Illuminating disease and enlightening biomedicine: Raman spectroscopy as a diagnostic tool," Analyst 138(14), 3871-3884 (2013).
4. R. Ankri, H. Taitelbaum, and D. Fixler, "Reflected light intensity profile of two-layer tissues: phantom experiments," Journal of biomedical optics 16(8), 085001, (2011).
5. D. Fixler, and R. Ankri, "Subcutaneous gold nanorods detection with diffusion reflection measurement," Journal of biomedical optics 18(6), 061226 (2013).
6. R. A. J. Groenhuis, J. J. Ten Bosch, and H. A. Ferwerda, "Scattering and absorption of turbid materials determined from reflection measurements. 2: Measuring method and calibration," Applied optics 22(16), 2463-2467 (1983).
7. D. Jakubowski, F. Bevilacqua, S. Merritt, A. Cerussi, and B. J. Tromberg, "Quantitative absorption and scattering spectra in thick tissues using broadband diffuse optical spectroscopy," Chapter 12 in Biomedical Optical Imaging, J. G. Fujimoto, and D. L. Farkas (eds.), Oxford University Press, New York, 330-355 (2009).
8. T. H. Pham, O. Coquoz, J. B. Fishkin, E. Anderson, and B. J. Tromberg, "Broad bandwidth frequency domain instrument for quantitative tissue optical spectroscopy," Review of Scientific Instruments 71(6), 2500-2513, (2000).

9. M. Friebel, J. Helfmann, U. Netz, and M. Meinke, "Influence of oxygen saturation on the optical scattering properties of human red blood cells in the spectral range 250to2000nm," Journal of biomedical optics 14(3), 034001 (2009).
10. M. Friebel, A. Roggan, G. Müller, and M. Meinke, "Determination of optical properties of human blood in the spectral range 250to1100nm using Monte Carlo simulations with hematocrit-dependent effective scattering phase functions," Journal of biomedical optics 11(3), 034021 (2006).
11. L. Zhang, A. Shi, and H. Lu, "Determination of optical coefficients of biological tissue from a single integrating-sphere," Journal of Modern Optics 59(2), 121-125 (2012).
12. I. Feder, H. Duadi, and D. Fixler, "Experimental system of the full scattering profile of circular phantoms," Biomed. Opt. Express 6(8), 2877-2886 (2015).
13. H. Duadi, I. Feder, and D. Fixler, "Linear dependency of full scattering profile isobaric point on tissue diameter," Journal of biomedical optics 19(2), 026007 (2014).
14. H. Duadi, D. Fixler, and R. Popovtzer, "Dependence of light scattering profile in tissue on blood vessel diameter and distribution: a computer simulation study," Journal of biomedical optics 18(11), 111408 (2013).
15. H. Duadi, and D. Fixler, "Influence of multiple scattering and absorption on the full scattering profile and the isobaric point in tissue," Journal of biomedical optics 20(5), 056010 (2015).
16. I. Feder, H. Duadi, T. Dreifuss, and D. Fixler, "The influence in the full scattering profile from cylindrical tissues following changes in vessels diameter: experimental evidence for the shielding effect," Journal of biophotonics 9(10), 1001-1008 (2015).
17. L. O. Svaasand, E. J. Fiskerstrand, G. Kopstad, L. T. Norvang, E. K. Svaasand, J. S. Nelson, and M. W. Berns, "Therapeutic response during pulsed laser treatment of port-wine stains: dependence on vessel diameter and depth in dermis," Lasers in Medical Science 10(4), 235-243 (1995)."
18. H. Liu, B. Chance, A. H. Hielscher, S. L. Jacques, and F. K. Tittel, "Influence of blood vessels on the measurement of hemoglobin oxygenation as determined by time-resolved reflectance spectroscopy," Medical physics 22(8), 1209-1217 (1995).
19. S. L. Jacques, "Optical assessment of cutaneous blood volume depends on the vessel size distribution: a computer simulation study," Journal of biophotonics 3(1-2), 75-81 (2010).
20. W. Verkruysse, G. W. Lucassen, J. F. de Boer, D. J. Smithies, J. S. Nelson, and M. J. C. van Gemert, "Modelling light distributions of homogeneous versus discrete absorbers in light irradiated turbid media," Physics in Medicine and Biology 42(1), 51-65 (1997).
21. M. Firbank, E. Okada, and D. T. Delpy, "Investigation of the effect of discrete absorbers upon the measurement of blood volume with near-infrared spectroscopy," Physics in medicine and biology 42(3), 465-477 (1997).
22. A. Talsma, B. Chance, and R. Graaff, "Corrections for inhomogeneities in biological tissue caused by blood vessels," J. Opt. Soc. Am. 18(4), 932-939 (2001).
23. K. K. Tremper,"Pulse oximetry," Chest 95(4), 713-715 (1989).
24. H. Duadi, M. Nitzan, and D. Fixler, "Simulation of oxygen saturation measurement in a single blood vein," Opt. Lett. 41(18), 4312-4315 (2016).
25. M. Nitzan, S. Noach, E. Tobal, Y. Adar, Y. Miller, E. Shalom, and S. Engelberg, "Calibration-Free Pulse Oximetry Based on Two Wavelengths in the Infrared — A Preliminary Study," Sensors 14(4), 7420-7434 (2014).
26. V. V. Tuchin, A. N. Bashkatov, E. A. Genina, V. I. Kochubey, V. V. Lychagov, S. A. Portnov, N. A. Trunina, D. R. Miller, S. Cho, H. Oh, B. Shim, M. Kim, J. Oh, H. Eum, Y. Ku, D. Kim, and Y. Yang, "Finger tissue model and blood perfused skin tissue phantom," Proc. SPIE 7898, 78980Z (2011).
27. R. Ankri, H. Taitelbaum, and D. Fixler, "On Phantom experiments of the photon migration model in tissues," The Open Optics Journal 5(1), 28-32 (2011).
28. J. S. Dam, C. B. Pedersen, T. Dalgaard, P. E. Fabricius, P. Aruna, and S. Andersson-Engels, "Fiber-optic probe for noninvasive real-time determination of tissue optical properties at multiple wavelengths," Applied optics 40(7), 1155-1164 (2001).
29. I. Feder, M. Wróbel, H. Duadi, M. Jędrzejewska-Szczerska, and D. Fixler, "Experimental results of full scattering profile from finger tissue-like phantom," Biomed. Opt. Express 7(11), 4695-4701 (2016).

1 Introduction

In recent years, optical methods are very useful in the detection of various physiological states. They are noninvasive and rely on the minor changes in the optical properties during disease or in other physiological states [1-3]. Most of the optical methods for biological applications use the reflected light [4-8], while few of them use the transmitted light [9-11].

In a previous work, we presented our new system for measuring the full scattering profile (FSP) of cylindrical tissues [12]. We suggested this method of measuring the ejected light from every possible exit angle as a new point of view for light-tissue interactions. In order to investigate the influence of optical properties and blood

vessel diameters on the light scattering, we simulated the FSP of cylindrical tissues using a Monte Carlo simulation [13-15], and measured liquid and solid phantoms [16] with different reduced-scattering coefficients (μ_s') and with blood vessels in different diameters, prepared in our lab.

The main findings that we published are the isobaric point and the shielding effect in the FSP. The isobaric point is a unique point in the FSP that is independent on the optical properties of the tissue. This point, from a clinical perspective, can be a self-reference point for extracting optical properties. The angle of the isobaric point linearly depends on the tissue diameter, as we have validated both in simulation and experimentally [12, 13].

The second stage of the research focused on heterogeneous tissue-like phantoms that included blood vessels. By investigating the blood vessel diameter's influence on the FSP, we presented in a simulation as well as an experimentally, the shielding effect in the FSP. The meaning of the shielding effect is that the inner part of large vessels is not exposed to light and therefore is less effective in the determination of the optical path length.

The shielding effect, which was examined while measuring the reflected light, has been already discussed in literature by simulations [17] as well as experiments [18]. As Jacques [19] published, the shielding effect is significant proportionally to the blood vessel diameter (D) and to the blood absorption coefficient (μ_a). Verkruysse et al. [20] concluded that for $\mu_a D > 1$, the shielding effect is more significant. Hence, for tissue optical properties in near infrared (NIR) the shielding-effect does not occur under 1mm vessel diameter. Others [21] claim that it is limited to a lower vessel diameter, and the shielding effect is significant for $\mu_a D > 0.06$.

In other words, as Talsma [22] published, the apparent coefficients of blood vessels and the coefficients inside the blood vessels are the same for small values of $\mu_t D$ only (where $\mu_t = \mu_s' + \mu_a$). However, for values higher then $\mu_t D$, the apparent absorption coefficient and the apparent reduced-scattering coefficient are both smaller than the coefficients inside the blood vessels.

In a previous work, we discussed the shielding effect in the FSP of cylindrical silicon-based phantoms with blood vessels larger than 1 mm. Due to a fabrication limit, 1mm was the smallest diameter. Therefore, we are interested in obtaining smaller blood vessels in a different way, using narrowed glass capillaries (i.e. tapered capillaries) and liquid phantoms. Through this method, the glass volume remains constant in the phantom, even though the diameter is different. These tapered diameters are closer to the vascular system in human fingers.

The common method for measuring oxygen saturation in blood is pulse oximetry which is based on reflection of two wavelengths [23]. Since the optical properties of the tissue are depended on wavelength, the optical path length is different for the two wavelengths even though they advanced in the same surroundings. While the usage of nearby wavelengths, where the optical ways are similar, it is more challenging to extract the SpO_2, due to the proximity of the extinction coefficients [24]. Therefore, the use of two light sources requires calibration, thus adding an error which is too high for some clinical problems [25]. Hence, it is necessary to consider the shielding effect for each one of them respectively.

In this paper, we present our system's sensitivity to vessels of a diameter less than 1 mm. The isobaric point is still discernible in these small diameters. In addition, the prevailing investigation of the blood vessel diameter's influence on the light propagation is at the reflectance region. There we can see changes for the same blood volume that is placed in different vessel diameters, as well as at the transmission area. The uniqueness of our method is the isobaric point which is discovered to be immune to the shielding effect. We can use the isobaric point as a self-reference point for extracting optical properties in clinical applications, even though the blood vessels change their size during respiration, as they do in various physiological conditions. Therefore, it can be useful for more accurate blood perfusion measurements and blood oxygen saturation determination.

2 Preparing of phantoms

In order to simulate a skin tissue with blood vessels in different diameters, we tapered glass capillaries [26] using a glass processing unit (LZM-100, LAZERMaster) which is shown in Fig. 1. We designed the capillaries with different inner diameters per our requirements (750 μm, 600 μm and 510 μm), as shown by the CT scan images in Fig. 2.

The operation principle of the LZM-100 machine is based on pulling both ends of the capillary while heating it with a CO2 laser system. The speed and heating power are programmable and since the machine is designed to work also with fiber, its accuracy is at the sub-micron level.

For the tissue around the blood vessels, we prepared phantoms using Intralipid 20% (Lipofundin MCT/LCT 20%, B. Braun Melsungen AG, Germany) as a scattering component ($\mu_s' = 1.04\ mm^{-1}$), and Agarose powder (SeaKem, LE Agarose, Lonza, USA), in order to convert the solution into gel [27]. We injected liquid phantoms that mimic blood in their scattering and absorption properties into the capillaries. As an absorbing component we used Indian ink ($\mu_a = 1\ mm^{-1}$, $\mu_s' = 3\ mm^{-1}$).

After the capillaries were filled with the blood-like solution, they were placed in a tube (13 mm diameter), as presented in Fig. 3. Finally, the background solution was added, in order to prevent cutting of the phantom after it stabilization and thus allowing the entry of undesirable air to the sample. The volume of the inner part of the capillaries in the different tubes remains constant (5%) as the blood volume in human finger [19].

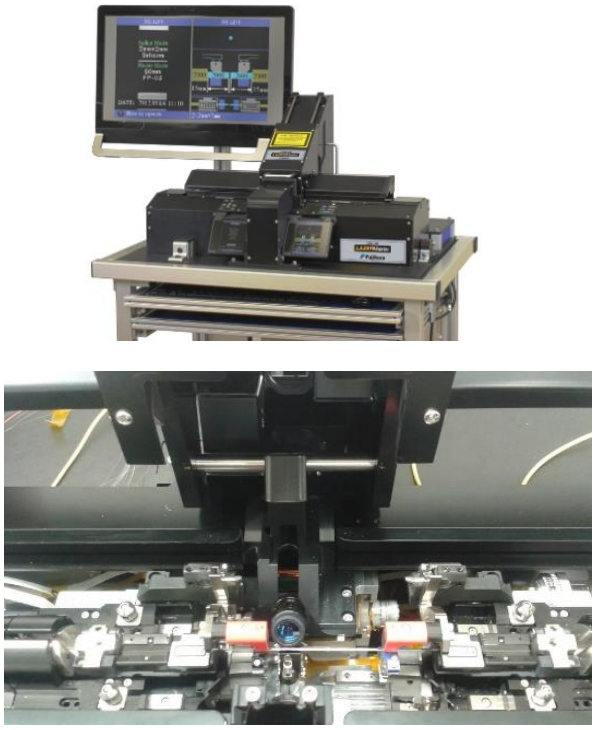

Fig. 1 (top) The LZM-100 system and (bottom) a capillary lying inside the LZM-100.

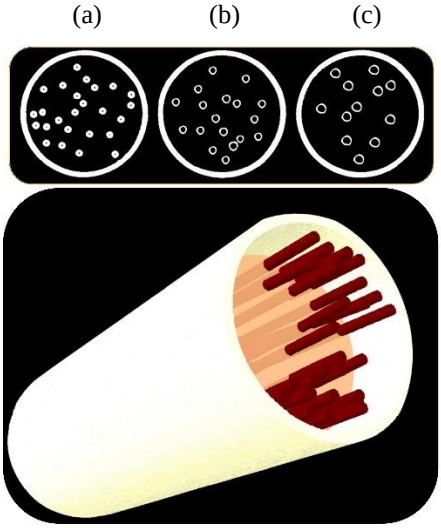

Fig. 2 CT scans of the capillaries in a 13 mm tube. Upper panel – 2D images: Tapered capillaries with inner diameter of (a) 510 µm (b) 600 µm and (c) 750 µm. Lower panel – 3D image where tapered capillaries have an inner diameter of 510 µm.

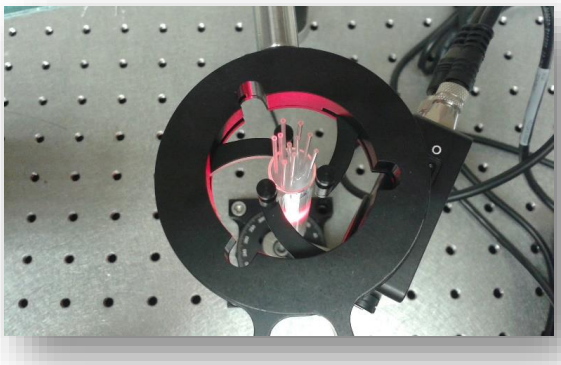

Fig. 3 Top view image of capillaries in a tube fixed in the FSP setup.

3 Optical setup description

We measured the phantoms, using our FSP optical system (Fig. 4). The set-up includes a He-Ne gas laser (Thorlabs, Newton, USA) with an excitation wavelength of λ=632.8 nm and maximum power of 5 mW. The waist of the laser beam is ω_0=0.63 mm. We use a portable fixed gain silicon detector as a photo detector (PD). The PD has an active area of 0.8 mm^2 and it is placed on a rotation stage in order to enable the full scattering profile measurements. The stage can be rotated around a tube with an accuracy of 1°. The voltage is measured every 5 degrees, when 0° is the full transmission and 180° is the full reflection. It should be noted that the light intensities from 145° to 180° were not measured, because of a system limitation; the PD's size blocks the laser. For each phantom, we repeated the measurements for different locations of the capillaries, in relation to the light source. The standard deviation due to capillaries' placement is presented in the results.

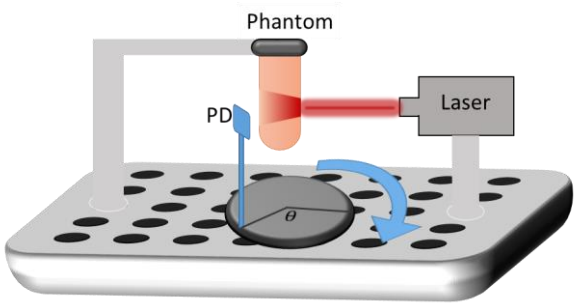

Fig. 4 A scheme of the FSP optical setup.

4 Results

We measured solid phantoms with liquid filled capillaries inside that mimic cylindrical tissues with blood vessels, where the liquid volume mimicking the blood is kept constant. The background solution that we measured has a smaller reduced scattering coefficient than the capillaries. In addition, the capillaries contain absorption components. In this phantom model, we are

able to discern different light intensities throughout the full scattering profile, even though the volume of the components is the same. Our system has the ability to distinguish between different diameters smaller than 1mm. The distribution of the blood volume inside capillaries with different diameters causes the light to advance in different ways, in accordance to the effective optical properties.

The FSPs of the measured phantoms are presented in Fig. 5. The highest curve represents a phantom that was used as a background tissue, without capillaries, that has a reduced scattering coefficient characteristic to human skin tissue ($\mu_s' = 1.04\, mm^{-1}$) [28]. The other profiles belong to phantoms with capillaries inside, in different diameters: 750 μm and 510 μm, while the volume of the

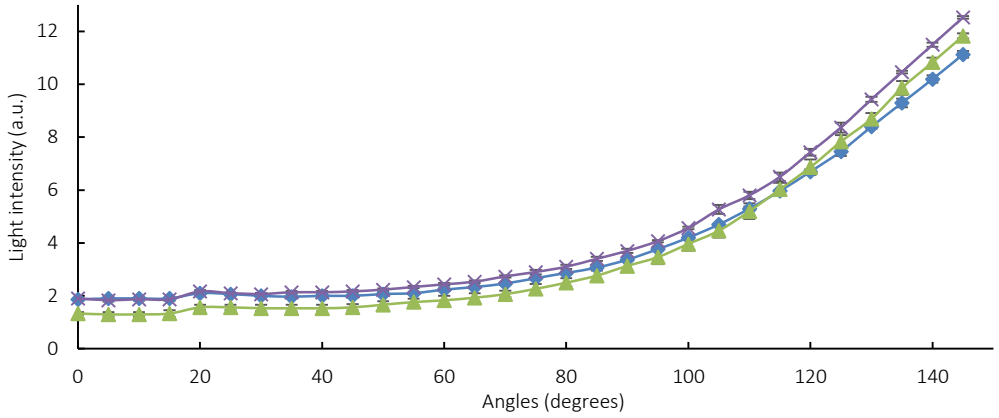

Fig. 5 Full scattering profiles of phantoms in a 13 mm tube: a background phantom (μ_s'=1.04 mm^{-1}) without capillaries (x) and phantoms with capillaries in different diameters (triangles and diamonds for 750 μm and 510 μm). The capillaries contain a solution (μ_s'=1.04 mm^{-1}, μ_a=3 mm^{-1}) in the same volume for each sample.

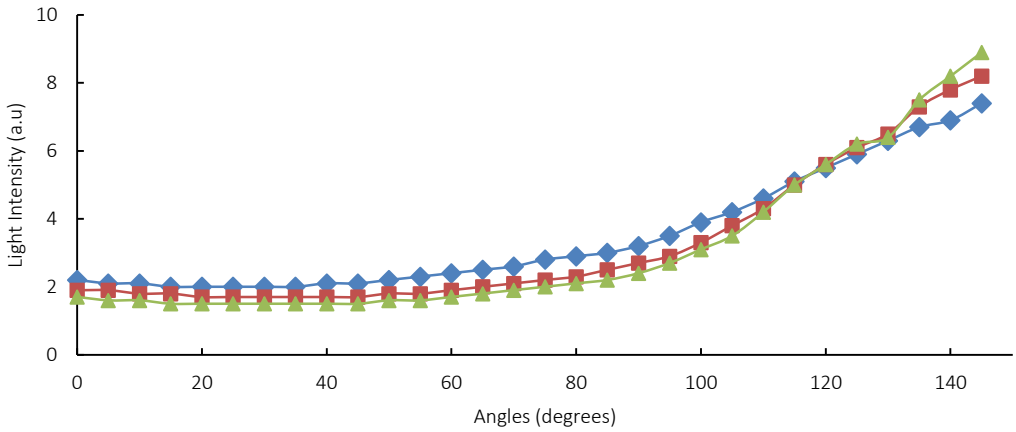

Fig. 6 Full scattering profiles of liquid homogenous phantoms with different reduced scattering coefficients (diamonds, squares and triangles in respect to 1, 1.6 and 2.6 mm^{-1}) in a tube of 13 mm diameter.

blood-like phantom in the capillaries is kept constant (5%). The isobaric point appears at 115 degrees; at this point a substitution between the curves occurs. The background has no value common with the isobaric point due to the lack of absorbing components within it. The standard deviation is in average lower than 1.5%.

These results correspond with our previous work that presented a linear dependence between the angle of the isobaric point and the cylindrical tissue diameter. There, the isobaric point of 13 mm homogenous phantoms in different reduced scattering coefficients appeared at 115°, as shown in Fig. 6. The standard deviation is in average lower than 1.5% also.

The finding of the isobaric point means that the total reduced scattering coefficient of each one of the phantoms is actually different. The measurements of different phantom profiles, that have the same volume of solution in the capillaries and the same background solution, present the shielding effect. While the shielding effect is known as an effect that depends on the absorption of the medium [18-20], in this experiment we mimic blood that has high absorption and also high scattering, and we see the influence of the scattering as well.

In addition, we measured phantoms with constant reduced scattering coefficient, inside the capillaries as

well as out of them, in addition to the absorption components in the capillaries. The FSPs of these phantoms are presented in Fig. 7 in comparison to the first phantoms. As we expected, the intensities of the FSPs are lower than the FSP of similar phantoms with higher scattering in the capillaries, as a result of the light absorption that is more significant without the high reduced scattering coefficient. The higher standard deviation at the attenuated profiles (1.8%), in combination with the subtle change that is expected between the profiles, make it difficult to determine that the absorption alone maintains the profile's format.

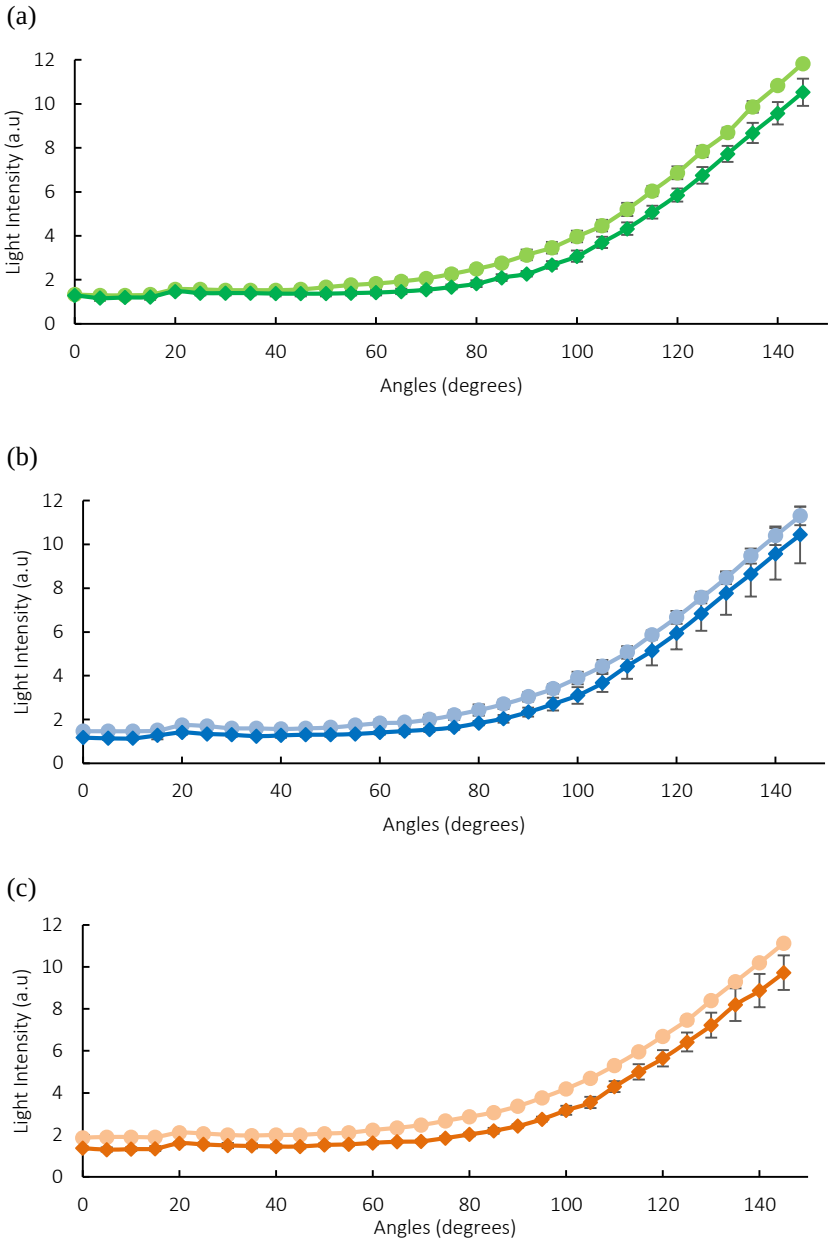

Fig. 7 A distinction of absorption influence within capillaries in different diameters (a) 750 µm (b) 600 µm and (c) 510 µm. FSP of phantom with a lower reduced scattering coefficient in the capillaries (μ_s'=1.04 mm^{-1}), which is the same as the background, and absorption coefficient of μ_a=1mm^{-1} (in diamonds) compared to FSP of phantom with a higher scattering coefficient (μ_s'=3 mm^{-1}), which is the same as the blood, while the absorption coefficient is the same (in circles).

5 Discussion

In the results that we presented above, the order of the profiles in the transmission area (the low angles) is arranged according thus: as the diameter of the capillaries increases, the light intensity decreases (Fig. 8), while in the reflectance area (the high angles) the opposite is true.

In previous experiments [15] we manufactured silicon-based phantoms with blood vessels inside with different diameters larger then 1mm (the blood volume remained constant). The obtained STD was smaller than 7%. At the transmission range we could not distinguish between the FSPs of the phantoms, as presented in

Fig. 9, whereas with the new phantoms with the glass capillaries, we have the ability to discern the changes in the transmission area. However, in the reflection range we obtained the same tendency in both models, above 1mm and under 1 mm – the reflection decreases as the vessel diameter decreases, in accordance with the shielding effect.

Fig. 8 Tendency of profiles in transmission and reflection area in accordance to blood vessel diameter.

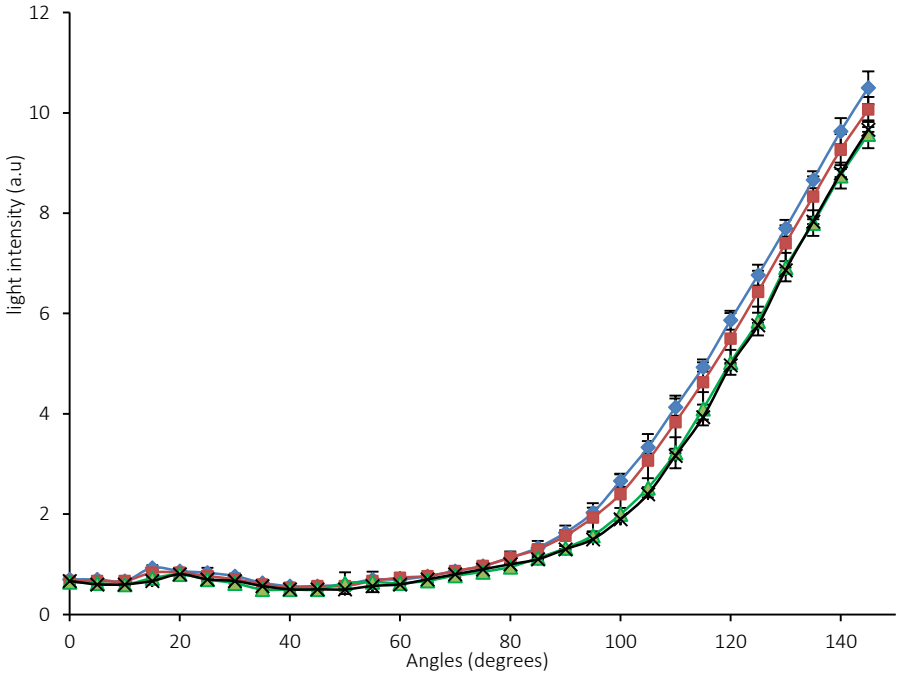

Fig. 9 Full scattering profiles of silicon-based phantoms, 10 mm diameter. With constant blood volume in different blood vessel diameter (diamonds, squares, triangles and x for 1.6 mm 1.3 mm, 1.1 mm and 1 mm diameter, respectively). The larger the diameter is, the higher the obtained intensity is.

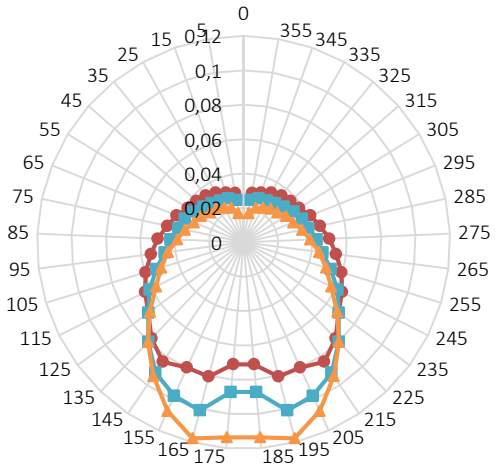

Fig. 10 Radar presentation for simulation results of the full scattering profile of tissue with constant blood volume in vessels in different diameter (circles, squares and triangles indicate 5 vessels of 1mm diameter, 40 vessels of 502 μm diameter and 200 vessels of 159 μm diameter, respectively). Light intensity value (a.u.) is presented at each angle (0 to 360°), starts at the center of the chart and ends on the outer ring. The isobaric point appears at 125°. The transmission increases as vessel size increases while the reflection decreases as vessel diameter increases.

In our simulation, the order of the profiles was in a reversed tendency, as shown in Fig.10. It is important to notice that the scattering definitions in the simulation were higher (4 mm^{-1}), while lower values were determined for the absorption (0.04 mm^{-1}), due to the higher wavelength (850 nm). In the experiment the impact of the absorption was displayed more dominantly and therefore the profiles' order was inverse. Since the absorption causes the attenuation of the whole profiles' intensities, as we showed in a previous work [12], we can expect to obtain more attenuation for smaller vessels with stronger effectivity, as a result of the shielding effect. Therefore, the intensities in the reflectance area increase as the vessel diameter increases. The smaller the vessel is, the stronger the obtained effective absorption, hence the effective scattering coefficient of the whole phantom is decreased. However, in the transmission area we obtain an opposite gradation for the curves.

According to our previous research [12,29], based on homogenous phantoms with different reduced scattering coefficients, it can be concluded that the curves' gradation is in accordance with the tendency of the reduced scattering coefficient, as shown in Fig. 11. In the transmission range (low angles) the light intensity of higher μ_s' is weaker, while in the reflectance range (high angles), for higher μ_s' the intensity is stronger. The many scattering events prevent photons from advancing toward the transmission region and cause them to reach the reflectance area. On the other hand, for lower μ_s' the opposite occurs, because less scattering events occur. Hence, we can conclude in this capillaries experiment, that larger diameter of capillaries yields a medium with a higher total reduced scattering coefficient than the smaller diameter, due to the less effective absorption there. However, with smaller capillaries the absorption is more expressed.

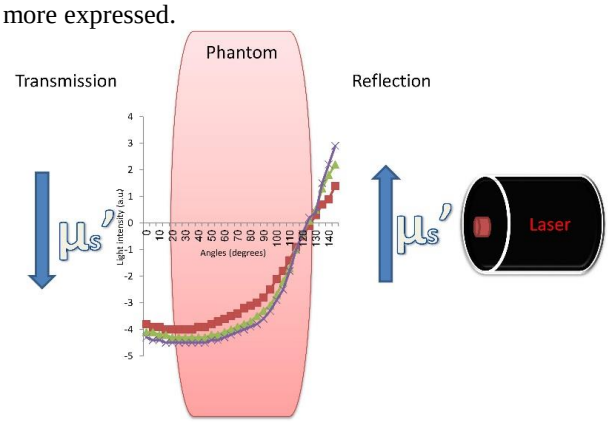

Fig. 11 The trend of the reduced scattering coefficient in accordance with the range.

6 Conclusion

In this research, we present the role of the blood vessel diameter in light-tissue interactions using our model of FSP. We prepared cylindrical phantoms with glass capillaries in different diameters (smaller than 1 mm), and they were filled with blood-like solution. The FSP that we measured experimentally corresponded with our simulation results. We found the isobaric point, which is non-dependent on the optical properties. The angle where the isobaric point appeared in the experiment is 115^0, while in the simulation it appeared at higher angle, probably due to the assumptions which made for the simplification of the simulation. The results that we present here validate that the isobaric point overcomes the shielding effect. The importance of this finding is that this unique point can be useful as a reference point for clinical purposes. For example, it can be implemented in various optical methods such as NIR spectroscopy and PPG experiments, and thus can improve analyzing oxygen saturation values, blood perfusion and blood pressure. In addition, it is relevant as well to the development and promotion of imaging and tomography methods, owing to the new viewpoint of FSP. On the one hand, the FSP method has the ability to distinguish between minor changes in the blood vessel diameter, and on the other hand it has the uniqueness of the fixed isobaric point, serving as a self-reference point.

Two-dimensional fractal analysis of retinal tissue of healthy and diabetic eyes with optical coherence tomography

Wei Gao[1]*, Delia Cabrera DeBuc[2], Valery P. Zakharov[3], Erika Tatrai[4], Gabor M. Somfai[4], Oleg O. Myakinin[3], Ivan A. Bratchenko[3], Dmitry N. Artemyev[3], and Dmitry V. Kornilin[3]

[1] School of Safety Engineering, Ningbo University of Technology, China
[2] Bascom Palmer Eye Institute, University of Miami, Florida, United States of America
[3] Department of Laser and Biotechnical Systems, Samara National Research University, Russian Federation
[4] Department of Ophthalmology, Semmelweis University, Budapest, Hungary

* **e-mail**: gwei@ustc.edu

Abstract. In the ophthalmic research, the measurement of the retinal thickness is usually employed for characterizing the structural changes of the retinal tissue. However, changes in the fractal dimension (FD) may provide additional information regarding the structure of the retinal layers and their early damage in ocular diseases. In the present paper, we investigated the possibility of detecting changes in the structure of the cellular layers of the retina by applying a two-dimensional fractal analysis to optical coherence tomography (OCT) images. OCT images were obtained from diabetic patients without retinopathy (DM, n = 38 eyes) and with mild diabetic retinopathy (MDR, n = 43 eyes) as well as in healthy subjects (Controls, n = 74 eyes). The two-dimensional fractal dimension was calculated using the differentiate box counting methodology. We evaluated the usefulness of quantifying the fractal dimension of layered structures in the detection of retinal damage. Generalized estimating equations considering within-subject inter-eye relations were used to test for differences between the groups. An adjusted p-value of <0.001 was considered statistically significant. Receiver operating characteristic (ROC) curves were constructed to describe the ability of the fractal dimension to discriminate between the eyes of DM, MDR, and healthy eyes. Lower values of the fractal dimension were observed in all layers in the MDR eyes compared with controls except in the inner nuclear layer (INL). Lower values of the fractal dimension were also found in all layers in the MDR eyes compared with DM eyes. The highest area under receiver operating characteristic curve (AUROC) values estimated for the fractal dimension were observed for the outer plexiform layer (OPL) and outer segment photoreceptors (OS) when comparing MDR eyes with controls. The highest AUROC value estimated for the fractal dimension were also observed for the retinal nerve fiber layer (RNFL) and OS when comparing MDR eyes with DM eyes. Our results suggest that fractal dimension of the intraretinal layers may provide useful information to differentiate pathological from healthy eyes. Further research is warranted to determine how this approach may be used to aid diagnosis of retinal neurodegeneration at the early stage.

Keywords: optical coherence tomography; retina; diabetic retinopathy; fractal analysis, differentiate box counting.

Paper #3114 received 2016.11.09; accepted for publication 2016.12.30; published online 2016.12.31. doi: 10.18287/JBPE16.02.040302

References

1. D. Huang, E. A. Swanson, C. P. Lin, J. S. Schuman, W. G. Stinson, W. Chang, M. R. Hee, T. Flotte, K. Gregory, C. A. Puliafito, and J. G. Fujimoto, "Optical coherence tomography," Science 254(5035), 1178-1181 (1991).
2. D. C. DeBuc, and G. M. Somfai, "Early detection of retinal thickness changes in diabetes using optical coherence tomography," Medical Science Monitor 16(3), Mt15-21 (2010).
3. E. Tatrai, M. Simo, A. IIjicsov, J. Nemeth, D. C. DeBuc, and G. M. Somfai, "In vivo evaluation of retinal neurodegeneration in patients with multiple sclerosis," PLoS One 7(1) e30922 (2012).
4. D. C. DeBuc, "Novel methods and diagnostic tools in diabetic retinopathy," Retinal Physician 12, 22-27 (2015).
5. G. M. Somfai, E. Tatrai, L. Laurik, B. E. Varga, V. Olvedy, H. Jiang, J. H. Wang, W. E. Smiddy, A. Somogyi, and D. C. DeBuc, "Automated classifiers for early detection and diagnosis of retinopathy in diabetic eyes," BMC Bioinformatics 15(1), 106 (2014).
6. G. M. Somfai, E. Tatrai, L. Laurik, B. E. Varga, V. Olvedy, W. E. Smiddy, R. Tchitnga, A. Somogyi, and D. C. DeBuc, "Fractal-based analysis of optical coherence tomography data to quantify retinal tissue damage," BMC Bioinformatics 15, 295 (2014).
7. D. C. DeBuc, E. Tatrai, L. Laurik, B. E. Varga, V. Olvedy, A. Somogyi, W. E. Smiddy, and G. M. Somfai, "Identifying local structural and optical derangement in the neural retina of individuals with type 1 diabetes," Journal of Clinical and Experimental Ophthalmology 4(4) 1000289 (2013).
8. U. H. Schaudig, C. Glaefke, F. Scholz, and G. Richard, "Optical coherence tomography for retinal thickness measurement in diabetic patients without clinically significant macular edema," Ophthalmic Surgery Lasers 31(3), 182-186 (2000).
9. T. Oshitari, K. Hanawa, and E. Adachi-Usami, "Changes of macular and RNFL thicknesses measured by Stratus OCT in patients with early stage diabetes," Eye (London) 23(4), 884-889 (2009).
10. B. Asefzadeh, B. M. Fisch, C. E. Parenteau, and A. A. Cavallerano, "Macular thickness and systemic markers for diabetes in individuals with no or mild diabetic retinopathy," Clinical & Experimental Ophthalmology 36(5), 455-463 (2008).
11. W. Goebel, and T. Kretzchmar-Gross, "Retinal thickness in diabetic retinopathy: a study using optical coherence tomography (OCT)," Retina 22(6), 759-767 (2002).
12. N. M. Bressler, A. R. Edwards, A. N. Antoszyk, R. W. Beck, D. J. Browning, A. P. Ciardella, R. P. Danis, M. J. Elman, S. M. Friedman, A. R. Glassman, J. G. Gross, H. K. Li, T. J. Murtha, T. W. Stone, and J. K. Sun, "Retinal thickness on Stratus optical coherence tomography in people with diabetes and minimal or no diabetic retinopathy," American Journal of Ophthalmology 145(5), 894-901 (2008).
13. P. G. H. Clarke, "Developmental cell death: morphological diversity and multiple mechanisms," Anatomy and Embryology 181(3) 195-213 (1990).
14. C. D. M. Fletcher (ed.), Diagnostic histopathology of tumors, 2nd. ed., Churchill Livingstone, London (2000). ISBN: 978-0-443-07992-4.
15. G. M. Somfai, H. M. Salinas, C. A. Puliafito, and D. C. Fernandez, "Evaluation of potential image acquisition pitfalls during optical coherence tomography and their influence on retinal image segmentation," Journal of Biomedical Optics 12(4), 041209 (2007).
16. D. C. DeBuc, System and method for early detection of diabetic retinopathy using optical coherence tomography. U.S. Patent WO2010080576 (2010).
17. D. C. DeBuc, H. M. Salinas, and C. A. Puliafito, "Automated detection of retinal layer structures on optical coherence tomography images," Optics Express 13(25), 10200-10216 (2005).
18. C. Flueraru, D. P. Popescu, Y. Mao, S. Chang, and M. G. Sowa, "Added soft tissue contrast using signal attenuation and the fractal dimension for optical coherence tomography images of porcine arterial tissue," Physics in Medicine and Biology 55(8), 2317-2331 (2010).
19. A. C. Sullivan, J. P. Hunt, and A. L. Oldenburg, "Fractal analysis for classification of breast carcinoma in optical coherence tomography," Journal of Biomedical Optics 16(6), 066010 (2011).
20. W. Gao, Improving the quantitative assessment of intraretinal features by determining both structural and optical properties of the retinal tissue with optical coherence tomography, Ph.D thesis, University of Miami (2012).
21. M. Hasegawa, J. Liu, K. Okuda, and M. Nunobiki, "Calculation of the fractal dimensions of machined surface profiles," Wear 192(1-2), 40-45 (1996).
22. N. Sarkar, and B. B. Chaudhuri, "An efficient approach to estimate fractal dimension of textural images," Pattern Recognition 25(9), 1035-1041 (1992).
23. J. Li, Q. Du, and C. Sun, "An improved box-counting method for image fractal dimension estimation," Pattern Recognition 42(11), 2460-2469 (2009).

24. A. J. Barber, E., Lieth, S. A. Khin, D. A. Antonetti, A. G. Buchanan, and T. W. Gardner, "Neural apoptosis in the retina during experimental and human diabetes. Early onset and effect of insulin," The Journal of Clinical Investigation 102 (4), 783-791 (1998).
25. S. H. Park, J. W. Park, S. J. Park, K. Y. Kim, J. W. Chung, M. H. Chun, and S. J. Oh, "Apoptotic death of photoreceptors in the streptozotocin-induced diabetic rat retina," Diabetologia 46(9), 1260-1268 (2003).
26. E. Rungger-Brandle, A. A. Dosso, and P. M. Leuenberger, "Glial reactivity, an early feature of diabetic retinopathy," Investigative Ophthalmology and Visual Science 41(7), 1971-1980 (2000).
27. X. X. Zeng, Y. K. Ng, and E. A. Ling, "Neuronal and microglial response in the retina of streptozotocin-induced diabetic rats," Visual Neuroscience 17(3), 463-471 (2000).
28. A. J. Barber, D. A. Antonetti, T. S. Kern, C. E. N. Reiter, R. S. Soans, J. K. Krady, S. W. Levison, T. W. Gardner, and S. K. Bronson, "The Ins2^{Akita} mouse as a model of early retinal complications in diabetes," Investigative Ophthalmology and Visual Science 46(6), 2210-2218 (2005).
29. B. J. Lujan, A. Roorda, J. A. Croskrey, A. M. Dubis, R. F. Cooper, J. K. Bayabo, J. L. Duncan, B. J. Antony, J. Caroll, "Directional optical coherence tomography provides accurate outer nuclear layer and Henle fiber layer measurements," Retina 35(8), 1511-1520 (2015).
30. T. Otani, Y. Yamaguchi, and S. Kishi, "Improved visualization of Henle fiber layer by changing the measurement beam angle on optical coherence tomography," Retina 31(3), 497-501 (2011).
31. R. Akshikar, M. Richardson, R. Crosby-Nwaobi, R., A. Abdelhay, S. Sivaprasad, S. Heng, "Retinal neuronal changes in people with diabetes," Investigative Ophthalmology and Visual Science 53, 2852 (2012).
32. A. Verma, P. K. Rani, R. Raman, S. S. Pal, G. Laxmi, M. Gupta, C. Sahu, K. Vaitheeswaran, and T. Sharma, "Is neuronal dysfunction an early sign of diabetic retinopathy? Microperimetry and spectral domain optical coherence tomography (SD-OCT) study in individuals with diabetes, but no diabetic retinopathy," Eye (London) 23(9), 1824-1830 (2009).
33. P. M. Martin, P. Roon, T. K. Van Ells, V. Ganapathy, and S. B. Smith, "Death of retinal neurons in streptozotocin-induced diabetic mice," Investigative Ophthalmology and Visual Science 45(9), 3330-3336 (2004).
34. G. Liew, J. J. Wang, P. Mitchell, T. Y. Wong, "Retinal vascular imaging: a new tool in microvascular disease research," Circulation Cardiovascular imaging 1(2), 156–161 (2008).
35. M. Hasegawa, J. Liu, K. Okuda, M. Nunobiki, "Calculation of the fractal dimensions of machined surface profiles," Wear 192(1), 40–45 (1996).

1 Introduction

Optical coherence tomography is an optical imaging modality that provides high-resolution, cross-sectional images of biological tissue in a non-invasive manner [1]. Notably, the OCT technology has been widely utilized to detect retinal diseases in Ophthalmology. By employing the OCT technique, the thickness and volume measurements of the retinal tissue can be obtained from OCT scans. Particularly, the structural alterations revealed by changes in thickness and volume of the cellular layers of the retina can be measured to characterize the neurodegeneration in patients with diabetes [2-7]. The most significant retinal pathology caused by diabetes is diabetic retinopathy (DR), which is characterized by blood vessel damage and neurodegenerative changes.

The quantification of the thickness measurement of various cellular layers of the retina with OCT has helped to assess treatment efficacy and identify potential markers for monitoring the progression of DR [8-12]. However, in biology and medicine, the shapes of structures such as molecules, cells, tissues, and organs also play a significant role in the diagnosis of diseased retinal tissue [13-14]. Out of the various structural parameters, the fractal dimension can be capable of revealing differences and irregularities in these structures. Quantitative measurements of the fractal dimension could be an effective approach to discriminate diseased tissue from healthy tissue. Therefore, the structural changes revealed by changes in fractal dimension may provide further information regarding cellular layers and early damage in ocular diseases. The abnormal retinal tissue could be detected by performing fractal analysis for particular cellular structures visualized in OCT images. Thus, fractal analysis of OCT images could provide a useful diagnostic methodology to identify diseased tissue.

In this study, OCT images were obtained from diabetic and normal healthy subjects to investigate the possibility of OCT to detect structural changes in the retina by quantifying the two-dimensional fractal dimension of its layered structures.

2 Materials and Methodology

2.1 Data Collection

The data collection included participants recruited under a study sponsored by the Juvenile Diabetes Research Foundation (JDRF). The Institutional Review Board of each institution (Bascom Palmer Eye Institute at University of Miami, FL, USA and Semmelweis University, Budapest, Hungary) involved in the study approved the study protocol. The research adhered to the tenets outlined in the Declaration of Helsinki. Informed consent was obtained from each subject. OCT examination was performed in healthy and diabetic eyes

with and without retinopathy. Once the subject was enrolled in the study, one visit was required to perform a comprehensive eye examination including the following assessments: best-corrected visual acuity, intraocular pressure (using a Goldmann tonometer) and seven standard field stereoscopic fundus photos. Also, hemoglobin A1c test was required at this visit for diabetic patients with no past glycemic control. No additional tests were needed after this first visit or during the time the study was completed. Inclusion

Table 1 Characteristics of the study participants.

Characteristic	Controls	DM	MDR
Number of Participants	41	29	29
Number of Eyes	74	38	43
Age (years, mean ± SD)	34 ± 12	35 ± 10	43 ± 17
Female, N (% total eyes)	52 (70%)	20 (53%)	21 (49%)
Race (% Caucasian)	100	100	91
Hemoglobin A1c level (%)	-	7.20 ± 0.90	8.51 ± 1.76
DM duration (years, mean ± SD)	-	13 ± 5	22 ± 10
IOP (mmHg, mean ± SD)	-	15.74 ± 1.77	15.09 ± 1.56
BCVA	1.00 ± 0.00	1.00 ± 0.00	0.97 ± 0.06

Abbreviations: SD: standard deviation; DM: diabetic eyes without retinopathy; MDR: diabetic eye with mild diabetic retinopathy; BCVA: best corrected visual acuity

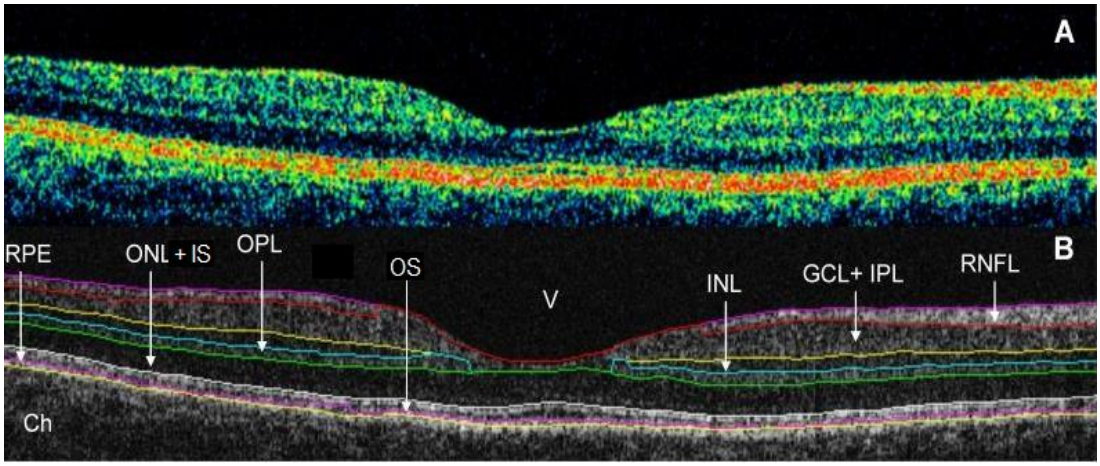

Fig. 1 Macular image segmentation using OCTRIMA. (A) The image of a healthy macula scanned by Stratus OCT. (B) The same OCT scan processed with OCTRIMA. Abbreviations: Ch, choroid; GCL+IPL, ganglion cell layer and inner plexiform layer complex; INL, inner nuclear layer; ONL+IS, combined outer nuclear layer and inner segment of photoreceptors; OS, outer segment of photoreceptors; OPL, outer plexiform layer; RNFL, retinal nerve fiber layer; RPE, retinal pigment epithelial layer; V, vitreous. Note that OCTRIMA measures the thickness of the whole retina between the inner limiting membrane and the inner boundary of the photoreceptor outer segment/RPE junction. The thickness of the combined ONL+IS structure is measured between the outer boundary of OPL and the inner boundary of the photoreceptor outer segment/RPE junction.

criteria for healthy controls included best-corrected visual acuity of 20/25 or better, no history of any current ocular or systematic disease and a normal-appearing macula on contact lens biomicroscopy. All eye examinations were performed at the Department of Ophthalmology, Semmelweis University, Budapest, Hungary. A total of 74 normal healthy eyes, 38 eyes with type 1 diabetes mellitus with no retinopathy and 43 eyes with mild diabetic retinopathy on biomicroscopy were included in this study (see Table 1).

2.2 OCT System and Measurements

The OCT system (Stratus OCT, Carl Zeiss Meditec, Dublin, California) used in this study employs a broadband light source, delivering an output power of 1 mW at the central wavelength of 820 nm with a bandwidth of 25 nm. It has a scanning speed of 400 A-scans per second with a resolution of 10 μm in tissue that determines the imaging axial resolution of the system. A cross-sectional image is achieved by the axial reflectance while the sample is scanned laterally. All Stratus OCT study cases were obtained using the macular thickness map protocol. This protocol consists of six radial scan lines centered on the fovea, each having a 6 mm transverse length. To obtain the best image quality, focusing and optimization settings were controlled, and scans were accepted only if the signal strength was above 6 (preferably 9-10) [15]. Scans with

foveal decentration (i.e., with center point thickness SD >10%) were repeated.

2.3 OCT image processing

OCT signals were collected and exported from the OCT device in the form of 16-bit grayscale images. To use OCT to quantitatively evaluate structural changes of the cellular layers of the retina caused by some severe eye diseases, a segmentation of these layers is required. We used a computer-aided grading methodology for OCT retinal image analysis (OCTRIMA) that is an interactive, user-friendly stand-alone application for analyzing Stratus OCT retinal images [16]. This method integrates a denoising and edge enhancement technique along with a segmentation algorithm previously developed by Cabrera et al [17]. The denoising and edge enhancement techniques are part of a novel preprocessing step that facilitates better automatic segmentation results (see Figure 1). Also, the semi-automatic segmentation correction tool minimizes segmentation errors generated during the automatic segmentation process, significantly reducing the need for manual error corrections. It also gives quantitative information about intraretinal structures and facilitates the analysis of other retinal features that may be of diagnostic and prognostic value, such as morphology and reflectivity.

2.4 Fractal Analysis

In the analysis of OCT images, fractal analysis has been used to investigate the structural change of biological tissue. For example, Fluearu et al. used the box counting method to calculate the fractal dimension to characterize porcine arterial tissue [18]. Sullivan et al. utilized the box counting method to calculate the fractal dimension to classify the breast carcinoma [19]. The power spectrum method has been used to perform the fractal analysis on the layered retinal tissue for investigating the diseased tissue in diabetic patients and healthy subjects [5-7,17,20]. In those studies, the fractal analysis was performed on each A-scan within each region of interest (ROI). Therefore, only the irregularity or roughness along the direction of A-scans was considered in the one-dimensional fractal analysis, while the irregularity or unevenness in all other directions was ignored. Therefore, to extend the fractal analysis in all directions in OCT images and to improve the accuracy of the fractal analysis, the two-dimensional fractal analysis for intraretinal layers of OCT images is necessary.

To determine the fractal dimension of 2D OCT images, several definitions of fractal dimension have been used [21]. One straightforward and understandable methodology for calculating the 2D fractal dimension is the differentiate box counting method [22]. The method of differentiate box counting method is described below.

Consider a grayscale image in a Cartesian coordinate (x,y,z), the coordinates (x,y) denote the 2D position on the image plane, and the coordinate (z) represents the intensity value. In the 2D differentiate box-counting method, the image plane is covered by the non-overlapping grids. Assume the grayscale image's size is $W \times W$ and the non-overlapping grid's size is $s \times s$, W and s need to meet the requirement as $W/2 \geq s \geq 2$. Assume the G is the total number of gray level, the value s' can be derived from the following equation: $s' = Gs/W$. Thus, the size of the box that is used to cover the 3D spatial surface is $s \times s \times s'$ as showed in Figure 2. Here, assume that the minimum and maximum gray level in the (i, j) grid were in the box number k and l, respectively, the number of the boxes covering the surface in the grid (i, j) is:

$$n_r(i,j) = l - k + 1.$$

Taking contributions across all grids, we have

$$N_r = \sum_{i,j} n_r(i,j),$$

where N_r is counted for different values of r. Then, the fractal dimension of 2D OCT image can be estimated from the least square linear fit of $\log(N_r)$ versus $\log(1/r)$.

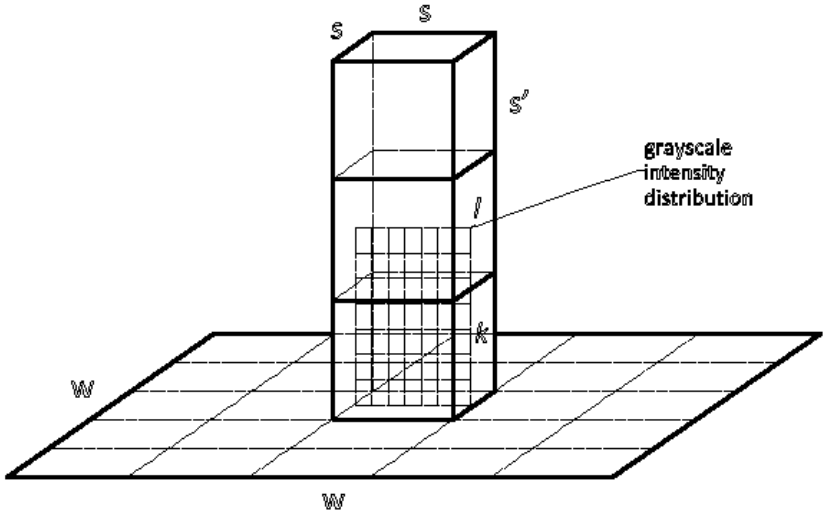

Fig. 2 Sketch of determination of the number of boxes by the differentiate box counting method [23].

2.5 Statistical Analysis

The differences in fractal dimension between study groups were tested using an ANOVA followed by Newman-Keuls posthoc analysis and the student's t-test. Because of the number of comparisons, $p \leq 0.001$ was considered statistically significant. Receiver operating characteristic analysis was also performed on the fractal dimension between study groups to determine the ability of fractal dimension to differentiate diabetic eyes with and without MDR from healthy eyes. AUROC was used to compare diagnostic power. This area summarizes the sensitivity and specificity of diagnosis over the total range of valid diagnostic thresholds. An AUROC of 1.0 indicated perfect discrimination. An AUROC of 0.5 indicated no discrimination. The AUROC calculations and statistical analyses were performed using the software package SPSS version 16 (SPSS Inc., Chicago, Illinois).

3 Results and Discussion

OCT is usually employed for the measurement of retinal thickness. However, the fractal analysis may provide further information regarding cellular layers and early damage in ocular diseases. In this study, the fractal dimension showed the most powerful diagnostic utility for detecting early changes in the diabetic retina.

Significantly smaller values of fractal dimension were observed in all layers in the MDR eyes compared with controls (except INL, see Table 2). Specifically, the fractal dimension was 2.0% smaller in the OPL as compared to healthy eyes. When comparing MDR with DM eyes, the fractal dimension had a significantly less value in all intraretinal layers. Specifically, the fractal dimension was 1.7% smaller in the RNFL. Our results suggest that the RNFL, OPL, ONL+IS, and OS are more susceptible to initial damage when comparing MDR with control eyes. Mainly, the trend observed for the fractal dimension of the RNFL in MDR eyes might be associated with pathological metabolic changes in the retina and may reflect neurodegenerative changes in the diabetic retina. These findings also have possible implications for the early detection of macular damage in diabetes. Because the macular region is rich in retinal ganglion cells, it could be suggested that diabetic damage of this central area might occur early in the disease process. In fact, animal models of DR have shown significant loss of macular ganglion cells [24-28]. Moreover, the fractal dimension of the OPL and OS in MDR eyes was significantly smaller than similar measures in normal healthy eyes. Previous studies have shown that not only retinal pericytes and endothelial cells are susceptible to hyperglycemia, but neuroglial elements of the retinal are also involved in the retinal damage caused by diabetes. Interestingly, in the one-dimensional fractal analysis performed using the same OCT data, the fractal dimension of the OPL in MDR eyes showed significantly higher values compared to healthy eyes [20]. The opposite conclusion might be due to Henle fiber layer artifacts that the thickness and the reflectance information might have been changed as the scanning is performed at oblique angles [29-30].

The ROC analysis was performed for the fractal dimension measures of each intraretinal layer. The AUROC values are shown in Table 3 by study groups.

Table 2 Distribution statistics of fractal dimension (mean ± SD) values by study group.

Fractal Dimension	Controls	DM	MDR
RNFL	2.071 ± 0.021	2.078 ± 0.015‡§	2.043 ± 0.041‡§
GCL+IPL	2.219 ± 0.020	2.219 ± 0.017‡	2.202 ± 0.031‡
INL	2.104 ± 0.028	2.110 ± 0.018‡§	2.089 ± 0.030§
OPL	2.155 ± 0.026	2.141 ± 0.034‡§	2.111 ± 0.024‡§
ONL+IS	2.138 ± 0.038	2.137 ± 0.034‡§	2.107 ± 0.037‡§
OS	2.075 ± 0.015	2.080 ± 0.013‡§	2.053 ± 0.016‡§
RPE	2.076 ± 0.011	2.077 ± 0.008‡§	2.067 ± 0.012‡§

‡ $p < 0.001$ (ANOVA followed by Newman-Keuls post hoc analysis) and § $p < 0.001$ (student's t-test) between MDR and healthy eyes (see MDR column) and between MDR and DM eyes (see DM column).

Table 3 AUROC values of best diagnostic parameters by study group.

Intraretinal Layer	MDR vs. Controls	MDR vs. DM	DM vs. Controls
RNFL	0.744*	0.846**	0.374
GCL+IPL	0.670	0.664	0.526
INL	0.652	0.711*	0.460
OPL	0.889**	0.732*	0.598
ONL+IS	0.726*	0.712*	0.508
OS	0.844**	0.906**	0.392
RPE	0.706*	0.740*	0.496

$0.7 \leq$ AUROC ≤ 0.8, **$0.8 \leq$ AUROC.

Detailed ROC analysis results for the fractal dimension that showed a significant difference between the groups are also shown in the Tables 4-5 and Figures 3-4. All AUROC values were greater than 0.5 when comparing MDR eyes to controls and DM eyes. The highest AUROC values estimated for the fractal dimension were observed for OPL and OS (0.889 and 0.844, respectively) when comparing MDR with normal healthy eyes. The cutoff point for the OPL was suggested to be 2.126 with a sensitivity and specificity of 83.3% and 74.4%, respectively. The cutoff point for the OS was proposed to be 2.061 with a sensitivity and specificity of 79.7% and 69.8%, respectively. The highest AUROC values estimated for the fractal dimension were observed for the RNFL and OS (0.846 and 0.906, respectively) when comparing MDR with DM eyes. The cutoff point for the RNFL was suggested to be 2.065 with a sensitivity and specificity of 81.6% and 72.1%, respectively. The cutoff point for the OS was proposed to be 2.065 with a sensitivity and specificity of 86.8% and 76.7%, respectively. The highest AUROC values were obtained for the OS when comparing MDR eyes with controls and DM eyes. This particular results might suggest that diabetes inflicts additional damage to the outer photoreceptor segment, which could be an early indication of visual function degeneration that could be used as an additional indicator to enable the early detection of diabetic retinal damage or disease progression [31-33].

There are some potential shortcomings of our study. Time domain OCT technology has some limitations compared to the more advanced OCT technology. Also, current OCT devices include different segmentation algorithms and methods for speckle noise removal. Therefore, data analysis is influenced by particular assumptions and technological specifications that are in place for each OCT device. Moreover, the box-counting method to calculate the fractal dimension has been reported as not the best technique to estimate fractal dimension when the image intensity surface is smooth [22,32]. Therefore, a modified differentiate box counting method should be considered to avoid the underestimation of fractal dimension. In the modified differentiate box-counting method, a random shift is added to the column in the vertical or horizontal direction when counting the number of the boxes for the 3D spatial surface. Though the random shifting in each column needs some additional computation time, the modified differentiate box counting method could generate the exact fractal dimension in smoothly textured images.

Table 4 Cutoff values derived from the ROC analyses between MDR group and Controls.

Intraretinal Layer	AUROC	Asymptotic 95% CI Lower-upper bound	Cutoff Point	Sensitivity	Specificity
RNFL	0.744	0.651 - 0.836	2.063	75.7%	65.1%
GCL+IPL	0.670	0.560 - 0.780	2.214	70.3%	60.5%
INL	0.652	0.548 - 0.756	2.098	66.2%	55.8%
OPL	0.889	0.831 - 0.947	2.126	83.8%	74.4%
ONL+IS	0.726	0.630 - 0.821	2.120	73.0%	62.8%
OS	0.844	0.769 - 0.919	2.061	79.7%	69.8%
RPE	0.706	0.609 - 0.803	2.071	67.6%	58.1%

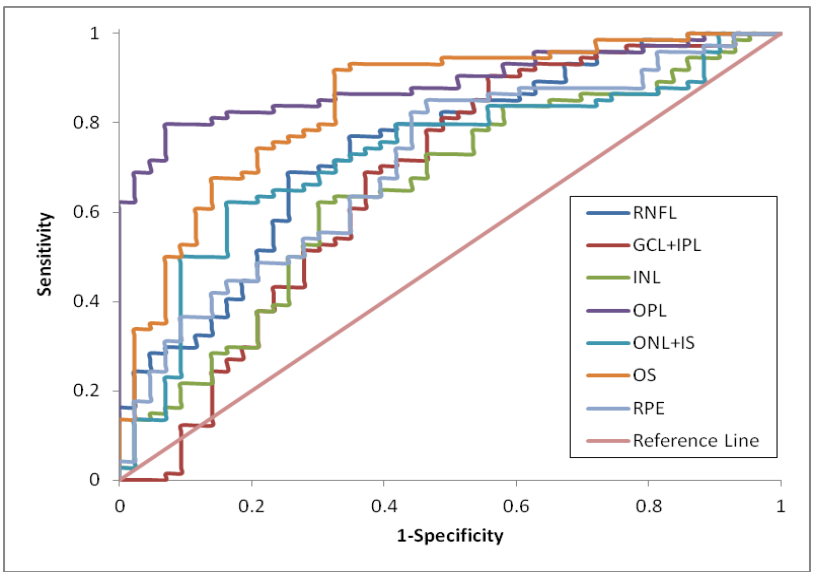

Fig. 3 Receiver operating characteristic (ROC) curves for the detection of diseased tissue using fractal dimension as the predictor variable when comparing MDR group to healthy group.

Table 5 Cutoff values derived from the ROC analyses between MDR group and DM group.

Intraretinal Layer	AUROC	Asymptotic 95% CI lower-upper bound	Cutoff Point	Sensitivity	Specificity
RNFL	0.846	0.764 - 0.928	2.065	81.6%	72.1%
GCL+IPL	0.664	0.544 - 0.784	2.210	65.8%	55.8%
INL	0.711	0.598 - 0.824	2.100	71.1%	60.5%
OPL	0.732	0.618 - 0.845	2.119	63.2%	53.5%
ONL+IS	0.712	0.597 - 0.826	2.111	65.8%	55.8%
OS	0.906	0.840 - 0.971	2.065	86.8%	76.7%
RPE	0.740	0.631 - 0.848	2.073	73.7%	62.8%

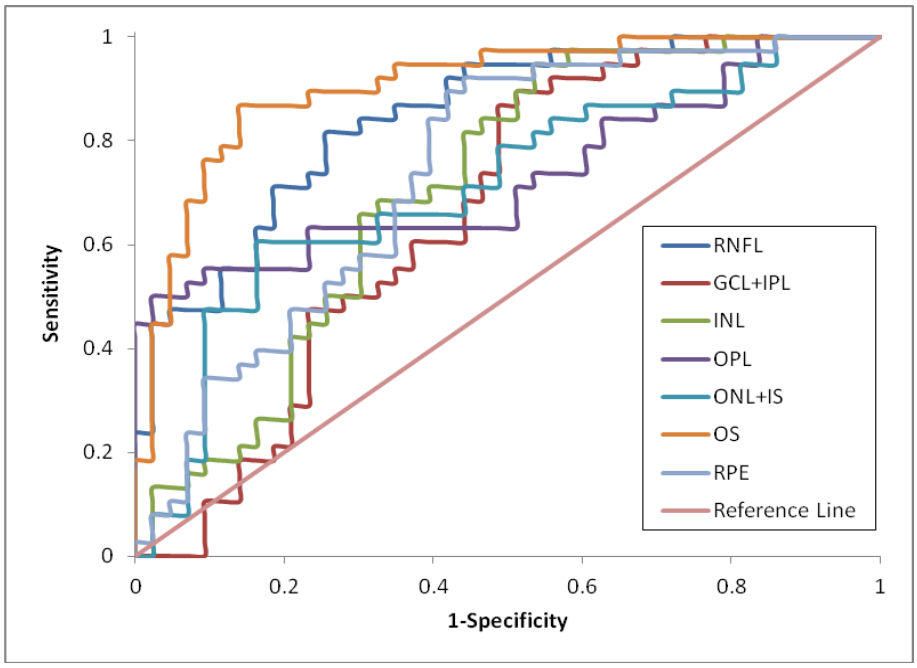

Fig. 4 Receiver operating characteristic (ROC) curves for the detection of diseased tissue using fractal dimension as the predictor variable when comparing MDR group to DM group.

Also, fractal analysis using the power spectrum technique, which is generalizable and potentially more precise, should be compared with the modified differentiate box counting method results to investigate which one produce better estimates in OCT imaging [34-35].

4 Conclusion

The early results presented have shown this methodology could have the potential to differentiate diabetic eyes with early retinopathy from normal healthy eyes. Particularly, this result is in agreement with previous reports showing a significant reduction of the fractal dimension during induced apoptosis throughout early apoptotic phases in breast cancer cells. This observation could be an early indication of visual function degeneration and could be used to improve early sign of diabetic retinal damage and disease progression. Future studies are needed to determine the accuracy, repeatability and full capability of this methodology with more OCT scans and advanced technology. A possibility of error exists due to the quantization nature of the approach, especially when the image intensity surface is smooth.

5 Acknowledgement

This study was supported in part by a Juvenile Diabetes Research Foundation Grant, the research grants NIH R01EY020607, NIH Center Grant P30 EY014801 and a grant from Research to Prevent Blindness (RPB), by a research fellowship of the Helen Keller Foundation for Research and Education, the Eötvös Scholarship of the Hungarian Scholarship Fund, by the Zsigmond Diabetes Fund of the Hungarian Academy of Sciences, by the Ministry of Education and Science of the Russian Federation, and by the research grant D2016009 from Ningbo University of Technology of China.

Foreword to the Special Issue on Optical Technologies for Biomedical Applications

We are pleased to present the special issue of JBPE, which focuses on optical technologies for different biomedical applications. The issue contains selected papers presented at Saratov Fall Meeting 2016 (SFM-16) – International Symposium on Optics and Biophotonics - IV (September 27-30, 2016, Saratov, Russia) and includes eight representative papers that well characterize the major topics of SFM-16.

Invited paper of **E. Zherebtsov** and co-authors is based on a plenary lecture presented by **Prof. A. Dunaev** during SFM-16. This paper describes current state of the optical non-invasive diagnostics, especially methodological and metrological provision for this technology. The authors focus on laser Doppler flowmetry and fluorescence spectroscopy.

Invited paper of **L. Oliveira** and co-authors is related to the study of wavelength dependence of the refractive index of healthy and pathological human colorectal mucosa. Authors underline that refractive index, which can be measured directly, is very significant for the improvement or development of optical technologies in clinical practice. The presented results have demonstrated that it is possible to discriminate between healthy and pathological tissues from refractive index measurements.

Investigations of refractive index dispersion, permittivity and absorption coefficient of human nails in THz frequency range are presented in paper of **V. Guseva** and co-authors. These results may be used for development of non-invasive technique of human pathology monitoring using a nail as a reference sample in reflection mode of THz time-domain spectroscopy.

The main blood protein albumin attracts much attention of researchers. **E. Nepomnyashchaya** and co-authors have investigated the albumin-fullerenol interaction by laser correlation spectroscopy. Authors have suggested a new algorithm for the solution of the inverse problem allowing one to analyze sizes of nanoparticles in polydisperse solutions.

Deficiency or over exposure to iron of the living organism can cause various diseases ranging from anemia to iron overload, and possibly to neurodegenerative diseases. Therefore, it is of undoubted interest to study the molecular dynamics of the processes occurring in aqueous solutions of serum albumin under the influence of iron ions. **V. Gibizova** and co-authors have investigated the molecular mobility of the albumin molecules in pure aqueous solution and at the addition of ferric chloride III by light scattering method.

Photosensitizing properties of novel supramolecular systems based on chlorin e6 are discussed in paper of **I. Klimenko** and **A. Lobanov**. The influence of various excipients on spectral characteristic of these systems as well as the influence of intermolecular interactions on aggregation behavior of chlorin e6 in solutions have been studied.

The use of nanostructures in therapy is an actual problem in the medicine. The bactericidal activity of nanocomposites prepared on the basis of natural glauconite matrix and antibiotics against Staphylococcus aureus has been demonstrated by **S. Venig** and co-authors. The authors note the prospects for use of glauconite composites in human and veterinary medicine.

For the past few years, there has been a rapid development of nanovaccine design, which are on use to solve relevant problems of prevention and treatment of human and animal diseases. **P. Mezhenny** and co-authors present the study of immunogenic properties of transmissible gastroenteritis virus antigen conjugated with gold and selenium nanoparticles.

In overall, papers collected in this special issue demonstrate well the exciting potential of optical technologies for biomedical studies and applications aiming medical diagnostics and treatment.

Special issue Editors:

Elina A. Genina, Alexey N. Bashkatov,
Optics and Biophotonics Department, Research and Educational Institute of Optics and Biophotonics of the Saratov National Research State University; Biophotonics Laboratory of the Tomsk National Research State University, Russia

Valery V. Tuchin,
Optics and Biophotonics Department, Research and Educational Institute of Optics and Biophotonics of the Saratov National Research State University; Institute of Precision Mechanics and Control RAS; Biophotonics Laboratory of the Tomsk National Research State University; Samara National Research University, Russia

Synthesis of glauconite composites and study of their antibacterial activity

Sergey B. Venig[1], Rimma K. Chernova[1], Victor G. Sergeantov[1], Alexey A. Selifonov[2], Olga G. Shapoval[2], Olga V. Nechaeva[2], Vladimir P. Splyukhin[1], Andrey M. Zakharevich[1], Ekaterina I. Selifonova[1], Galina N. Naumova[1*], and Natalia N. Scherbakova[1]

[1] Saratov National Research State University, 83 Astrakhanskaya str., Saratov 410012, Russia

[2] Saratov State Medical University, 112 Bolshaya Kazachya Street, Saratov 410012, Russia

***e-mail**: naumova.galinka.93@mail.ru

Abstract. The elemental composition, the surface morphology and the sorption properties of glauconite from the Beloozerskoye deposit in Saratov Region were investigated. The nanocomposites based on glauconite as a matrix with doxycycline and tetracycline were synthesised. The antibacterial activity of the obtained composites against Staphylococcus aureus was studies. © 2016 Journal of Biomedical Photonics & Engineering.

Keywords: glauconite, tetracycline, doxycycline, sorption, antibacterial composite, *Staphylococcus aureus.*

Paper #3125 received 2016.11.19; revised manuscript received 2016.12.29; accepted for publication 2016.12.30; published online 2016.12.31. doi: 10.18287/JBPE16.02.040303. [Saratov Fall Meeting 2016 Special Issue].

References

1. J. M. Huggett, "Minerals/Glauconites," in Encyclopedia of Geology, 542–548 (2005).
2. V. Valanciene, R. Siauciunas, and J. Baltusnikaite, "The influence of mineralogical composition on the colour of clay body," Journal of the European Ceramic Society 30(7), 1609-1617 (2010).
3. O. A. Hegab, and A. G. Abd El-Wahed, "Origin of the glauconite from the Middle Eocene, Qarara Formation, Egypt," Journal of African Earth Sciences 123, 21-28 (2016).
4. L. M. Moretto, E. F. Orsega, and G. A. Mazzocchin, "Spectroscopic methods for the analysis of celadonite and glauconite in Roman green wall paintings," Journal of Cultural Heritage 12(4), 384-391 (2011).
5. S. S. Chang, Y. H. Shau, M. K. Wang, C. T. Ku, and P. N. Chiang, "Mineralogy and occurrence of glauconite in central Taiwan," Applied Clay Science 42(1-2), 74-80 (2008).
6. G. El-Habaak, M. Askalany, M. Faraghaly, and M. Abdel-Hakeem, "The economic potential of El-Gedida glauconite deposits, El-Bahariya Oasis, Western Desert, Egypt," Journal of African Earth Sciences 120, 186-197 (2016).
7. A. V. Voronina, V. S. Semenishchev, A. A. Bykov, M. O. Savchenko, A. S. Kutergin, and T. A Nedobuh, "Approaches to rehabilitation of radioactive contaminated territories," Journal Of Chemical Technology And Biotechnology 88(9), 1606–1611 (2013).
8. T. Bajda, and Z. Kłapyta, "Adsorption of chromate from aqueous solutions by HDTMA-modified clinoptilolite, glauconite and montmorillonite," Applied Clay Science 86, 169-173 (2013).
9. E. H. Smith, W. Lu, T. Vengris, and R. Binkiene, "Sorption of heavy metals by Lithuanian glauconite," Water Research 30(12), 2883-2892 (1996).
10. T. J. Berger, J. A. Spadaro, S. E. Chapin, and R. O. Becker, "Electrically Generated Silver Ions: Quantitative Effects on Bacterial and Mammalian Cells," Antimicrob Agents Chemotherapy 9(2), 357-358 (1976).
11. B. Bagchi, S. Kar, S. K. Dey, S. Bhandary, D. Roy, T. K. Mukhopadhyay, S. Das, and P. Nandy, "In situ synthesis and antibacterial activity of copper nanoparticles loaded natural montmorillonite clay based on contact inhibition and ion release," Colloids Surf B Biointerfaces 108, 358-365 (2013).
12. D. Avisar, O. Primor, I. Gozlan, and H. Mamane, "Sorption of Sulfonamides and Tetracyclines to Montmorillonite Clay," Water, Air, & Soil Pollution 209(1), 439-450 (2009).
13. J. Wang, J. Hu, and S. Zhang, "Studies on the sorption of tetracycline onto clays and marine sediment from seawater," Journal of Colloid and Interface Science 349(2), 578-582 (2010).

14. R. Daghrir, and P. Drogui, "Tetracycline antibiotics in the environment: a review," Environ. Chem. Lett. 11(3), 209-227 (2013).
15. S. G. Walker, C. A. Flemming, F. G. Ferris, T. J. Beveridge, and G. W. Bailey, "Physicochemical interaction of Escherichia coli cell envelopes and Bacillus subtilis cell walls with two clays and ability of the composite to immobilize heavy metals from solution," Appl Environ Microbiol. 55(11), 2976–2984 (1989).

1 Introduction

The therapeutic capabilities of glauconite are due to the presence of the clay component of this mineral known as "green clay" and are related to many fields of medicine and cosmetology [1, 2]. It is traditionally used for physiotherapeutic procedures in the treatment of osteochondrosis, podagra, and other arthropathies. It also facilitates fast healing of wounds and other skin lesions. Glauconite-based creams have shown good results in cosmetology, in the treatment of skin inflammations and allergy, acne, seborrhea oleosa, psoriasis, and dermatitis [3-8].

There are also data on using the glauconite-based enterosorbents in veterinary [9-10]. In the digestive tract the glauconite improves the metabolism, namely, it participates in catalytic processes, regulates the content of free intestinal fluid, the composition and concentration of electrolytes, the mineral metabolism, and the acid-base balance. The enterosorbents consisting of glauconite concentrates are used as active agents for prophylactics and treatment of gastrointestinal tract diseases in animals. In this case, glauconite can be applied both solely and in the composition of therapeutic agents and fodder. Thus, it is proposed to use glauconite in the feed additive in combination with the "Biosporin" probiotic (RU 2319391, 2008) to in-crease the immunity and natural organism resistance in pigs.

The clay-based antibacterial preparation studied up to now mainly include metallic nanoparticles or an antibacterial medicine [11]. Thus, the montmorillonite and the bed silt are able to absorb sulphonamides and antibiotics [12, 13]. In the literature, the data on the sorption of tetracycline and doxycycline by the glauconite and on the antibacterial properties of glauconite composites with immobilised antibiotics are absent. Alongside with sulphanilamides and penicillins, the tetracycline antibiotics are most frequently used in medicine and veterinary because of their high antimicrobial activity and low cost of the preparations. To date nearly 40 natural and 3000 synthesised tetracycline antibiotics are known. Annually in veterinary more than 3350 tons of tetracyclines are used in Russia, more than 3200 tons in the USA, and more than 2575 tons in Europe [14]. Therefore the issue of synthesis and study of antibacterial composites based on natural sorbents and tetracycline antibiotics and possessing high bactericidal activity for both external and internal use is interesting and urgent.

2 Materials and Methods

As a matrix for the composites, we used the enriched fraction of glauconite, extracted from the glauconite sand using the magnetic separation technique and containing 85% of glauconite. The morphological characteristics of glauconite were studied using the scanning electron microscope (SEM) MIRA 2 LMU (Tescan, Czech Republic). The elemental composition of the enriched glauconite was analysed using the energy dispersive microanalysis system INCA Energy 350 (SEM), as well as the X-ray fluorimeter Innov X-5000 with silicon drift detector. The texture characteristics of the aluminosilicate were studied by means of the Brunauer–Emmett–Teller (BET) method of measuring the specific sorbent surface, based on the measurement of equilibrium adsorption of nitrogen at 77 K using the Quantachrome nova 2200 system.

The role of biologically active components of the nanocomposite was played by the antibacterial preparations tetracycline and doxycycline. The glauconite-antibiotic composite was obtained by means of sorption in the static regime at room temperature. To get the composite the portions of 0.5 g of glauconite were put in conic flasks, poured with 25 ml of the initial aqueous solution of tetracycline (TC) or doxycycline (DC) hydrochloride (C_0(TC)=5.198*10^{-5} mole/l and C_0(DC)=8.316·10^{-5} mole/l) and mixed during 90 minutes by means of a magnetic mixer. After filtering, the residual solid phase was dried at room temperature. The residual concentration of antibiotics in the filtrate was determined by means of spectrophotometry (λ=346 nm) using the preliminarily drawn calibration plot.

The antibacterial activity of the obtained composites of glauconite with immobilised antibiotics was assayed using the strain S. *aureus* ATCC 6538-P. The broth culture of the strain was volumetrically seeded by 1 ml (10^5 CFU) on meat infusion agar and the grown colonies were counted immediately and in 3 and 6 hours after the seeding. For this purpose to the portions of the composite 100 ml of sterile beef-extract broth (BEB) was added. Then the suspension of pure one-day culture of the above strain, prepared using the opacity standard of L. A. Tarasevich State Institute of Standardization and Control of Biomedical Preparations (OT 0.75 at the wavelength 600 nm) and diluted by saline to the final concentration of 10^5 CFU/ml was inoculated by 1 ml. The seeded cultures in the BEB with glauconite portions without antibiotics and the medium without these substances were used for control samples. The weight portions of the composites were determined by the necessity to create its sub-inhibiting concentrations, basing on the acceptable values of the minimal inhibiting concentrations of these antibiotics for the

experimental strain. All seedings were triply repeated and incubated in a thermostat at 37 °C. The statistical processing of the results included the calculation of the arithmetical mean of cell number (M) in 1 ml and the standard deviation (m); then we evaluated the significant difference of the mean values from the control samples with the probability 95 %.

3 Results and discussion

We found that the grains have layered surface, formed by flakes having different shape and size. The thickness of the flakes varies from 10 to 90 nm, and the separation be-tween them amounted to 10-200 nm (Fig. 1).

The elemental composition of the enriched glauconite determined using the energy dispersive microanalysis system INCA, as well as the X-ray fluorimeter, is presented in Table 1.

As follows from the table, the studied glauconite is characterised by a variety of macro- and microelements.

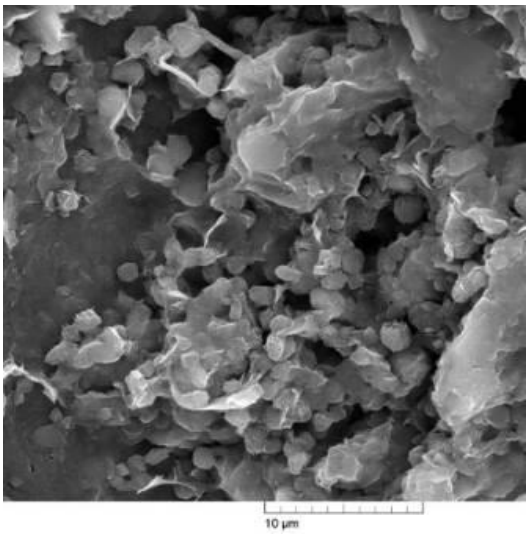

a)

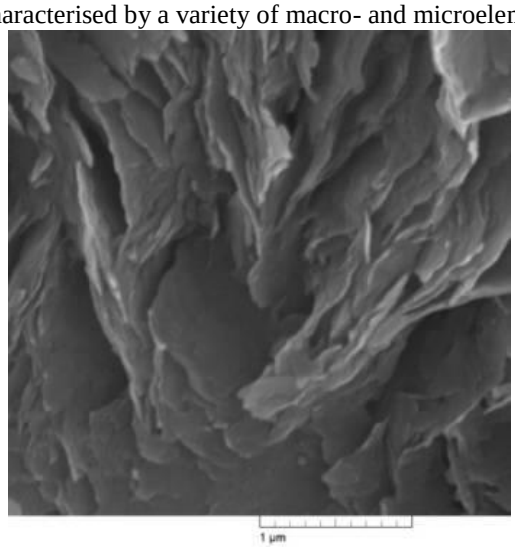

b)

Fig. 1 Electron microphotographs of the enriched glauconite. Magnification 10 000× (a) and 100 000× (b).

Table 1 Mean microelement (scanning electron microscope) and microelement (X-ray fluorescence analysis) composition of glauconite (m, %).

Macroelement	C	O	Mg	Al	Si	P	K	Ca	Fe
m, %	14.21	48.27	1.05	3.54	20.98	1.10	2.15	1.86	8.59
Microelement	Cr	Mn	Ni	Co	Cu	Zn	V	Zr	Sr
m, %	$1.3 \cdot 10^{-2}$	$5.6 \cdot 10^{-3}$	$3.4 \cdot 10^{-3}$	$4.3 \cdot 10^{-3}$	$2.1 \cdot 10^{-3}$	$4.6 \cdot 10^{-3}$	$1.4 \cdot 10^{-3}$	$2.3 \cdot 10^{-3}$	$9.8 \cdot 10^{-3}$

The obtained isotherms of adsorption-desorption of nitrogen on glauconite according to the IUPAC classification belong to the isotherms of the IV type, characterised by the presence of the capillary-condensation hysteresis loop, which label the presence of mesopores having the size from 2 to 50 nm (Fig. 2).

The sharp increase of the isotherm at P/P_0 close to 1 indicates the minor presence of large pores in the sample. The sharp increase in the low-pressure region is identical to the shape of type I isotherm, typical for microporous sorbents. Note also that according to the de Boer classification the hysteresis loop shape corresponds to the type B and indicates the presence of slit-like pores. Thus, all studied samples possess the dominating mesoporous structure and a small number of micro- and macropores. From the adsorption and desorption branches of isotherms the following texture characteristics of the enriched glauconite were found: the specific surface 35.04 m^2/g, the total volume of pores (P/P_o=0.98) 0.048 cm^3/g.

We estimated the parameters of sorption ability of glauconite with respect to doxycycline (R=91.2%) and tetracycline (R=82.3%). They are adsorbed on the mineral surface at the expense of the chemosorption process, facilitated by the presence of hydroxyl groups in the structure of glauconite and of active groups in the structure of the studied antibiotics.

It was established that in 3 hours after the seeding, the arithmetic mean cell number (M) of the S. *aureus* strain did not essentially differ from that of the control sample for the smallest composite portion with doxycycline (0.015 mg). The antibacterial effect of the 0.03 mg composite with doxycycline appeared to be comparable with the effect of the doxycycline preparation itself. In 6 hours of S. *aureus* strain incubation the significant difference of the values (M) compared to the control samples (C) was observed for both doxycycline concentrations (0.25 and 0.125 µg/ml) and the composite with the mass 0.03 mg. The 0.015 mg portion of nanocomposite in 6 hours after the seeding did not suppress the development of bacterial colonies

S. *aureus*, and the result is comparable with the control sample. The best effect of the composite was observed for the portion of 25 mg with respect to S. *aureus*, the number of colonies being essentially smaller than in the control sample (Table 2).

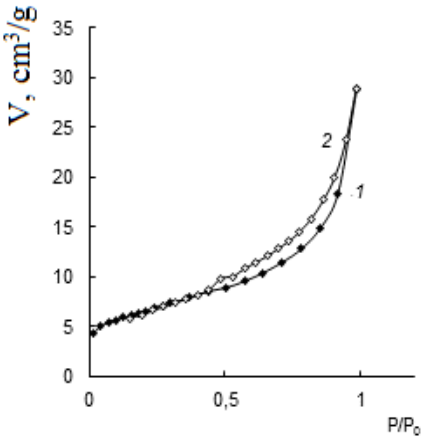

Fig. 2 Isotherms of adsorption (1) – desorption (2) of nitrogen at 77 K on the enriched glauconite.

Thus the sorbed doxycycline и tetracycline in the inhibiting concentrations suppress the development of the S. *aureus* strain population in the logarithmic phase of the growth (Fig. 3).

Discussing the possible mechanism of the antibacterial effect of the synthesised composite, it is worth noting that besides the antibacterial properties of the antibiotics themselves, an important feature is the possibility of direct contact of the bacterial membrane with hydrophobic particles of glauconite, when the latter "encapsulates" the bacterial cells. Ref. [15] can be considered as confirming this useful property of the glauconite matrix. Walker et al. studied the interaction of bacterial membranes with the clay particles of kaolinite and smectite. They demonstrated the alignment of particles around the bacterial cell wall as a result of forming the polynuclear complex bridge $[Al_{13}(OH)_{31}]^{7+}$.

Table 2 The mean number of S. *aureus* cells in 1 ml of BEB (M, CFU/ml) and its standard deviation (m) depending on the cultivation conditions (n=3, p=0.95).

M±m CFU/ml							
Doxycycline							
Seeding time	K[1]	Glauconite 0.5 mg	Glauconite 0.25 mg	Doxycycline 0.25 µg/ml	Doxycycline 0.125 µg/ml	Composite 0.03 mg	Composite 0.015mg
0 h	600±290	420±50	550±80	330±70	330±90	350±160	290±130
3 h (Lag-phase)	1040±260	570±180	970±110	440±170[2]	410±110[2]	490±170[2]	1120±450
6 h (Log-phase)	7230±2350	8730±960	6490±2700	620±20[2]	500±90[2]	660±210[2]	12010±5210
Tetracycline							
Seeding time	K[1]	Glauconite 2.5 mg	Glauconite 1.25 mg	Tetracycline 4 µg/ml	Tetracycline 2 µg/ml	Composite 2.5 mg	Composite 1.25mg
0 h	323±93	451±80	442±65	451±77	470±62	519±29	446±84
3 h (Lag-phase)	1967±208	1663±323	1693±170	630±262[2]	710±252[2]	777±212[2]	753±152[2]
6 h (Log-phase)	12767±568	13500±888	13800±1277	673±392[2]	798±282[2]	937±182[2]	1267±252[2]

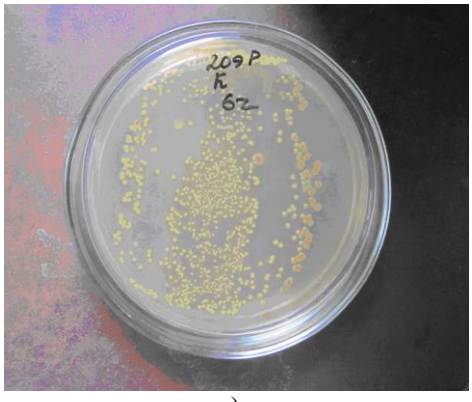

a)

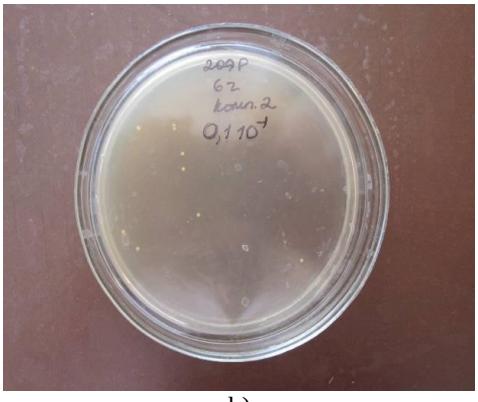

b)

Fig. 3 Character of changes in the *S. aureus* ATCC 6538-P colonies after 6 hours of cultivation: a) control measured seeding (7230±2350 CFU/ml) b) measured seeding (660±210 CFU/ml) after treating with the glauconite composite with immobilised doxycycline.

4 Conclusion

We established the macro- and microelement composition of the glauconite, the squamous surface of its grains, some texture characteristics and good adsorption capacity for the antibiotics tetracycline and doxycycline.

The tetracycline and doxycycline antibacterial preparations were immobilised in the glauconite matrix. The obtained composites in the inhibiting concentrations suppress the growth of the staphylococci. Significant difference in the number of *S. aureus* colonies compared to the control seedings are demonstrated. Thus, it is interesting to perform further studies of bactericidal properties of glauconite composites with other strains of microorganisms and to evaluate the prospects of their applications in medicine and veterinary.

Serum albumin molecular mobility in water solutions, containing iron chloride III

Victoria V. Gibizova*, Viktor A. Sapozhnikov, Ksenia V.Fedorova, and Galina P. Petrova
Department of Physics, M.V. Lomonosov Moscow State University, Leninskiye Gory 1, building 2, Moscow GSP-1, 119991, Russian Federation

***e-mail:** gibizova@physics.msu.ru

Abstract. The lack or overload of iron in living organism can cause different diseases, including those related to the serum blood. In this connection the basic blood proteins, in particular, albumin, can change their charge, conformation, molecular mobility, etc. Due to this fact, it is of undoubtful interest to study the molecular dynamical processes that occur in water solutions of serum albumin under the effect of iron ions. In the present work we performed comparative studies of optical properties of bovine serum albumin (BSA) water solutions and BSA solutions with the addition of Iron(III) chloride by light scattering. © 2016 Journal of Biomedical Photonics & Engineering.

Keywords: dynamic light scattering, static light scattering, translation diffusion coefficient, hydrodynamic radius, intermolecular interaction coefficient

Paper #3128 received 2016.11.20; accepted for publication 2016.12.29; published online 2016.12.31. doi: 10.18287/JBPE16.02.040304. [Saratov Fall Meeting 2016 Special Issue].

References

1. P. T. Lieu, M. Heiskala, P. A. Peterson, and Y. Yang, "The roles of iron in health and disease," Molecular Aspects of Medicine 22(1–2), 1–87 (2001).
2. Z. Shu-hong, F. Yong-shan, F. Shuo, and Z. Yun-feng, "Microdetermination of proteins by resonance light scattering technique based on aggregation of ferric nanoparticles," Spectrochimica Acta Part A 72, 748–752 (2008).
3. B. D. Fair, and A. M. Jamieson, "Effect of Electrodynamic Interactions on the Translational Diffusion of Bovine Serum Albumin at Finite Concentration," Journal of Colloid and Interface Science 73(1), 130-135 (1980).
4. M. Othman, A. Aschi, and A. Gharbi, "Polyacrylic acids–bovine serum albumin complexation: Structure and dynamics," Materials Science and Engineering C. 58, 316-323 (2016).
5. V. V. Gibizova, I. A. Sergeeva, G. P. Petrova, A. V. Priezzhev, and N. G. Khlebtsov, "Interaction of Albumin and gamma-Globulin Molecules with Gold Nanoparticles in Water Solutions," Moscow University physics bulletin. 66(5), 449–452 (2011) [in Russian].
6. http://www.photocor.ru/.
7. H. Z. Cummins, and E. R. Pike, Photon Correlation and Light Beating Spectroscopy, Springer Science+Business Media, New York (1974).
8. A. Einstein, Collected Papers, Nauka, Moscow (1966) [in Russian].
9. V. N. Tsvetkov, B. E. Eskin, and S. Y. Frenkel, Structure of Macromolecules in Solutions, Nauka, Moscow (1964) [in Russian].

1 Introduction

Proteins are an important component of a living organism executing different functions. The methods of dynamic and static light scattering are informative methods of studying the behaviour of protein molecules in solutions, using which one can determine the molecular mass, the coefficient of intermolecular interaction, the coefficient of translation diffusion. From the latter, using the Stokes-Einstein equation, one can estimate the hydrodynamic radius of the scattering particles.

The analysis of the effect of different substances on the protein molecules allows the study of the processes that take place in a living organism. Under the development of different pathological changes in the organism, the parameters of protein molecules (total surface charge, intermolecular interaction coefficient, translation diffusion coefficient) can essentially vary.

Iron is one of widespread chemical elements taking part in the vital activity of living organisms. Iron is involved in blood formation, breathing, immune biological processes, and enters into the composition of more than a hundred enzymes.

Iron is a component of haemoglobin that executes the function of binding and delivery of oxygen to the cells of human organism. Therefore, iron is necessary for the synthesis and functioning of haemoglobin.

Iron is present in the human organism mainly as a component of a few biologically active compounds (haemoglobin, myoglobin, iron-containing enzymes) that execute four basic functions:

1. transport of electrons (cytochromes);
2. transport and deposition of oxygen (haemoglobin, myoglobin);
3. participation in the formation of active centres of redox enzymes;
4. transport and deposition of iron (transferrin, ferritin).

The concentration of iron in human blood considerably varies. It has a daily rhythm and the variations of its level in the blood serum of a healthy human during 24 hours can be as large as ~ 100%.

Some diseases cause the change of iron content in the blood serum; thus, the decrease of the iron content is observed in the case of iron-deficit anaemia, the anomaly of iron absorption, and the increased level of iron is observed in the case of hemochromatosis [1].

In this connection, it is interesting to study the molecular dynamic processes that occur in the solutions of the main proteins of blood serum, comprising the iron ions.

In our study as an iron salt, we used Iron(III) chloride (this preparation is also intensely used in water purification).

Most substances enter the organism via the gastrointestinal tract and then appear in the blood circulation system. Albumin, the main protein of blood serum, is a globular protein, the main role of which in the organism is the transport of substances. In this connection, it is important to study the mechanism of interaction between the ferric chloride II and the albumin.

In the literature, there are practically no papers on the interaction of iron salts with serum proteins. However, there are a few papers, e.g., [2], in which the interaction of bovine serum albumin (BSA) with iron nanoparticles having the size of about 5 nm was studied. It was found that the iron nanoparticles with positive charges combine with the -COO- groups of the protein. They interact by means of electrostatic forces, thus forming aggregates of larger particles. In the paper the spectra of light scattered by the iron nanoparticles and by the mixture of iron nanoparticles and BSA were obtained. These spectra show that the intensity of light scattered by the iron nanoparticles is very small. However, when the nanoparticles are mixed with BSA the intensity of the scattered light strongly increases in the range of wavelengths 300-600 nm and reaches its maximum at 451 nm even for small concentrations of BSA (about 0.1 μg/ml).

In other papers the aqueous solutions of BSA were studied [3, 4]. The Americal research team from Ohio determined the BSA translation diffusion coefficients in the concentration 0-200 mg/ml by means of laser light quasielastic scattering. The protein diffusion was studied in the systems having pH that was equal to 7.4 [3]. In this paper it was found that under the increase of BSA concentration the translation diffusion coefficient decreased insignificantly.

The research team from Tunisia University [4] studied the change of protein conformation depending on pH. In the paper they studied the behaviour of the hydrodynamic radius of the particles affected by pH, the scattering angle being $\theta=173°$. It was shown that the hydrodynamic radius of the protein is constant in a wide range of pH values (R_h varied from 38 to 44 Å). These values are close to the results of earlier studies [5]. The increase of the protein molecule size at pH<3 is an evidence of BSA denaturation [4].

2 Experimental results

All studies were carried out using the Photocor Complex setup [6], the laser wavelength being 647 nm, and the power being 25 mW.

3 Preparation of solutions

In the present work, we used the BSA (Sigma) and the 30% aqueous solution of iron(III) chloride (Panreac) as an iron-containing component.

As a solvent, we used the water for injections (OAO "Biokhimik", pH 7.0). The measurements were carried out at the temperature 20 °C.

For experiments it was necessary to prepare three solutions, with the normal (corresponding to a healthy organism) content of iron (1.12 mg/l), the increased (3.35 mg/l), and the decreased (0.28 mg/l) content, respectively. To prepare the first solution we used 10 μl of 30% iron(III) chloride, which were then dissolved in 5 ml of water. In the obtained solution (1) the mass of iron(III) chloride amounted to 13.4 mg. Form the new solution (1) we took 21 μl and added to 5 ml of water. As a result, we obtained the solution with the normal concentration of iron. For the solutions with increased and decreased concentration, we took 62 μl and 5 μl of the obtained aqueous solution (1) of the Iron(III) chloride, respectively, and added to 5 ml of water. Then to each of these samples we added 20 μl of BSA solution having the concentration 50mg/ml.

4 Experimental results obtained using the dynamic light scattering

In the course of the experiment, we fixed the concentration of the ferric chloride and varied the BSA concentration. Basing on the results obtained using the dynamic light scattering method [7] the hydrodynamic radius (R_h) and the translation diffusion coefficient (D_t) were plotted versus the BSA concentration.

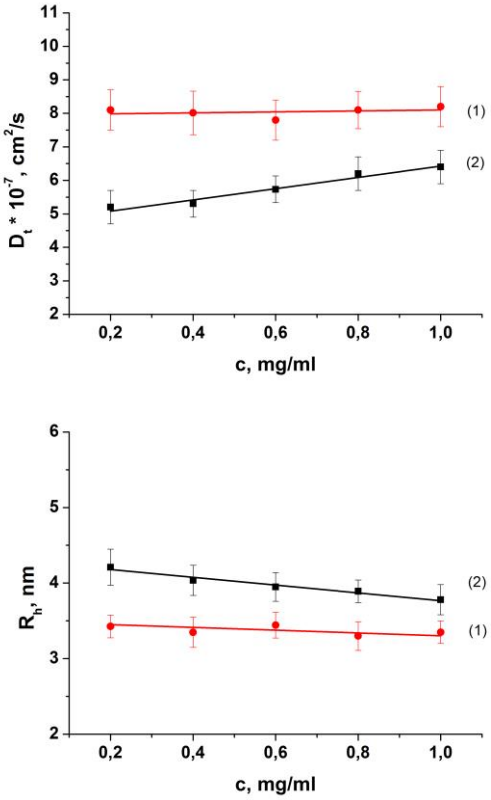

Fig. 1 Concentration dependence of the translation diffusion coefficient (D_t) (top), and the hydrodynamic radius (R_h) (bottom) for pure BSA (1) and for the BSA with the addition of aqueous solution of Iron(III) chloride with the content of Fe^{3+} equal to 0.28 mg/l (2).

The first series of experiments was carried out with the BSA solutions and with those in the presence of iron(III) chloride (c(Fe3+)=0.28 mg/l), which corresponds to the decreased content of iron in human blood (Fig. 1).

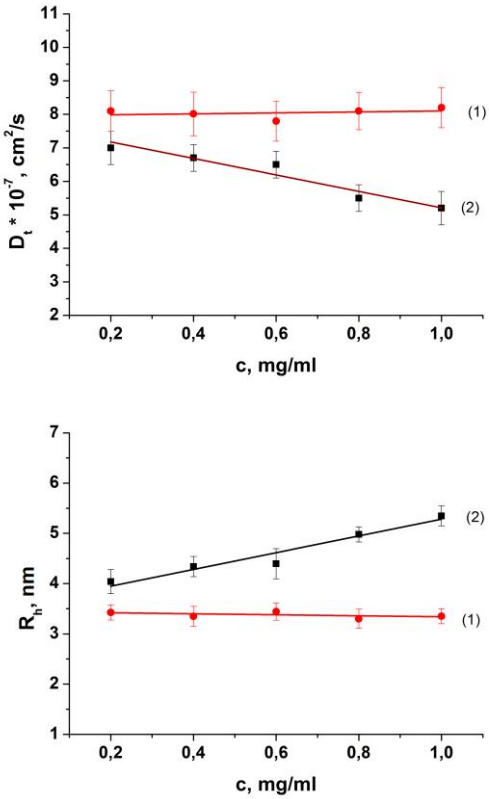

Fig. 2 Concentration dependence of the translation diffusion coefficient (D_t) (top) and hydrodynamic radius (bottom)) for pure BSA solution (1) and for the BSA with the addition of aqueous solution of iron(III) chloride with the content of Fe^{3+} equal to 1.12 mg/l (2).

Then we carried out a series of experiments with the solutions, containing the normal concentration of iron (c(Fe^{3+})=1.12 mg/l) (Fig. 2).

The last series of experiments was carried out with the increased concentration (c(Fe^{3+})=3.35 mg/l).

5 Experimental results obtained by means of the static light scattering method

Using the static light scattering [8] we determined the coefficient of intermolecular interaction ***B*** for BSA solutions with the addition of iron(III) chloride (Fig. 4) and the molecular mass of the scattering particles ***M*** (Fig. 5).

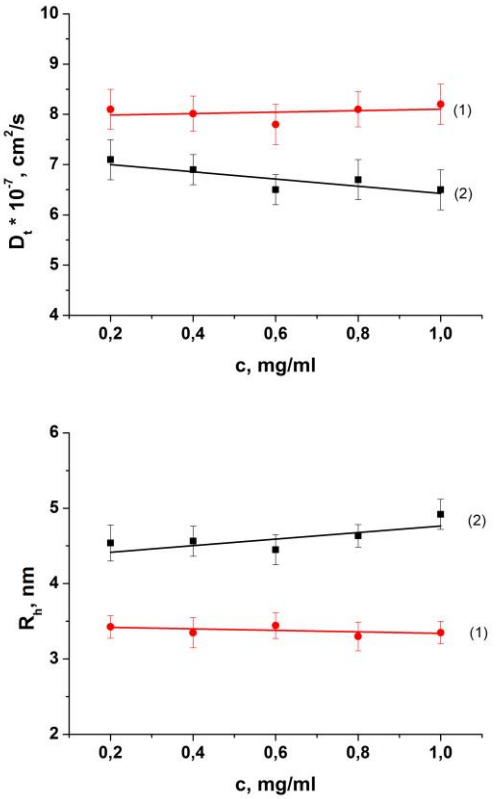

Fig. 3 Concentration dependence of the translation diffusion coefficient (Dt) (top) and hydrodynamic radius (bottom)) for pure BSA solution (1) and for the BSA with the addition of aqueous solution of Iron(III) chloride with the content of Fe3+ equal to 3.35 mg/l (2).

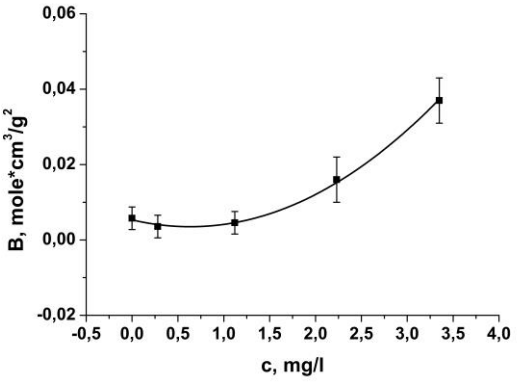

Fig. 4 Dependence of the coefficient of intermolecular interaction upon the concentration of Fe^{3+}.

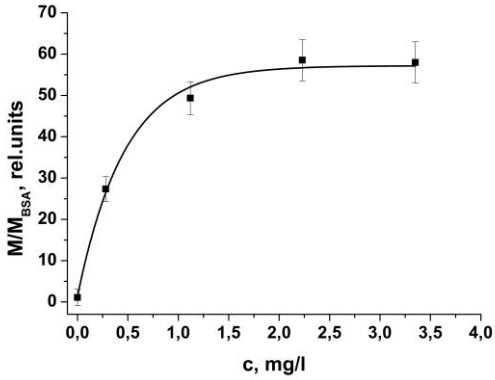

Fig. 5 Dependence of the ratio of the molecular mass of the scattering particles to that of BSA upon the concentration of Fe^{3+}.

6 Discussion

The obtained values of the hydrodynamic radius of particles in the solution exceed the size of BSA molecules in the pure solution by less than 60%. This fact can mean that no protein aggregates are formed.

The growth of molecular size can be explained by partial absorption of ions that appear due to the interaction between the iron(III) chloride with water on the BSA molecules. The model of this process is presented in Fig. 6.

At the same time an insignificant decrease of the translation diffusion coefficient and increase of the intermolecular interaction coefficient occur, caused by the addition of $FeCl_3$.

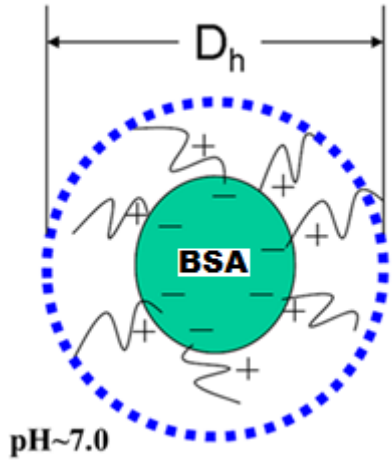

Fig. 6 Model of partial adsorption of iron ions on the BSA protein.

Table 1 The ratio of the scattering particle mass to that of the pure albumin depending on the ionic strength of the solution

I, mmole/l	0	0.025	0.1	0.2	0.3
M/M_{BSA}, rel. units	1.09	27.03	49.3	58.5	58

The results obtained in the course of measurements for the molecular mass of scattering particles in the BSA solution with the addition of Iron(III) chloride (Table 1) were compared with the mass of the particles in the pure solution of Iron(III) chloride (Table 2). According to the Rayleigh-Debye theory, one can find the mass of the scattering particles using the expression

$$\frac{cHK}{R_{90}} = \frac{1}{M} + 2Bc + \cdots, \quad (1)$$

where c is the concentration of the solution, H is the optical constant of the solution, K is the Cabanne factor, R_{90} is the reduced intensity for the angle 90°, B is the second virial coefficient, characterising the degree of the solution imperfection and allowing for pair intermolecular interactions in the solution [9]. The obtained dependence of R_{90} on c does not allow one to determine the mass using the measurement for one concentration. It is necessary to perform measurements for a few values of c and to extrapolate the results to c=0, which yields the following result:

$$M = \left(\frac{cHK}{R_{90}}\right)^{-1}_{c\to 0}. \quad (2)$$

Table 2 The obtained values of the mass of scattering particles and the intermolecular interaction coefficient

	Value	Error
$M*10^6$, g/mole	3.25	0.24
B, mole*cm^3g^2	0.601	0.012

The calculated value of the mass of particles in the Iron(III) chloride solution provides a thorough explanation the sharp increase of the scattering particles under the addition of protein BSA molecules to the solution. The heavy ions that apparently arise in the interaction of the complex compounds of iron that have the radius by 50 times smaller than that of the DSA. The existence of the ion adsorption process i.e., the binding of these heavy complexes to protein molecules becomes theoretically possible, which considerably increases the total mass of the forming particles leaving their radius of these complexes practically unchanged.

7 Conclusion

The study of the behaviour of protein molecules in the albumin solutions, containing the Iron(III) ions is carried out and the features of molecular mobility of albumin molecules in the pure aqueous solution and with the addition of Iron(III) chloride are investigated.

The obtained results allowed the following conclusions:

1. The study of the dynamic parameters of serum albumin under the action of iron(III) ions using the method of photons correlation has shown that the hydrodynamic radius of the scattering particles insignificantly increases due to the addition of iron(III) chloride (by less than 60 %).
2. We have found a significant increase of the mass of scattering particles in BSA solutions under the addition of iron(III) chloride, which can be caused by the formation of heavy ions in the solution of iron(III) chloride due to the interaction of $FeCl_3$ with water.
3. The process of partial adsorption of heavy ion complexes on the negatively charged BSA molecules was observed.
4. It was shown that with the increase of the concentration of (Fe^{3+}) the molecular mass of scattering particles becomes constant. The observed effect can be a consequence of the Langmuir saturation process in the course of the monolayer formation.

It can be summarised that the influence of Iron(III) on the molecular mobility of serum albumin is insignificant.

Acknowledgments

The study was supported by the Russian Foundation for Basic Research, project No. 16-32-00847 mol_a.

Optical non-invasive diagnostics of microcirculatory-tissue systems of the human body: questions of metrological and instrumentation provision

Evgeny A. Zherebtsov, Victor V. Dremin, Angelina I. Zherebtsova, Irina N. Makovik, and Andrey V. Dunaev*

Orel State University named after I.S. Turgenev, 95 Komsomolskaya St., Orel 302026, Russia

* **e-mail**: dunaev@bmecenter.ru

Abstract. Optical techniques are one of the most promising non-invasive technologies for the diagnosis of medical conditions. This work is devoted to the current state of the optical non-invasive diagnostics (OND), especially about instrumentation as well as methodological and metrological provision for this technology. In some details Laser Doppler Flowmetry (LDF) and Fluorescence Spectroscopy (FS) diagnostics methods are considered. The main conclusion is that it is necessary to solve the problems of metrological support OND devices of these types. It is also important to develop a methodology based on diagnostic criteria obtained from a relationship between a number of OND methods and others.

Keywords: optical non-invasive diagnostics, blood microcirculation, biotissue, laser Doppler flowmetry, fluorescence spectroscopy.

Paper #3129 received 2016.11.28; accepted for publication 2016.12.29; published online 2016.12.31. doi: 10.18287/JBPE16.02.040305. [Saratov Fall Meeting 2016 Special Issue].

References

1. V. V. Tuchin (ed.), Handbook on Optical Biomedical Diagnostics, SPIE Press, Bellingham (2002).
2. G. E. Nilsson, T. Tenland, and P. A. Oberg, "Evaluation of a laser Doppler flowmeter for measurement of tissue blood flow," IEEE Trans Biomed Eng BME 27(10), 597-604 (1980).
3. A. N. Obeid, N. J. Barnett, G. Dougherty, and G. Ward, "A critical-review of laser Doppler flowmetry," Journal of Medical Engineering & Technology 14(5), 178-181 (1990).
4. M. J. Leahy, F. F. M. de Mul, G. E. Nilsson, and R. Maniewski, "Principles and practice of the laser-Doppler perfusion technique," Technol Health Care 7(2-3), 143-162 (1999).
5. A. I. Krupatkin, and V. V. Sidorov, Laser Doppler flowmetry of Blood Microcirculation, Meditcina-Press, Moscow (2005).
6. M. Bracic, and A. Stefanovska, "Wavelet-based analysis of human blood-flow dynamics," Bulletin of Mathematical Biology 60(5), 919-935 (1998).
7. A. V. Tankanag, and N. K. Chemeris, "Application of the adaptive wavelet transform for analysis of blood flow oscillations in the human skin," Phys. Med. Biol. 53(21), 5967-5976 (2008).
8. J. R. Lakowicz (ed.), Principles of Fluorescence Spectroscopy, Kluwer Academic Publishers, 3rd ed., Springer, New York (2006). ISBN: 10 0-387-32278-1.
9. M. A. Mycek, and B. W. Pogue (eds.), Handbook of Biomedical Fluorescence, CRC Press, Taylor & Francis (2003). ISBN 978-0-824-70955-6.
10. D. Roblyer, R. A. Schwarz, and R. R. Richards-Kortum, "Fluorescence Spectroscopy," in Handbook of Biomedical Optics, D. A. Boas, C. Pitris, and N. Ramanujam, (eds.), CRC Press, Taylor & Francis, 217-232, (2011).
11. A. V. Dunaev, E. A. Zherebtsov, D. A. Rogatkin, N. A. Stewart, S. G. Sokolovski, and E. U. Rafailov, "Substantiation of medical and technical requirements for noninvasive spectrophotometric diagnostic devices," Journal of Biomedical Optics 18(10), 107009 (2013).

12. A. V. Dunaev, V. V. Dremin, E. A. Zherebtsov, I. E. Rafailov, K. S. Litvinova, S. G. Palmer, N. A. Stewart, S. G. Sokolovski, and E. U. Rafailov, "Individual variability analysis of fluorescence parameters measured in skin with different levels of nutritive blood flow," Medical Engineering and Physics 37(6), 574-583 (2015).
13. S. L. Jacques, "Optical properties of biological tissues: a review," Phys. Med. Biol. 58(11), R37-R61 (2013).
14. V. V. Dremin, and A. V. Dunaev, "How the melanin concentration in the skin affects the fluorescence-spectroscopy signal formation," Journal of Optical Technology 83(1), 43-48 (2016).
15. I. E. Rafailov, V. V. Dremin, K. S. Litvinova, A. V. Dunaev, S. G. Sokolovski, and E. U. Rafailov, "Computational model of bladder tissue based on its measured optical properties," Journal of Biomedical Optics 21(2), 025006 (2016).
16. I. Rafailov, S. Palmer, K. Litvinova, V. Dremin, A. Dunaev, and G. Nabi, "A novel excitation-emission wavelength model to facilitate the diagnosis of urinary bladder diseases," Proc. SPIE 9303, 93030W (2015).
17. V. V. Dremin, E. A. Zherebtsov, I. E. Rafailov, A. Y. Vinokurov, I. N. Novikova, A. I. Zherebtsova, K. S. Litvinova, A. V. Dunaev, "The development of attenuation compensation models of fluorescence spectroscopy signals," Proc. SPIE 9917, 99170Y (2016).
18. T. Binzoni, T. S. Leung, M. L. Seghier, and D. T. Delpy, "Translational and Brownian motion in laser-Doppler flowmetry of large tissue volumes," Physics in Medicine and Biology 49(24), 5445-5458 (2004).
19. I. Fredriksson, M. Larsson, F. Salomonsson, and T. Strömberg, "Improved calibration procedure for laser Doppler perfusion monitors," Proc. SPIE 7906, 790602 (2011).
20. A. Liebert, M. Leahy, and R. Maniewski, "A calibration standard for laser-Doppler perfusion measurements," Review of Scientific Instruments 66(11), 5169-5173 (1995).
21. M. Larsson, W. Steenbergen, and T. Stromberg, "Influence of optical properties and fiber separation on laser Doppler flowmetry," Journal of Biomedical Optics 7(2), 236-243 (2002).
22. E. A. Zherebtsov, A. I. Zherebtsova, A. V. Dunaev, and K. V. Podmaster'ev, "Method and device for metrological control of laser Doppler flowmetry devices," Biomedical Engineering 48(4), 191-195 (2014).
23. A. V. Dunaev, E. A. Zherebtsov, D. A. Rogatkin, N. A. Stewart, S. G. Sokolovski, and E. U. Rafailov, "Novel measure for the calibration of laser Doppler flowmetry devices," Proc. SPIE 8936, 89360D (2014).
24. V. V. Dremin, V. V. Sidorov, A. I. Krupatkin, G. R. Galstyan, I. N. Novikova, A. I. Zherebtsova, E. A. Zherebtsov, A. V. Dunaev, Z. N. Abdulvapova, K. S. Litvinova, I. E. Rafailov, S. G. Sokolovski, and E. U. Rafailov, "The blood perfusion and NADH/FAD content combined analysis in patients with diabetes foot," Proc. SPIE 9698, 969810 (2016).

1 Introduction

At present, optical non-invasive technologies [1], such as laser Doppler flowmetry (LDF) and fluorescence spectroscopy (FS) are widely utilized for the diagnosis of peripheral tissues, the assessment of blood microcirculation and biological tissue concentrations of enzymes. However, these technologies have a number of general problems unsolved today. In particular, the problems are low reliability and methodological limitations. This leads these methods having no wide and proper application in clinical practice. Thus, the solution to these problems of OND is to increase their efficiency and applicability in clinical practice. Possible ways to resolve the task can be improvement of the metrological assurance as well as further development of the instrumental tools. For example, the high-performance applications in clinical practice will allow us to identify the disease at level of tissue systems in the early stages of development. Undoubtedly it will reveal new horizons in the medicine of occupational diseases as well as reduce the risks of the socially significant diseases in the social and active segment of the population that will have a positive impact on the structure of the market of labour and the economy as a whole.

It is common knowledge that the LDF method is widely used in the research programs of various research teams and allows to estimate the intensity of peripheral blood flow in the microvasculature. The unit of measurement of the method in most cases is the index of microcirculation (I_m). The value of the index by convention is expressed in arbitrary perfusion units and is proportional to the average concentration of red blood cells (RBC) as well as their average velocity. Practically, the I_m is the result of processing of the signal from the photodetector, which is formed in photomixing of signals from the reference and frequency-shifts (in the band from 1 Hz to 24 kHz) due to the Doppler effect during scattering on RBC coherent light fluxes [2-4]. The time domain recorded signal of I_m consists of variable and constant components. The constant component - this is the mean perfusion of blood over a selected time interval. The variable component of the signal reflects the rhythms of frequency regulation of blood flow (fluxomotions) which appear due to the regulation of blood circulation and other physiological factors. Both components provide important information for diagnosing a number of diseases [5].

One of the weaknesses of the LDF method is its insufficient metrological support, leading to a lack of representation in medical practice. There is still no accurate, convenient and inexpensive tool (test object, optical phantom) to monitor the technical condition of LDF devices. Therefore, for the further development and wider application of the method in practice, it is vital to develop the system that can quantitatively

reproduce the reference and Doppler-shifted light fluxes in the correct proportions. The estimated test facility should provide an opportunity to quickly and comprehensively monitor the technical condition of both optical and electronic parts of the measurement channel. In particular, the system should reproduce the variable and constant components of the perfusion signal. It becomes important for the diagnosis of some diseases, that there is a need for accurate evaluation of fluctuations in vascular blood [6-7]. Thus, the level of the reproducible signal should be accurate and be able to vary in some range. Another important requirement is the versatility and ease of use.

Fluorescent spectroscopy (FS) is becoming more widely used in chemistry, biology, in various fields of medical technology and medicine in general. These methods are highly sensitive and provide a unique opportunity to study the excited states of molecules, photochemical reactions, dynamics of fast molecular processes, structures, and properties of complex biochemical and cellular systems. FS provides effective and non-invasive optical diagnostics, primarily in medical areas such as oncology, transplantation, cosmetology and surgery. The FS method is based on exciting fluorescence from tissue endogenous and exogenous fluorophores and recording the emission in the visible spectral region [8-9]. FS is a good method to differentiate benign and malignant tumours of various origins [10]. FS is also used as a tool to monitor the dynamics of the processes occurring in the tissues, during cancer treatments such as radiotherapy. Many purulent wounds, burns and other destructive inflammatory processes are accompanied by changes in the fluorescent activity of the tissues, which occurs due to a misbalance in accumulation of natural fluorophores: FAD, NADH, lipofuscin, porphyrins, structural proteins, etc.

However, fluorescence spectroscopy of biological tissue is a complicated technique that depends on the temperature, topological heterogeneity, different properties of each sample, etc. Therefore, the reliability of FS is affected by multiple factors, including the availability of data concerning the scattering and absorbing properties of specific tissues in specific conditions, light pollution at the optical fibre tip and instrument errors such as excitation source instability, photo-detector limitations, light filter precision, grating precision, CCD performance, etc. This study aims to fill some gaps in the FS method.

The study conducted by the authors represents an attempt at forming a comprehensive, systematic and unifying approach of solving the above mentioned problems of the diagnostic methods. The problems of accuracy, variation and reproducibility of measurements are investigated. The obtained results can improve the reliability of clinical diagnostic results by the methods of FS and LDF. To assess the variability of the diagnostic parameters obtained by FS and LDF methods appropriate experimental studies have been conducted. As main equipment, the multifunction laser diagnostic system “LAKK-M” (SPE “LAZMA” Ltd., Russia) was chosen. The experiments were conducted with the participation of healthy volunteers. Comparative analysis of the collected data showed that the relative variation of the parameters for all volunteers has the quite homogeneous mean level and can range from 10 to 40% depending on the determined parameter. It has been found that total scatter and, consequently, the final diagnostic result can be affected by several factors. Thus, the blood supply of the biological tissue affects both attenuation of the intensity of the exciting radiation and the excited fluorescence radiation [11, 12].

Also, the effect of melanin on the fluorescence signal was investigated. This skin component is one of the most important natural pigments and has a significant impact on the optical properties of the skin. Influence of melanin was assessed in different ethnic skin types, including European, Indian, Arabic and African [13]. It is found that with increasing the melanin concentration the fluorescence signal decays monotonically. For the tasks of medical instrument engineering recommendations about the influence of the effect on signal-to-noise ratio of the photodetector were given [12, 14].

In order to describe and predict the effects of the above factors on the obtained FS spectrum, a Monte Carlo model of propagation of optical radiation in epithelial biological tissues was developed [12, 14-17]. Such an approach to solve this problem seems to be prospective and shows good accuracy of the modelling results.

2 New approaches of metrological support of devices for laser Doppler flowmetry

At present, as a test objects for the LDF measurements, colloidal solutions of light-scattering particles are most widely used. The tissue phantoms simulate the movement of RBC by Brownian motion of the microparticles of certain size and concentration. The speed of Brownian motion is calculated from the theoretical dependences on temperature as well as particle shape parameters [18-20]. An example of such calibration system is the test object “Motility Standard” (Perimed AB, Sweden) [21]. However, the test object is not stable in time and undergoes desiccation. In addition, the test object can reproduce only one level of the perfusion.

Conducted experimental research of the colloid solution standard together with LDF-channel (single mode laser, wavelength 1064 nm) of “LAKK-M” system demonstrated significant methodological shortcomings of this approach. The results of periodic monitoring of the reproduced level of LDF signal for channel “LAKK-M” by “Motility Standard” during 8 months is presented at Figure 1.

The fibre optic probe of the reference LDF channel was submerged in the solution and the reproduced signal was recorded for 30-minute. One possible reason for obtaining a sufficiently large spread of results is that the solution has changed their characteristics over time (its shelf life is no more than six months). Also, significant drawback of this approach of calibration is the enormous sensitivity to any vibration of the surface table. To overcome the described problems new

approach for monitoring the technical condition of the LDF instruments was proposed.

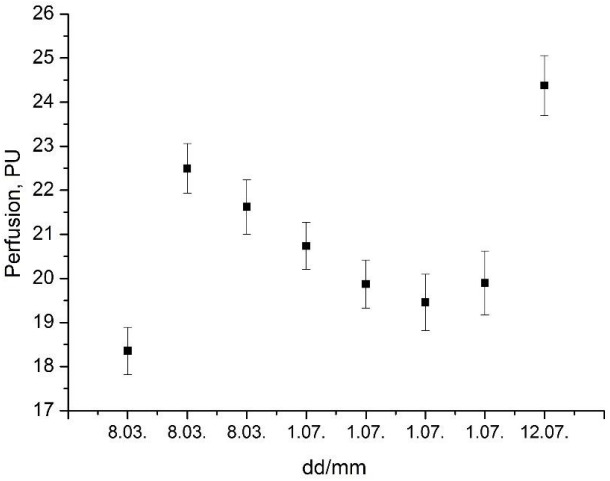

Fig. 1 The results of periodic monitoring of the reproduced level of LDF signal by "Motility Standard" (Perimed AB, Sweden).

The approach is based on the use of a new test object. General view of the setup is presented at Figure 2a. In the setup quantitatively reproducing of the reference and Doppler-shifted light fluxes is provided by the scattering on oscillating standard Lambertian reflector covered by immovable semi-transparent glass plate. The main basis of operation is presented at Figure 2b. The electromechanical transducer 3 converts electrical signal into mechanical vibrations in the moving diffuse reflector 2. In order to create a constant component of the signal, laser radiation from the probe fiber (aperture of source S_{in}) passes first through a fixed semi-transparent plane-parallel plate 1. The reflected back from the plate radiation does not undergo Doppler shift. Laser radiation is scattered by oscillating diffusing Lambertian surface and receives the component of the Doppler shift. Both radiation fluxes are collected by receiving fiber with aperture S_{out} and processed by the checked LDF device. The reflector 2 is driven by high-precision piezo actuator with the oscillation frequency of 0 to 100 Hz. In that way, this test facility realized the possibility of reproducing a constant level of perfusion as well as blood filling fluctuations (fluxmotions) in the microvasculature in the frequency range of 0.01 to 2 Hz. By varying modes of operation, it is possible to simulate a variety of patterns of LDF signal. Thus, the approach provides the tool of checking during one procedure both optical and electronic parts of the measurement channel. This test facility allows to make a technical check of the device as well as metrological control of its condition [22, 23]. No doubt further improvement of the metrological provision of LDF method will rise this diagnostic technology to a new level of effectiveness and reliability.

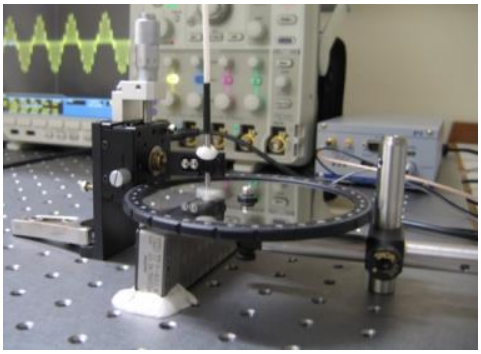

(a)

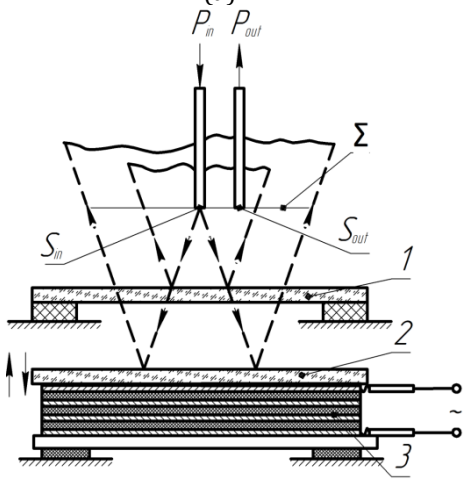

(b)

Fig. 2 The experimental setup for metrological check of LDF devices based on the oscillating standard Lambertian reflector: (a) general view; (b) the main basis of operation:
1 – semi-transparent plane-parallel plate, 2 – moving diffuse reflector, 3 – electromechanical transducer (batch piezoelectric actuator), S_{in} – aperture of source, S_{out} – aperture of the receiver, Σ – plane coincidence of aperture of receiver and source.

3 Problem with methodological and instrumentation provision of fluorescence spectroscopy for medicine

Experiments were conducted to assess the performance of 2 identical FS-channels. Measurements were conducted on a solution of porphyrin in PBS solution. The cuvette with the biomarker was placed on a white PTFE reflection standard. A concentration of 0.25 mM was used. The depth of immersion of the fibres in the cuvette was about 5 mm. Figure 3 shows some porphyrin fluorescence spectra (Figure 3a and 3b for green (532 nm) and red (635 nm) fluorescence excitation lines respectively).

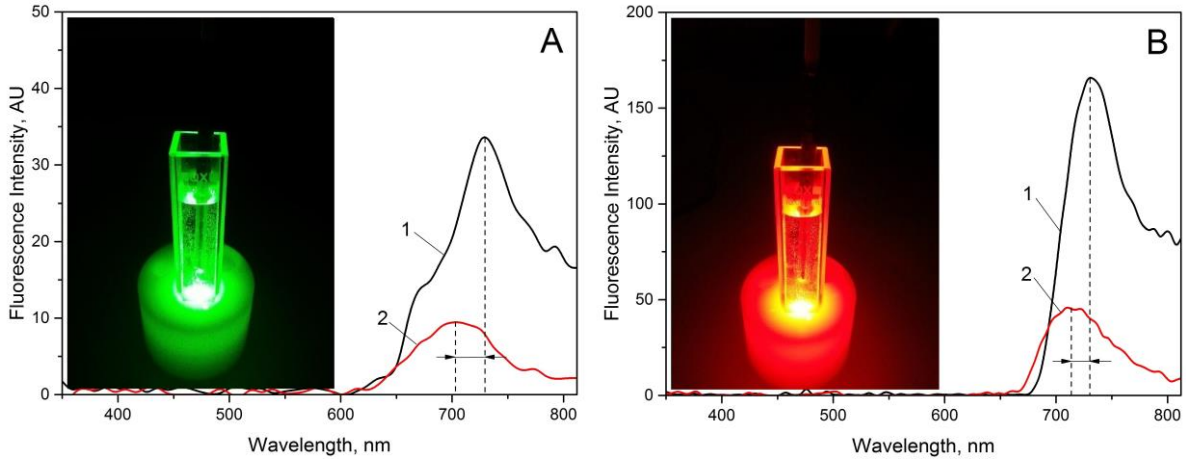

1 – Device №1; 2 – Device №2

Fig. 3 Examples of fluorescence spectra: for porphyrin on the green (a) and red (b) lines excitation.

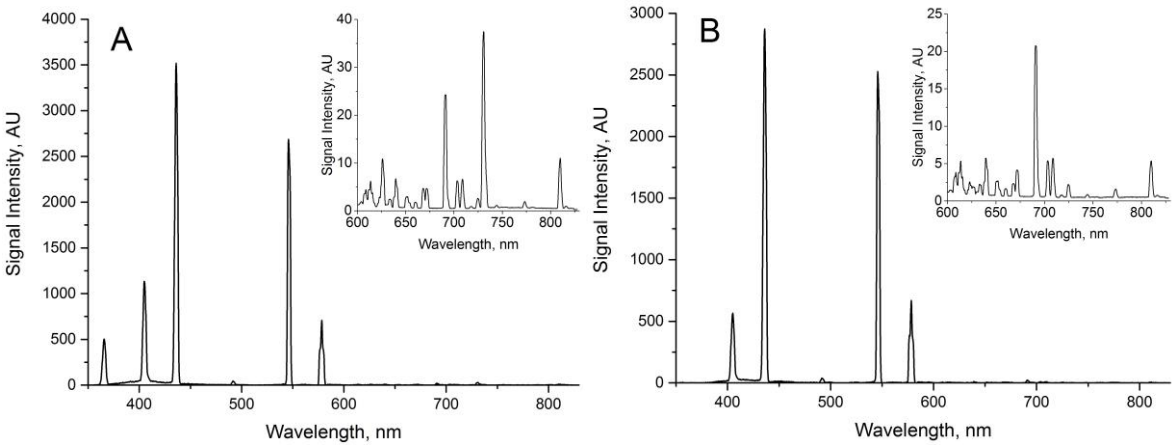

Fig. 4 The registered spectrum of mercury lamp without a filter (a) and with UV filter (b).

In addition to physical errors, there were also a number of technical errors in the method. Thus, even the minor parameter changes in optical radiation of the device, differences between separate receiver sites and individual nodes of the optical system, may visibly influence the shape of the spectral curve and, consequently, the final diagnostic result when measuring the fluorescent spectra. In the figures, dotted lines represent the peaks of fluorescent biomarkers.

As seen in Figure 3, for the two compared FS channels fluorescence intensity values differ greatly in amplitude. The reason for this may be a different spectral sensitivity of the transfer function and resolution of different diagnostic instruments, since cell CCD arrays have unequal sensitivity, i.e. even if the signal is homogeneous, illumination produced is different. The magnitude of this heterogeneity is typically less than 5%. However, this does not eliminate the problem of reducing CCD noise itself, as fluorescent applications often work with the signals in the tens of photons per cell. For this reason, in systems which require high photometric accuracy such as this, it is necessary to apply the same non-uniformity correction algorithms as well as adjusting dark current. Spectral characteristics of the CCD, however small, affect the quality of the signal. Often, the output electronic cascades are an even more intense source of noise. In this regard, attention should be paid to the rational matching of a receiver and a follow-up system.

As mentioned above, the different nodes of the optoelectronic system appear to be the primary sources of noise, interference and other distortion. Thus, a set of interchangeable filters is installed on the input of the devices polychromator, damping the radiation at given source wavelengths to required levels. As studies have shown with use of a mercury gauge lamp (Fig.4), utilised filters affect the sensitivity of the measurement channel. More specifically, they weaken not only the backscattered radiation, but the fluorescence emission of various fluorophores, which affects the whole recorded spectra and calculated parameters.

One may infer the need for more precise filters with a narrow band filter and a high percentage transmittance of other wavelengths. Based on the received results, we can conclude on the need to develop methods of metrological monitoring for FS devices. Metrological provision should cover both the spectral calibration of the instrument readings and the normalisation of quantitative fluorescence, based on modelling the endogenous fluorescence of the investigated fluorophores. Creation of new FS hardware also requires new approaches to software development for

the processing and analysis of diagnostic information to develop practical methods for its application in applied clinical medicine. It should be emphasized that addressing the issues of metrological support for the FS method can bring this diagnostic technology to a new level.

4 Conclusion

The presented results demonstrate the relevance of instrumentation, methodological and metrological provision for these technologies in general and especially for the medical application of the LDF- and FS-devices and combined systems. The combined use of OND technologies with functional (provocative) tests allows increasing the repeatability of results and accuracy of diagnostics (for example, LDF and FS methods allows to predict the development of trophic disorders and the diabetic foot syndrome on the more early stages) [24]. Further problem solving of the outlined issues will bring OND closer to standardized diagnostic technologies and to wider application in real medical practice.

Acknowledgments

This work was supported by Russian Foundation for Basic Research (grant №16-32-00662 mol_a) and partially by grant of the President of the Russian Federation for state support of young Russian scientists № MK-7168.2016.8.

Optical properties of human nails in THz frequency range

Victoria A. Guseva, Sviatoslav I. Gusev*, Petr S. Demchenko, Egor A. Sedykh, and Mikhail K. Khodzitsky

Laboratory of THz Biomedicine, ITMO University, 49 Kronverksky Pr., St.Petersburg 197101, Russian Federation

***e-mail:** mail@gusev-spb.ru

Abstract. This work is devoted to investigation of optical properties (dispersion of refractive index, permittivity and absorption coefficient) of human nails in THz frequency range. These data were obtained by THz time-domain spectroscopy (TDS) technique in transmission mode. These results may be used to develop non-invasive technique of human pathologies control using nail as a reference sample in reflection mode of THz TDS. © 2016 Journal of Biomedical Photonics & Engineering.

Keywords: spectroscopy, nail, refractive index, permittivity, absorption, penetration depth

Paper #3146 received 2016.11.31; accepted for publication 2016.12.29; published online 2016.12.31. doi: 10.18287/JBPE16.02.040306. [Saratov Fall Meeting 2016 Special Issue].

References

1. Classification and Diagnosis of Diabetes, Diabetes Care 38(Supplement_1), S8–S16 (2014).
2. A. Ceriello, and S. Colagiuri, "International Diabetes Federation guideline for management of postmeal glucose: a review of recommendations," Diabetic Medicine 25(10), 1151–1156 (2008).
3. L. Northam, and G. Baranoski, "A novel first principles approach for the estimation of the sieve factor of blood samples," Optics express 18(7), 7456–7469 (2010).
4. V. V. Tuchin, Tissue Optics: Light Scattering Methods and Instruments for Medical Diagnostics, SPIE-Intl Soc Optical Eng (2015). ISBN: 9780819495860
5. D. P. Popescu, and M. G. Sowa, "In Vitro Assessment of Optical Properties of Blood by Applying the Extended Huygens-Fresnel Principle to Time-Domain Optical Coherence Tomography Signal at 1300 nm," International Journal of Biomedical Imaging 2008, 1–6 (2008).
6. D. Yim, G. V. G. Baranoski, B. W. Kimmel, T. F. Chen, and E. Miranda, "A Cell-Based Light Interaction Model for Human Blood," Computer Graphics Forum 31(2pt4), 845–854 (2012).
7. A. Fitzgerald, E. Berry, N. Zinov'ev, S. Homer-Vanniasinkam, R. Miles, J. Chamberlain, and M. Smith, "Catalogue of human tissue optical properties at terahertz frequencies," Journal of Biological Physics 29(2-3), 123–128 (2003).
8. E. Pickwell, B. E. Cole, A. J. Fitzgerald, M. Pepper, and V. P. Wallace, "In vivo study of human skin using pulsed terahertz radiation," Physics in Medicine and Biology 49(9), 1595–1607 (2004).
9. P. H. Siegel, "Terahertz Technology in Biology and Medicine," IEEE Transactions on Microwave Theory and Techniques 52(10), 2438–2447 (2004).
10. J.-H. Son, Terahertz Biomedical Science and Technology, CRC Press (2014). ISBN 9781466570443
11. S. I. Gusev, M. A. Borovkova, M. A. Strepitov, and M. K. Khodzitsky, "Blood optical properties at various glucose level values in THz frequency range," Proc. SPIE 9537, 95372A (2015).
12. S. I. Gusev, N. S. Balbekin, E. A. Sedykh, Y. A. Kononova, E. V. Litvinenko, A. A. Goryachuk, V. A. Begaeva, A. Y. Babenko, E. N. Grineva, and M. K. Khodzitsky, "Influence of creatinine and triglycerides concentrations on blood optical properties of diabetics in THz frequency range," Journal of Physics: Conference Series 735, 012088 (2016).
13. A. Pashkin, M. Kempa, H. Němec, F. Kadlec, and P. Kužel, "Phase-sensitive time-domain terahertz reflection spectroscopy," Review of Scientific Instruments 74(11), 4711–4717 (2003).
14. M. M. Nazarov, A. P. Shkurinov, E. A. Kuleshov, and V. V. Tuchin, "Terahertz time-domain spectroscopy of biological tissues," Quantum Electronics 38(7), 647–654 (2008).

15. V. G. Bespalov, A. A. Gorodetskiĭ, I. Y. Denisyuk, S. A. Kozlov, V. N. Krylov, G. V. Lukomskiĭ, N. V. Petrov, and S. É. Putilin, "Methods of generating superbroadband terahertz pulses with femtosecond lasers," Journal of Optical Technology 75(10), 636–642 (2008).

1 Introduction

Diabetes mellitus is a group of metabolic diseases characterized by hyperglycemia resulting from defects in insulin secretion, insulin action, or both [1]. The chronic hyperglycemia of diabetes is associated with long-term damage, dysfunction, and failure of various organs, especially the eyes, kidneys, nerves, heart, and blood vessel. Accurate and efficient assessment of blood glucose concentration is critical in clinical management of many pathological conditions in human population. There is a direct relationship between the level of glucose in the blood of patients with diabetes and the probability of developing complications of the disease [2].

Optical properties of whole blood are important parameters in biophysical investigations and medical diagnostics. Variations in cellular and biochemical composition of whole blood markedly affect the values of different optical parameters (absorption, scattering, index of refraction etc.) [3-7].

One of the most important benefit of spectroscopy methods is the possibility of non-invasive analysis of media.8 Transmission mode of spectroscopy is common way for collecting data about easy extractable media [9, 10]. On the one hand transmission mode of medium analysis provides accurate results, but can be unsuitable for completely non-invasive investigation of biological tissues and fluids [11, 12]. On the other hand, reflection mode of spectroscopy cannot be used for direct blood optical measurement due to the location of blood below the surface of the human body [13]. Moreover, THz reflected signal considerably weakened due to the water contained in the skin layer. Despite this, capillar blood located in fingers' nail beds may be investigated through the nails in the reflection mode (see Fig. 1).

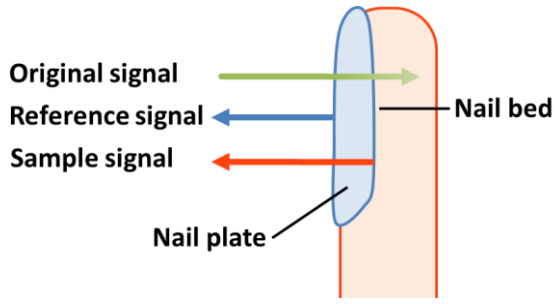

Fig. 1 Scheme of non-invasive reflective spectroscopy of the capillar blood inside the nail bed.

At this variant of reflective spectroscopy, it is need to know optical properties of nail plate for analysis of nail bed spectral data. It is not enough papers with detailed data about optical properties of human nails in THz frequency range. For example, in the Ref. [14] it was shown only refractive index and dispersion of absorption coefficient of nails. This work is dedicated to retrieve optical properties of human nails for purposes of non-invasive glucose measuring technology.

2 Experimental setup

The optical properties of nail plates were studied in the frequency range of 0.1-1 THz using time-domain spectrometer in transmission mode [11, 15]. The scheme of the setup is shown in the Fig. 2.

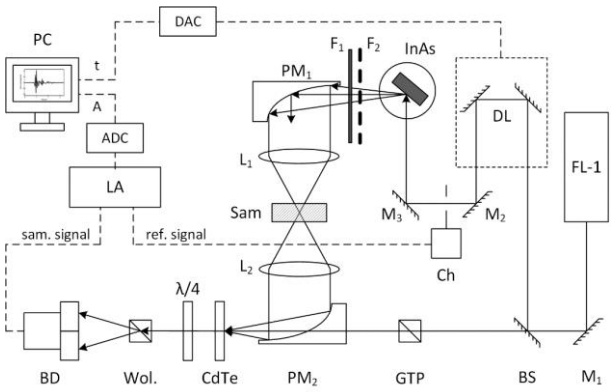

Fig. 2 Schematic diagram of the set up (FL-1 – femtosecond laser based on potassium-yttrium tungstate crystal activated with ytterbium (Yb: KYW), generating femtosecond pulses; F1, 2 – a set of teflon filters for IR wavelength range cutting off, BS – beamsplitter, DL – optical delay line, $M_{1, 2, 3}$ – mirrors, Sam – investigated sample, Wol. – Wollaston prism, CdTe – electro optical cadmium-telluric crystal, BD – balanced detector, LA – lock-in amplifier, PC – personal computer, GTP – Glan-Taylor prism, $PM_{1, 2}$ – parabolic mirrors, Ch – chopper, DAC – digital to analog converter, ADC – analog to digital converter

Broadband pulsed THz radiation is generated using a InAs semiconductor in the magnetic field of 2 T by irradiating it with femtosecond pulses of an Yb: KYW laser (wavelength of 1040 nm, the pulse duration of 120 fs, the pulse repetition frequency of 75MHz, the power of 1 W). THz radiation has the following output characteristics: the spectral range from 0.05 to 2 THz, the average power up to 30 μW, the pulse duration of 2.7 ps. The main power is concentrated at the frequency range from 0.12 to 1.1 THz. THz radiation passes through a teflon filter (which cuts the wavelengths shorter than 50 μm). After that, the radiation passes through the sample fixed in a focal plane perpendicularly to the beam. THz sample pulse affects on the anisotropy of the electrooptical CdTe crystal. As a result, THz pulse induces birefringence of the probe

beam in the crystal due to the electrooptical effect. The birefringence magnitude is directly proportional to the intensity of terahertz wave electric field in the time point E(t). These data are required to calculating E(ω) using Fourier transform.

3 Sample preparation

There are 10 different nails measured at this experiment. The nail samples were taken from hands of man corpse (Fig. 3).

Fig. 3 Investigated nail samples.

Thicknesses of each nail were measured 10 times with micrometer. This feature helps to decrease error caused by thickness measuring (the most significant error in transmissive TDS of thin structures). Determination of samples thicknesses is shown in Table 1.

Each sample of nail plate was prepared for recording of transmission time-amplitude signal: there were the same zones of nail plates for thickness measuring and signal transmission (Fig. 4). The diameter of the THz pulse spot is 3 mm. Dried nail plates had not any other specific treatment before experiment.

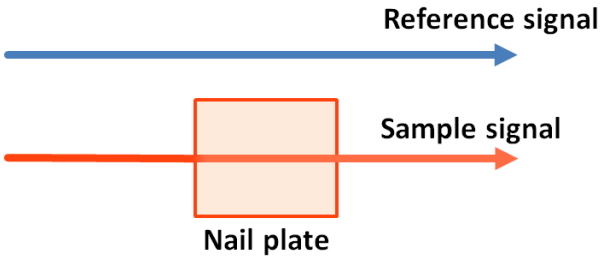

Fig. 4 Scheme of recording time-amplitude signal.

Table 1 Measured thickness values of nails, used in experiment.

Exp. №	Thickness of sample №x, μm									
	1	2	3	4	5	6	7	8	9	10
1	450	420	450	410	420	460	410	430	430	360
2	460	410	420	440	410	490	370	450	460	390
3	520	460	410	390	450	470	480	410	470	390
4	430	450	430	410	380	490	460	420	460	410
5	490	440	410	400	390	490	460	430	440	430
6	510	450	480	450	420	490	400	390	430	380
7	490	420	420	420	440	470	400	390	450	430
8	460	460	430	400	450	470	410	430	460	330
9	480	450	420	400	410	490	400	400	450	440
10	540	450	420	410	420	480	390	420	440	430
Average	483±27	441±15	429±15	413±14	419±17	480±10	418±29	417±16	449±11	399±29

4 Data acquisition

For each sample, a time-amplitude transmission waveform was taken 100 times and averaged for each timepoint. Also it was taken reference transmission waveform of air. All the acquired reference and sample waveforms were converted by Fourier transformation into $E_{ref}(\omega)$ and $E_{sam}(\omega)$, respectively. Then the THz electric field is:

$$\hat{E}(\omega) = \frac{1}{\sqrt{2\pi}} \int_{-\infty}^{+\infty} f(t)\, e^{-i\omega t} dt = E_0(\omega) e^{-i\varphi(\omega)} \quad (1)$$

where f(t) is the time-amplitude waveform, ω is the angular frequency, $E_0(\omega)$ is the amplitude data, φ(ω) is phase data.

The real part of refractive index n_{real} calculated as:

$$n_{real}(f) = 1 + \frac{c\left(\varphi_{sam}(f) - \varphi_{ref}(f)\right)}{2\pi l f} \quad (2)$$

where c is the speed of light in vacuum, l is the thickness of medium, f is the frequency.

The absorption coefficient α is calculated using the amplitude data:

$$\alpha(f) = \frac{1}{l} ln\left(\frac{E_{0\,ref}(f)}{E_{0\,sam}(f)}\right)^2 \quad (3)$$

The penetration depth L is reverse function to the absorption coefficient $\propto$.

The imaginary part of the refractive index $n_{imag}(f)$ requires data about the absorption coefficient $\propto$:

$$n_{imag}(f) = \frac{\mu(f)\, c}{4\pi f} \quad (4)$$

Both parts of the complex permittivity ε use both parts of the refractive index n:

$$\varepsilon_{real}(f) = n_{real}^2(f) - n_{imag}^2(f) \quad (5)$$

$$\varepsilon_{imag}(f) = 2\, n_{real}(f)\, n_{imag}(f) \quad (6)$$

All of these optical properties available as results of Spectrina software [11].

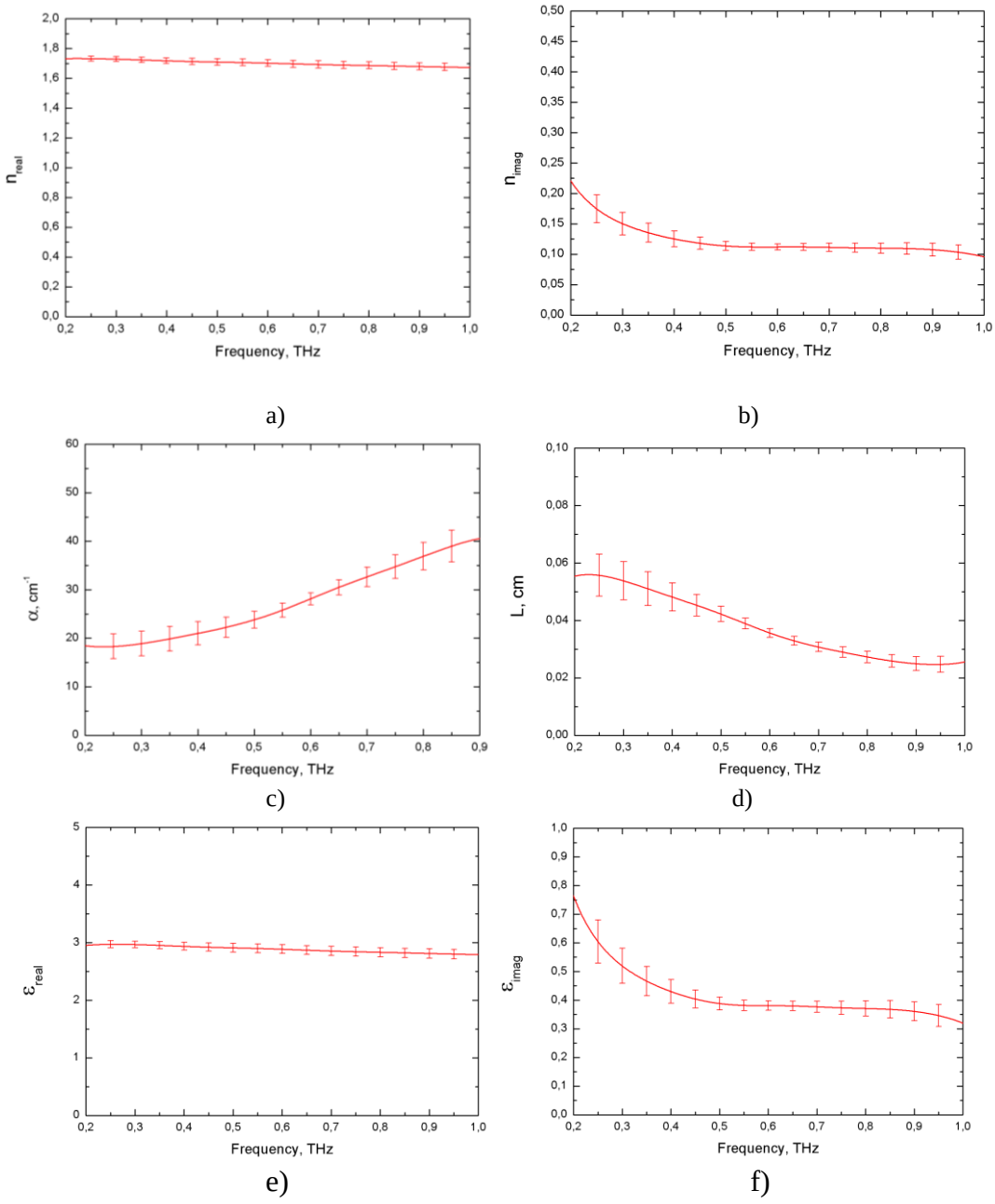

Fig. 5 Frequency dispersions of optical propreties of: a) real part of refractive index $n_{real}(f)$, b) imaginary part of refractive index $n_{imag}(f)$, c) absorption coefficient μ(f), d) penetration depth $L(f)$, e) real part of permittivity $\varepsilon_{real}(f)$, f) imaginary part of permittivity $\varepsilon_{imag}(f)$.

5 Results and Discussions

Based on 10 samples, we investigated the frequency dispersions of n_{real}, n_{imag}, $\propto$, L, ε_{real}, ε_{imag} in the frequency range of 0.2 to 1.0 THz (see Fig. 5).

Enough amount of samples and measurements provides the result with a low level of error. The real part of refractive index has stable value of 1.70 ± 0.03 in the frequency range of 0.2 – 1.0 THz. The imaginary part of refractive index has inverse ratio on frequency in the frequency ranges of 0.2 – 0.5 THz (from 0.22 ± 0.03 to 0.11 ± 0.01) and of 0.9 – 1.0 THz (from 0.11 ± 0.01 to 0.10 ± 0.01), but has fixed value of 0.11 ± 0.01 at the frequency range of 0.5 – 0.9 THz. The absorption coefficient has direct ratio on frequency in the frequency range of 0.2 – 0.9 THz (from 18 ± 3 cm^{-1} to 40 ± 4 cm^{-1}). The penetration depth has inverse correlation with frequency in the frequency range of 0.2 – 0.9 THz (from 0.055 ± 0.008 cm to 0.025 ± 0.002 cm). The real part of permittivity has stable value of 2.89 ± 0.08 in the frequency range of 0.2 – 1.0 THz. The imaginary part of permittivity has inverse ratio on frequency in the frequency ranges of 0.2 – 0.5 THz (from 0.76 ± 0.10 to 0.39 ± 0.02) and 0.9 – 1.0 THz (0.36 ± 0.03 to 0.32 ± 0.04) and fixed value of 0.38 ± 0.02 in the frequency range of 0.5 – 0.9 THz.

These results are dispersions, but not constants. At the same time, some frequency ranges with stable value are suitable for using nail as reference medium. Moreover, all 10 measured nail plates have same optical properties within the margin of error. The absorption coefficient of nail plates increases with the frequency increasing. Therefore, using of low frequency of THz range is more efficient for measuring glucose levels.

In the Ref. [14] it was shown only the refractive index and the dispersion of the absorption coefficient obtained using reflection THz TDS in the frequency range of 0.25 – 2.0 THz. It this paper we obtained all optical properties as dispersions such as the complex refractive index n(f), the absorption coefficient α(f), the penetration depth L(f), the complex permittivity ε(f).

6 Conclusion

The dispersions of nail plates optical properties (the complex refractive index n(f), the absorption coefficient α(f) , the penetration depth L(f) , the complex permittivity ε(f)) were obtained in the frequency range of 0.2 – 1 THz by THz TDS. These data will be helpful for development of the reflective non-invasive spectroscopic method of blood glucose measuring technique. Due to the radiation penetration depth is more than the nail plate thickness in the frequency range of 0.2 – 0.5 THz, that the radiation of this range can be used for nail bed investigation. Nail could be used as reference layer for investigation of capillar blood by reflection THz TDS.

Acknowledgments

This work was financially supported by the Government of Russian Federation, Grant 074-U01.

Wavelength dependence of the refractive index of human colorectal tissues: comparison between healthy mucosa and cancer

Sónia Carvalho[1], Nuno Gueiral[2,3], Elisabete Nogueira[2,3], Rui Henrique[1,4], Luís Oliveira[2,3*], and Valery V. Tuchin[5,6,7]

[1] Department of Pathology and Cancer Biology and Epigenetics Group-Research Centre, Portuguese Oncology Institute of Porto, Rua Dr. António Bernardino de Almeida S/N, 4200-072 Porto, Portugal

[2] School of Engineering, Physics Department, Polytechnic Institute of Porto, Rua Dr. António Bernardino de Almeida, 431, 4200-072 Porto, Portugal

[3] Centre of Innovation in Engineering and Industrial Technology, ISEP, Rua Dr. António Bernardino de Almeida, 431, 4200-072 Porto, Portugal

[4] Department of Pathology and Molecular Immunology, Institute of Biomedical Sciences Abel Salazar – University of Porto (ICBAS-UP), Rua de Jorge Viterbo Ferreira nº228, 4200-072 Porto, Portugal

[5] Research-Education Institute of Optics and Biophotonics, Saratov National Research State University, 83 Astrakhanskaya str., Saratov 410012, Russia

[6] Laboratory of Laser Diagnostics of Technical and Living Systems, Precision Mechanics and Control Institute of the Russian Academy of Sciences, 24 Rabochaya, Saratov 410028, Russia

[7] Interdisciplinary Laboratory of Biophotonics, National Research Tomsk State University, 36 Lenin's av., Tomsk 634050, Russia

***e-mail:** lmo@isep.ipp.pt

Abstract. Biological tissues have individual optical properties that may be used as an identity card. The refractive index in particular, which can be measured directly, is very significant for the improvement or development of optical technologies in clinical practice. With the objective of verifying if healthy and pathological tissues can be discriminated from refractive index measurements, we have studied human colorectal mucosa. By using the total internal reflection method to measure the refractive index from healthy and pathological colorectal mucosa tissues at different wavelengths, it was possible to calculate the dispersion curves for both types of tissues. It was observed a decaying refractive index with wavelength, both for healthy and pathological tissues, which were fitted with curves described by Cornu's equation for wavelengths between ultraviolet and near-infrared range. Experimental results show higher refractive index values for the pathological mucosa for all wavelengths. By performing measurements at wavelengths near 850 nm, we have detected non-monotonic behavior for the refractive index of both healthy and pathological tissues. Such abnormal wavelength dependence is evidence of lipids in both tissues. The acquired experimental data demonstrated that it is possible to discriminate between healthy and pathological tissues from refractive index measurements. Similar studies can be made for different biological tissues. By using lasers with different wavelengths it might be possible to identify other tissue components.

Keywords: Colorectal tissue, Cancer, Refractive index, Total internal reflection, Tissue dispersion

Paper #3130 received 2016.12.02; accepted for publication 2016.12.29; published online 2016.12.31. doi: 10.18287/JBPE16.02.040307. [Saratov Fall Meeting 2016 Special Issue].

References

1. J.-C. Lai, Z. Li, C. Wang, and A. He, "Experimental measurement of the refractive index of biological tissues by total internal reflection," Applied Optics 44(10), 1845–1849 (2005).
2. V. V. Tuchin, Tissue Optics: Light Scattering Methods and Instruments for Medical Diagnosis, 3rd Ed., Bellingham, SPIE Press (2015).
3. T. Vo-Dinh, Biomedical Photonics Handbook, CRC Press (2003).
4. P. Giannios, S. Koutsoumpos, K. G. Toutouzas, M. Matiatou, G. C. Zografos, and K. Moutzouris, "Complex refractive index of normal and malignant human colorectal tissue in the visible and near-infrared," J. Biophotonics (2016).
5. F. P. Bolin, L. E. Preuss, R. C. Taylor, and R. J. Ference, "Refractive index of some mammalian tissues using a fiber optic cladding method," Applied Optics 28(12), 2297-2303 (1989).
6. H. Li, and S. Xie, "Measurement method of the refractive index of biotissue by total internal reflection," Applied Optics 35(10), 1793-1795 (1996).
7. Q. Ye, J. Wang, Z.-C. Deng, W.-Y. Zhou, C.-P. Zhang, and J.-G. Tian, "Measurement of the complex refractive index of tissue-mimicking phantoms and biotissue by extended differential total reflection method," J. Biomedical Optics 16(9), 097001-1-5 (2011).
8. J.-C. Lai, Y.-Y. Zhang, Z.-H. Li, H.-J. Jiang, and A.-Z. He, "Complex refractive index measurement of biological tissues by attenuated total reflection ellipsometry," Applied Optics 49(16), 3235-3238 (2010).
9. H. Ding, J. Q. Lu, K. M. Jacobs, and X.-H. Hu, "Determination of refractive indices of porcine skin tissues and intralipid at eight wavelengths between 325 and 1557 nm," J. Opt. Soc. Am. A 22(6), 1151-1157 (2005).
10. Y. L. Jin, J. Y. Chen, L. Xu, and P. N. Wang, "Refractive index measurement for biomaterial samples by total internal reflection," Phys. Med. Biol. 51(20), N271-N379 (2006).
11. J. J. J. Dirckx, L. C. Kuypers, and W. F. Decraemer, "Refractive index of tissue measured with confocal microscopy," J. Biomed. Opt. 10(4), 044014-1-8 (2005).
12. Z. Wang, K. Tangella, A. Balla, and G. Popescu, "Tissue refractive index as marker of disease," J. Biomed. Opt. 16(11), 116017-1-7 (2011).
13. Y. Zhou, K. K. H. Chan, T. Lai, and S. Tang, "Characterizing refractive index and thickness of biological tissues using combined multiphoton microscopy and optical coherence tomography," Biomedical Optics Express 4(1), 38-50 (2013).
14. J. Sun, S. J. Lee, L. Wu, M. Sarntinoranont, and H. Xie, "Refractive index measurement of acute rat brain tissue slices using optical coherence tomography," Optics Express 20(2), 1084-1095 (2012).
15. H. Brenner, M. Kloor, and C. P. Pox, "Colorectal cancer," The Lancet 383(9927), 1490-1502 (2014).
16. S. D. Curran, and L. H. Schwartz, "Colorectal cancer imaging" in Colorectal Cancer: Evidence-based Chemotherapy Strategies, L. B. Saltz (ed.), Humana Press, New Jersey, USA, 219-230 (2007).
17. A. M. Lacy, J. C. García-Valdecasas, S. Delgado, A. Castells, P. Taurá, J. M. Piqué, and J. Visa, "Laparoscopy-assisted colectomy versus open colectomy for treatment of non-metastatic colon cancer: a randomized trial," The Lancet 359(9325), 2224-2229 (2002).
18. R. Subramaniam, A. Mizoguchi, and E. Mizoguchi, "Mechanistic roles of epithelial and immune cell signaling during the development of colitis-associated cancer," Cancer Research Frontiers 2(1), 1-21 (2016).
19. A. Pierangelo, A. Benali, M.-R. Antonelli, T. Novikova, P. Validire, B. Gayet, and A. De Martino, "Ex-vivo characterization of human colon cancer by Mueller polarimetric imaging," Optics Express 19(2), 1582-1593 (2011).
20. J. Wang, Z. Deng, X. Wang, Q. Ye, W. Zhou, J. Mei, C. Zhang, and J. Tian, "Measurement of the refractive index of hemoglobin solutions for a continuous spectral region," Biomedical Optics Express 6(7), 2536-2541 (2015).
21. H. Ding, J. Q. Lu, W. A. Wooden, P. J. Kragel, and X.-H. Hu, "Refractive indices of human skin tissues at eight wavelengths and estimated dispersion relations between 300 and 1600 nm," Phys. Med. Boil. 51(6), 1479-1489 (2006).
22. http://refractiveindex.info/
23. Z. Deng, J. Wang, Q. Ye, T. Sun, W. Zhou, J. Mei, C. Zhang, and J. Tian, "Determination of continuous complex refractive dispersion of biotissue based on internal reflection," J. Biomed. Opt. 21(1), 015003 (2016).
24. http://omlc.org/spectra/
25. S. Takatani, and M. D. Graham, "Theoretical analysis of diffuse reflectance from a two-layer tissue model," IEEE Trans. Biomed. Eng. 26(12), 656-664 (1979).
26. G. M. Hale, and M. R. Querry, "Optical constants of water in the 200 nm to 200 μm wavelength region," Appl. Opt. 12(3), 555-563 (1973).
27. R. L. P. van Veen, H. J. C. M. Sterenborg, A. Pifferi, A. Torricelli, E. Chikoidze, and R. Cubeddu, "Determination of VIS-NIR absorption coefficients of mammalian fat, with time- and spatially resolved diffuse reflectance and transmission spectroscopy," J. Biomed. Opt. 10(5), 054004-1-6 (2005).

28. R. Nachabé, B. H. W. Hendriks, M. van der Voort, A. E. Desjardins, and H. J. C. M. Sterenborg, "Estimation of biological chromophores using diffuse optical spectroscopy: benefit of extending the UV-VIS wavelength range to include 1000 to 1600 nm," Optics Express 18(24), 1432–1442 (2010).

1 Introduction and theoretical background

In the growing research field of Biomedical Photonics, the knowledge of the refractive index (RI) of biological tissues and fluids is highly necessary to understand and describe how light propagates and interacts with tissue components [1]. There are several diagnosis and treatment applications nowadays that use optical methods [2-3]. These techniques work at different wavelengths within the optical spectral range [2-3]. The RI is an optical property that depends on the light wavelength and it is characteristic for individual biological materials. Moreover, the RI can be different for healthy and pathological states of the same tissues and may serve as a means for cancer diagnosis, as recently published [4]. Surprisingly, the availability of the RI of biological tissues at different wavelengths is still scarce in literature. There are some methods to measure the RI of biological tissues, but in general, this measurement is made from *ex vivo* tissue samples. One method consists in using an optical fiber where the tissue serves itself as the fiber cladding [5]. This method allows the calculation of the RI of tissues by considering the total internal reflection of light inside a quartz optical fiber. The authors of reference [5] have measured the RI of various mammalian animal and human tissues. Another method is simply designated by the total internal reflection method, which was proposed in 1996 by Li and Xie to measure the RI of biological tissues [6]. It has been widely used since then and several publications explain how this method works and present results for various wavelengths and tissues. Such method is implemented by placing the biological tissue in contact with the base of a glass prism and illuminating the set with a laser with a particular wavelength through another prism surface. By using polarized laser light as the illuminating beam of the prism/tissue setup at different angles, the amount of reflected light is measured. By knowing the RI of the prism at the laser wavelength, the RI of the tissue can be calculated by identifying the critical angle at the prism/tissue interface [1, 4, 7-10]. This method is very simple and it can be used to measure the RI of biological tissues at different wavelengths, provided that lasers at those wavelengths are available. More recently, imaging methods like confocal microscopy [11], spatial light interference microscopy (SLIM) [12] or optical coherence tomography (OCT) [13-14] have also been proposed to measure the RI of biological tissues.

With such variety of methods to measure the RI of biological tissues, it is now possible to evaluate such parameter for the various biological tissue specimens at different wavelengths. Since the RI is unique for biological tissues and can be used to discriminate between pathological and healthy tissue, we decided to study this optical property at different wavelengths for human colorectal mucosa samples. Our objective was to estimate the dispersion curves of human colorectal mucosa and discriminate between healthy and pathological tissues.

Colorectal carcinoma is the third most common cancer and the fourth cause of cancer-related mortality worldwide. Approximately 1.2 million new cases are diagnosed each year worldwide and 50% of diagnosed patients will die from the disease [15].

Current technology implies colon endoscopy [16] to establish a reliable diagnosis and colectomy constitutes the basis of surgical treatment, eventually complemented with chemotherapy and/or radiotherapy [17]. Non-invasive optical methods are desired to turn diagnosis/treatment procedures easier and less aggressive to the patient.

Colon and rectum are tube-like structures composed of several layers from the inside to the outside, as represented in figure 1:

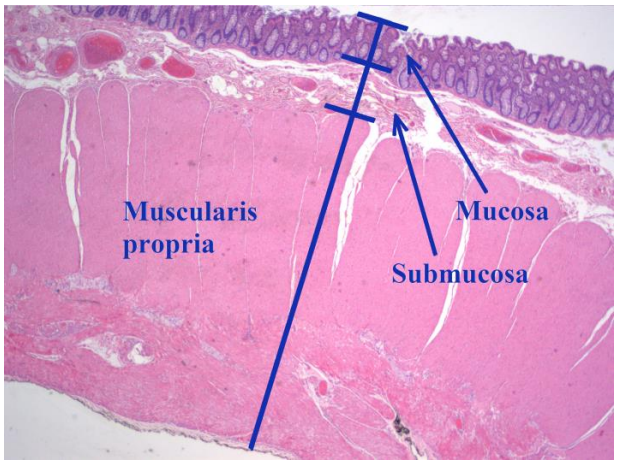

Fig. 1 Structure of the colorectal wall containing histologically distinct layers – from the inside (lumina) outwards: mucosa, submucosa and *muscularis propria*.

Adenomatous polyps, which are precursor lesions of colorectal carcinoma, originally develop in the innermost colon layer – the mucosa [18]. If polyps are not removed at this early stage, they evolve into adenocarcinoma which intrudes the other layers that compose the colorectal wall, first in the submucosa and eventually reaching the *muscularis propria*, the subserosal tissue or even the peritoneal lining or adjacent organs [19]. Since the polyps start developing in the mucosa, endoscopic instrumentation can be inserted into the colorectal lúmen to detect them [16] like the one displayed in figure 2:

Fig. 2 Colorectal polyp viewed in a surgical specimen.

The polyp in figure 2 shows a more intense red color than the surrounding tissue. Such difference in color is sugestive that it might have higher blood content than its neighbour mucosa tissues. The internal composition of colorectal mucosa and polyps is certainly different and consequently the RI for these tissues will also present different values.

Early this year, a research group has demonstrated that colorectal mucosa and dysplastic colorectal tissues present different RI values at 964 nm [4]. Since the RI is an optical property that can be measured directly, the discrimination of this parameter between healthy and pathological mucosa at different wavelengths should bring information that can be used for diagnostic and treatment purposes. Considering that optical diagnostic and treatment procedures can operate at different wavelengths, we have studied the RI of colorectal healthy and pathological mucosa samples for visible and near-infrared (NIR) wavelength ranges. This study has produced results that show similar wavelength dependencies for the RI profiles of healthy and pathological mucosa of the human colon. The correspondent dispersion curves were also estimated. The obtained RI values for pathological tissues are higher than the ones obtained for healthy mucosa and evidence of lipid content in both types of tissues was identified.

2 Materials and methods

With the objective of measuring the RI of healthy and pathological colorectal mucosa at different wavelengths, we have adopted the total internal reflection method [6]. The preparation of samples and the detailed methodology that was adopted is presented in the following subsections.

2.1 Tissue samples

Human colorectal mucosa samples were surgically collected from a population of 5 patients within a 3 month period. These patients were 3 men and 2 women with ages ranging from 52 to 82. The collected colorectal tissues had large dimensions for our research purposes and contained healthy and pathological areas that could be fragmented into smaller samples to use in our measurements.

A total of 21 healthy and 21 pathological mucosa samples were prepared to be used in our studies. Healthy and pathological samples were separated and preserved frozen at −80ºC for a period of 12 – 24 hrs prior to the beginning of measurements. A thin slice was made on the top surface of samples to turn them flat so they could be used in measurements with prism. A cryostat (Thermo Scientific™, model Microm HM 550) was used to make this slice and also to prepare thin samples with 0.4 mm thickness to use in measurements with Abbe refractometer (λ=589.6 nm). Before studies, samples were kept in saline for 10 min to mimic natural hydration.

2.2 Measurement procedure

The RI measuring setup adopted in this study was the internal reflection method with a dispersion prism as described in literature [7; 20-21]. Such experimental setup is represented in figure 3:

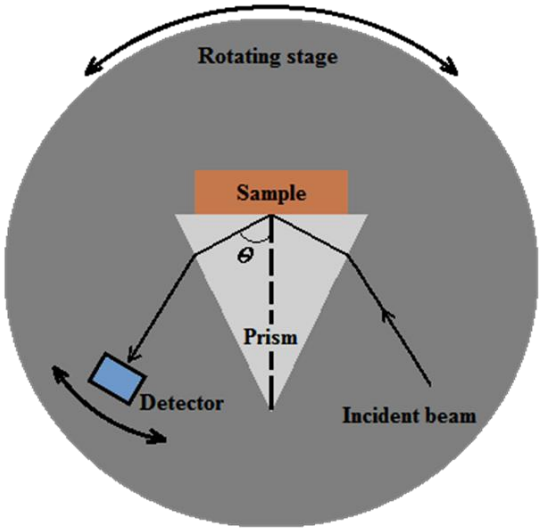

Fig. 3 Internal reflection setup.

Measurements from both types of tissue samples were made by this setup using lasers with wavelengths of 401.4, 532.5, 668.1, 782.1, 820.8 and 850.7 nm. All lasers are laser diodes from Edmund Optics, with the exception for the 668.1 nm, which is from Melles Griot. The measuring prism is a SCHOTT N-SF11 prism and it was also supplied by Edmund Optics. The RI-wavelength dependence for this prism is described by the Sellmeier equation [22], Eq. (1), and is represented in figure 4.

$$n^2 - 1 = \frac{K_1\lambda^2}{\lambda^2 - L_1} + \frac{K_2\lambda^2}{\lambda^2 - L_2} + \frac{K_3\lambda^2}{\lambda^2 - L_3}. \qquad (1)$$

According to Ref. 22, the Sellmeier coefficients in Eq. (1) take the following values for the SCHOTT N-SF11 prism: K_1=1.7376, K_2=0.3137, K_3=1.8988, L_1=0.0132, L_2=0.0623, L_3=155.2363.

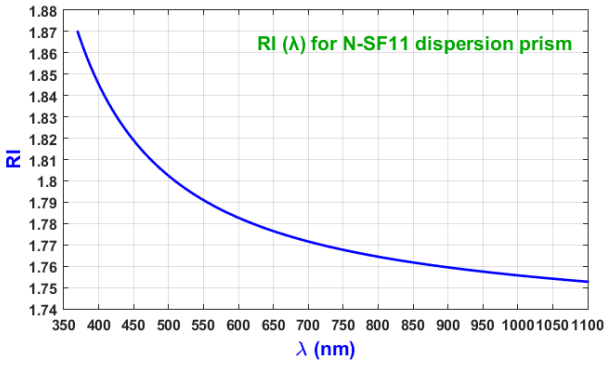

Fig. 4 RI-wavelength dependence for the N-SF11 dispersion prism.

Three sets of measurements were performed with each laser from individual healthy and other three from individual pathological samples to average results. The sequential steps in each individual study were the following:

1. The sample tissue was placed in perfect contact with the base of the prism (see figure 3);
2. An incident laser beam was used to illuminate the setup through a lateral side of the prism;
3. The reflected beam was detected by a photocell connected to a voltmeter to measure the potential difference;
4. This procedure was repeated for several angles of incidence (α) of the beam at the air/prism interface relative to interface normal;
5. Considering Snell-Descartes equation, the incidence angle at the air/prism interface (α) is related to the incidence angle at the prism/tissue interface (θ) according to:

$$\theta = \beta - arcsin\left(\frac{1}{n_1} \times sin(\alpha)\right), \quad (2)$$

where β is the prism internal angle (60º for our prism) and n_1 is the RI of the prism at the wavelength of the laser in use.

6. Reflectance at the prism/tissue interface was calculated for each angle as:

$$R(\theta) = \frac{V(\theta) - V_{noise}}{V_{laser} - V_{noise}}, \quad (3)$$

where $V(\theta)$ is the potential measured at angle θ, V_{noise} is the background potential and V_{laser} is the potential measured directly from the laser.

7. A representation of the reflectance at the prism/tissue interface ($R(\theta)$) as a function of the incident angle (θ) was created, showing an increase from a lower to a top value as a function of the incidence angle;
8. The first derivative of the previous curve was calculated, showing that a strong peak is observed at a particular incidence angle. This angle is the critical angle (θc) of reflection for a particular laser between the prism and the tissue sample;
9. Once θc was determined for a particular laser, it is used to calculate the correspondent RI of the tissue ($n_t(\lambda)$) at that particular wavelength (λ):

$$n_t(\lambda) = n_1(\lambda) \times sin(\theta_c). \quad (4)$$

In eq. (4), $n_1(\lambda)$ represents the RI of the prism at that particular wavelength. Such procedure was made using all lasers mentioned above.

In addition to these measurements, the RI of healthy and pathological mucosa were also measured with the Abbe refractometer (λ=589.6 nm). Three samples of each tissue type (healthy and pathological) were used in these measurements. Since biological tissues are in general turbid, we have prepared these samples with 0.4 mm thickness and used a He-Ne laser to improve contrast when reading the RI from the Abbe refractometer.

After obtaining the RI values of healthy and pathological mucosa for all wavelengths considered in our study, we estimated the dispersion curves for both types of colorectal mucosa tissues. Interpretation of results and discrimination between data for healthy and pathological mucosa was made.

3 Results and discussion

As described in the previous subsection, we have performed several sets of measurements from the two types of tissues. For each set of measurements made with a particular laser, the reflectance curve at the prism/tissue interface was calculated. Considering the laser with λ=850.7 nm, figure 5 presents the individual reflectance curves obtained for both types of tissues:

Similar graphs to the ones presented in figure 5 were calculated for the measurements with the other lasers. All graphs in figure 5 show that reflectance increases with the incident angle for both types of tissue, but for the case of pathological mucosa such increase is faster for angles around 50º. The following step consisted on calculating the first derivative of the reflectance curves. To perform this calculation, we have used MATLAB™. The first derivative is also a function of the incident angle and it was calculated according to equation 5:

$$deriv = \frac{Ref(\theta_i) - Ref(\theta_{i-1})}{\theta_i - \theta_{i-1}}, \quad (5)$$

where $Ref(\theta_i)$ represents the reflectance at a particular angle, θ_i, and $Ref(\theta_{i-1})$ represents the reflectance at the previous angle θ_{i-1}. The derivative calculated with Eq. (5) is the difference between consecutive reflectance values, normalized to the difference between the correspondent angles. This means that Eq. (5) calculates a local derivative. Figure 6 presents the results of these calculations for the datasets presented in figure 5.

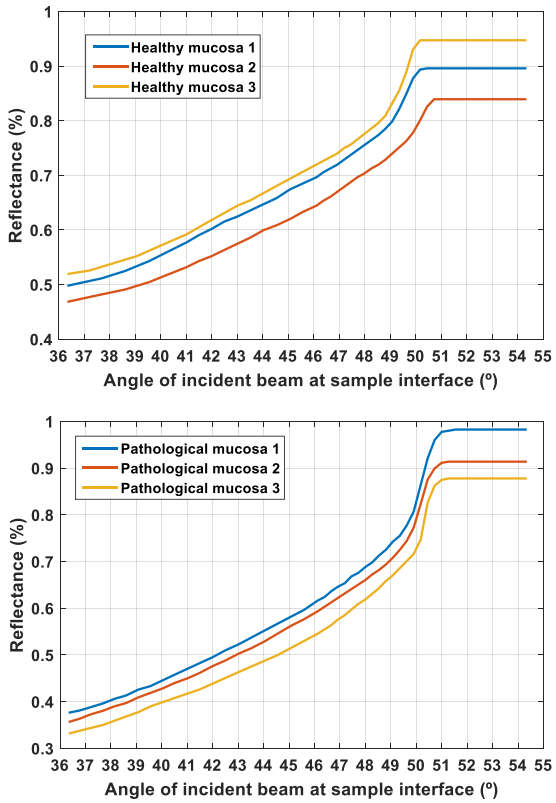

Fig. 5 Individual reflectance curves at the prism/tissue interface for the 850.7 nm laser.

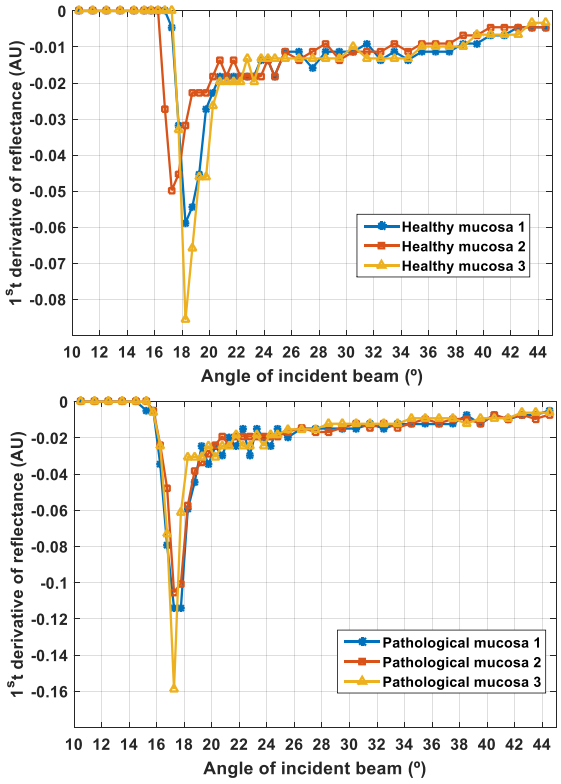

Fig. 6 1st derivative curves of the reflectance measurements made from colorectal healthy and pathological mucosa samples with the 850.7 nm laser.

The graphs in figure 6 consider the incident angle at the air/prism interface. Using MATLAB's CFTOOL, each dataset like the ones presented in figure 6 was fitted with a smooth spline curve to estimate the critical angle with precision. The critical angles of reflectance (α_c) correspond to the inverted peaks in previous graphs. A value for the critical angle α_c, was obtained for each curve that corresponds to an individual measurement. After obtaining the critical angles for each case, Eq. (2) was used to calculate the correspondent critical angles at the prism/tissue interface, θ_c. Using the individual values of θ_c in Eq. (4) we calculated the RI values for both tissue samples at the various laser wavelengths. Since we performed three studies with each laser, three RI values were obtained for each type of mucosa tissues at every particular laser wavelength. Using these RI values obtained from measurements with same laser, we calculated the mean and SD values at that particular wavelength for healthy and pathological mucosa.

Similarly, mean and SD values were also calculated for the RI of both samples at the wavelength of the Abbe refractometer. All the experimental resulting RI values are presented in table 1.

The experimental data for healthy mucosa in table 1 is presented in figure 7 along with the calculated dispersion curve indicated in literature [4].

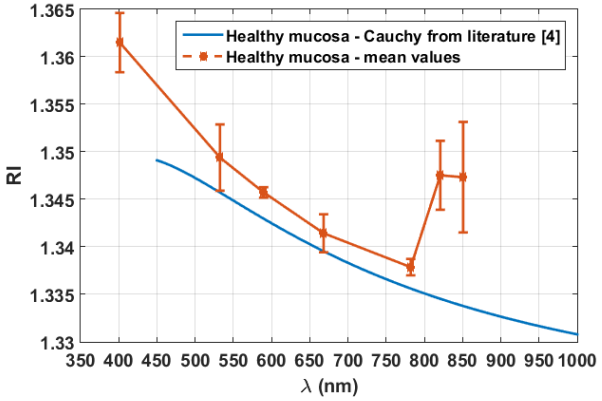

Fig. 7 RI of healthy human colorectal mucosa: experimental and literature data.

The dispersion curve presented in figure 7 was calculated using the following Cauchy equation [4]:

$$n_{mucosa}(\lambda) = 1.3217 + \frac{0.00994}{\lambda^2} - \frac{0.00089}{\lambda^4}. \qquad (6)$$

This equation was estimated based on experimental data from 450 to 1550 nm [4]. To perform calculations with Eq. (6), wavelengths must be considered in μm. As we could see from previous figure, for wavelengths between 500 and 800 nm, our experimental results are a little higher than the theoretical curve calculated by the authors of Ref. 4. Wavelength dependence for our experimental RI data is similar to the curve described by Eq. (6) for this range. When considering the uncertainty of the calculated curve, our values are consistent with estimations of the authors of Ref. 4 within the

Table 1 Measured and calculated mean RI values for healthy and pathological mucosa.

	λ (nm)						
Healthy mucosa	**401.4**	**532.5**	**589.6**	**668.1**	**782.1**	**820.8**	**850.7**
Sample 1	1.3634	1.3510	1.3457	1.3394	1.3377	1.3470	1.3433
Sample 2	1.3579	1.3518	1.3463	1.3415	1.3371	1.3514	1.3540
Sample 3	1.3632	1.3454	1.3452	1.3434	1.3388	1.3442	1.3447
Mean	1.3615	1.3494	1.3457	1.3414	1.3379	1.3475	1.3473
SD	0.0031	0.0035	0.0006	0.0020	0.0009	0.0036	0.0058
Pathological mucosa	**401.4**	**532.5**	**589.6**	**668.1**	**782.1**	**820.8**	**850.7**
Sample 1	1.3674	1.3510	1.3508	1.3475	1.3431	1.3581	1.3531
Sample 2	1.3722	1.3475	1.3496	1.3451	1.3427	1.3526	1.3537
Sample 3	1.3690	1.3431	1.3512	1.3451	1.3395	1.3530	1.3559
Mean	1.3695	1.3554	1.3505	1.3459	1.3418	1.3546	1.3542
SD	0.0024	0.0064	0.0008	0.0014	0.0020	0.0031	0.0015

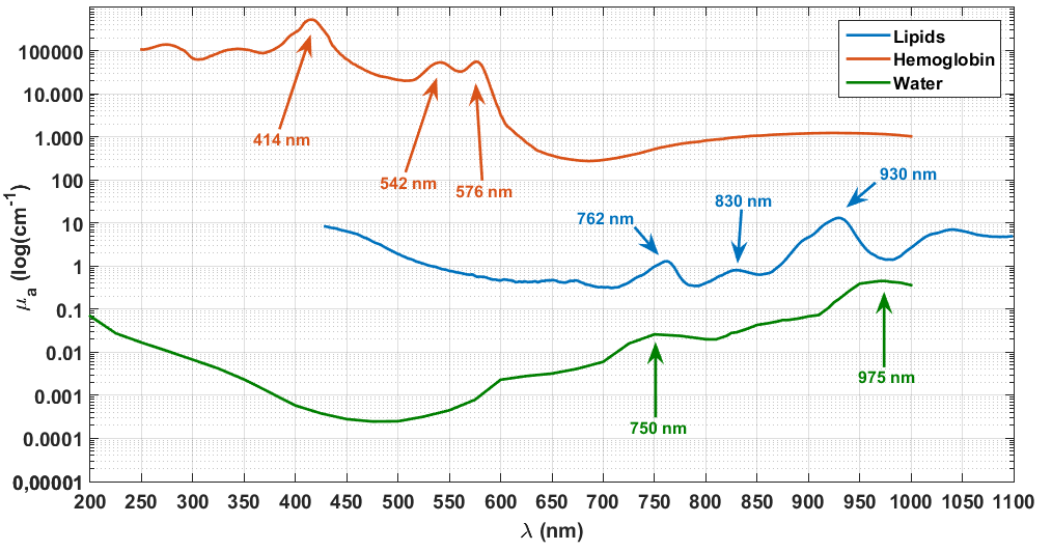

Fig. 8 Absorption coefficient spectra of water, hemoglobin and lipids.

mid-wavelength range. For shorter and longer wavelengths, our experimental results are significantly different from the dispersion curve described by Eq. (6). For ultraviolet wavelengths, our data seems to have more consistent wavelength decay as described in literature [21,23]. Such difference is visible, since we have used a laser with 401.4 nm in our measurements. For longer wavelengths, the difference between our results and the curve described by Eq. (6) is very significant and provides major information. First of all, the authors of Ref. 4 have not obtained measurements between 750 and 950 nm. For this reason, their curve (Eq. (6)), shows very smooth decay in this range. In our case, we see an increase in the RI of mucosa, meaning that some tissue component is responsible for this increase. Searching for an explanation to this anomalous behavior, we have found that lipids contain absorption bands in this spectral range. Figure 8 contains the absorption coefficient spectra for water, hemoglobin and lipids (most common tissue components), as retrieved from the website of the Oregon Medical Laser Center [24]. Figure 8 is represented in logarithmic scale to contain all data.

According to figure 8, hemoglobin presents a peak at 414 nm and two others at 542 and 576 nm [25]. For water we see a peak at 750 nm and another at 975 nm [26]. Lipids, on the other hand have three absorption peaks – one at 762 nm, another at 830 nm and another at 930 nm [27-28]. When absorption is strong, having similar values to scattering, it is expected to observe an increase in the RI of the sample. From data in figure 8, both water and lipids in our mucosa samples may contribute to the RI increase that we have observed. The water peak at 750 nm and lipids peak at 762 nm may also produce a RI increase, but we have not performed measurements within this range of wavelengths. On the other hand, we have measured at 820.8 and at 850.7 nm. At these wavelengths we can see the effect of the second absorption peak of lipids in figure 8. Due to the presence of this peak in this range, absorption and scattering might have a similar value, which originates an increase in mucosa RI.

Considering our experimental RI data for the lowest wavelengths only (below 820.8 nm), we can also estimate a fitting curve for our experimental data. According to literature, there are three equations that are commonly used to fit the RI of biological tissues – the Cauchy equation (equation 6), the Cornu equation (equation 7) and the Conrady equation (equation 8) [21, 23]:

$$n_{mucosa}(\lambda) = A + \frac{B}{\lambda^2} + \frac{C}{\lambda^4}, \tag{7}$$

$$n_{mucosa}(\lambda) = A + \frac{B}{(\lambda - C)}, \tag{8}$$

$$n_{mucosa}(\lambda) = A + \frac{B}{\lambda} + \frac{C}{\lambda^{3.5}}. \tag{9}$$

Using MATLAB's CFTOOL, we have tried to fit our RI data with these equations. Considering RI data for healthy mucosa, we have obtained best results when fitting with Cornu and Conrady equations (Eqs. (8) and (9)). The fitting with Cauchy equation was poor, giving an R-square value of 0.356. On the other hand, when using Cornu's or Conrady's equations, we have obtained R-square values of 0.999 in both fittings. Since fitting quality is the same for the two equations, we have selected Cornu's equation to fit our data. Figure 9 shows our experimental data and the calculated fitting curve:

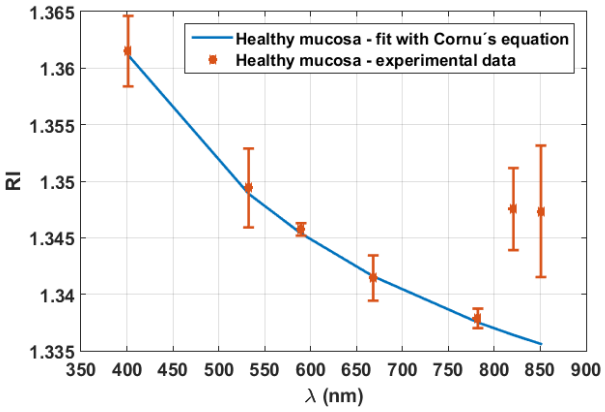

Fig. 9 Healthy mucosa – experimental data and fit curve.

As can be seen from figure 9, when calculating the fitting curve for the RI of healthy mucosa, we have neglected the experimental points at 820.8 and 850.7 nm.

The numerical parameters in the Cornu equation (Eq. (8)) that we have for this fitting are the ones in Eq. (10):

$$n_{mucosa}(\lambda) = 1.315 + \frac{16.73}{(\lambda - 38.84)}. \tag{10}$$

Performing a similar fitting to the RI data for the pathological mucosa, we have also obtained best fitting with Cornu and Conrady equations (Eqs. (7) and (8)). Once again selecting Cornu's equation, we have obtained the fitting curve represented in figure 10 and in equation 11:

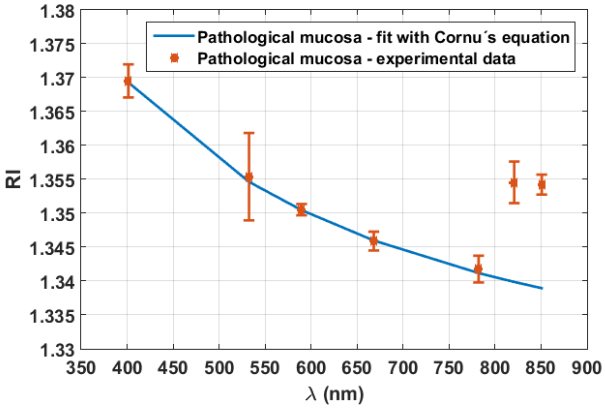

Fig. 10 Pathological mucosa – experimental data and fit curve.

$$n_{mucosa}(\lambda) = 1.315 + \frac{19.25}{(\lambda - 46.83)}. \tag{11}$$

As we have demonstrated, the best fittings for the decreasing behavior of RI with wavelength for healthy and pathological mucosa are obtained using Cornu's and Conrady's equations. Since both equations provide R-square values of 0.999, we have selected Cornu's equation to fit our experimental data.

From this analysis, we see that healthy and pathological mucosa show the same type of behavior for the RI as a function of wavelength. We have also seen that selecting the appropriate laser wavelengths it is possible to use the total internal reflection method to identify the presence of certain tissue components. In our case, by measuring at 820.8 and 850.7 nm, we could identify the presence of lipids in both types of tissues. Considering figure 8, it is possible that the other lipid peaks (762 and 930 nm) can be detected, provided that we perform measurements at those wavelengths in future. Regarding longer wavelengths and considering the data presented in Ref. 4, we assume that the decaying behavior of the RI of healthy and pathological mucosa is maintained.

4 Conclusions and future perspectives

Using the total internal reflection method, we have measured the RI values from healthy and pathological mucosa tissues at different wavelengths between the ultraviolet and near-infrared. Using the experimental data, we could estimate the dispersion curves for the

two types of tissues. Considering the visible wavelength range, our experimental data is much approximated to data presented in literature [4]. Since the lowest laser wavelength we used in our measurements was 401.4 nm, we have verified that both Cornu and Conrady equations are the best to fit the decaying RI behavior with wavelength that is described in literature for biological tissues [21, 23]. Cauchy's equation allows for good RI fittings for wavelengths above 450 nm, as demonstrated by authors of Ref.4, but as we have observed it provides poor fitting for smaller wavelengths.

We have obtained the same decaying behaviur for the RI of both colorectal tissues, but pathological mucosa presents higher RI values than healthy mucosa in the entire range of wavelengths. Such difference is significantly important for establishing diagnosis/treatment procedures that use optical technologies. By measuring at 820.8 and 850.7 nm, we were able to identify the presence of lipids in both tissues through the non-monotonic behavior observed. Lipids have strong absorption bands in this range of spectra as presented in figure 8 and the similar levels of scattering and absorption coefficients originate an increase in the RI. In the near future we intend to perform similar measurements for other wavelengths, expecting to identify other tissue components. We will also perform similar measurements for other biological tissues to obtain their dispersion curves. Such data is of high importance for the improvement and development of current and future technologies to use in clinical practice.

Another way to discriminate between healthy and pathological tissue is to estimate their optical properties. To obtain these optical properties, we need to perform inverse simulations, using the RI and other optical measurements. We plan to perform also this study in the near future for colorectal mucosa tissues.

Acknowledgments

The authors appreciate the availability of instrumental and technical resources made available by I3S-Porto and the help of Cláudia Machado in preparing the tissue samples used in these studies.

This research was supported by the Portuguese research grant FCT-UID/EQU/00305/2013.

VVT was supported by the Russian Presidential grant NSh-7898.2016.2, the Russian Governmental grant 14.Z50.31.0004, and The National Research Tomsk State University Academic D. I. Mendeleev Fund Program.

Study of immunogenic properties of transmissible gastroenteritis virus antigen conjugated to gold nanoparticles

Pavel V. Mezhenny[1*], Sergej A. Staroverov[2,3], Aleksandr S. Fomin[2,3], Aleksej A. Volkov[1], Ivan Y. Domnitsky[1], Sergej V. Kozlov[1], Vladislav N. Laskavy[3], and Lev A. Dykman[2]

[1] Saratov State Agrarian University, 1 Teatralnaya Square st., Saratov 410012, Russia

[2] IBPPM RAS, 13 Prospekt Entuziastov, Saratov 410049, Russia

[3] Saratov Scientific and Research Veterinary Institute, 6, 53rd Strelkovaya diviziya st., Saratov 410028, Russia

* **e-mail**: v1rus-m@rambler.ru

Abstract. There was performed the study of immunogenic properties of the transmissible gastroenteritis virus antigen conjugated to gold nanoparticles. In comparative immunobiological studies there was found that immunization of guinea pigs driven by the colloidal gold conjugated to transmissible gastroenteritis virus antigen of swine, leads to activation of the respiratory activity of lymphoid cells and peritoneal macrophages, which is directly related to increased activity of antibody-producing cells and activation of antibody generating. The obtained data suggest that the colloid particles promote antigen presentation to the reticuloendothelial system organs. In addition, there was established that these carriers stimulate production of proinflammatory cytokines, which leads to a complete and consistent immune response of both cellular and humoral components of immune system. © 2016 Journal of Biomedical Photonics & Engineering.

Keywords: Gold Nanoparticles, nanomaterials, transmissible gastroenteritis virus, cytokines.

Paper #3121 received 2016.12.02; accepted for publication 2016.12.29; published online 2016.12.31. doi: 10.18287/JBPE16.02.040308. [Saratov Fall Meeting 2016 Special Issue].

References

1. Q. H. Cheng, and X. Y. Niu, "Investigation on the porcine epidemic diarrhea prevalent on Qinhai," Vet. Sci. 22, 22-23 (1992).
2. B. E. Straw, S. D'Allaire, W. L. Mengeling, and D. J. Taylor (eds.) Disease of Swine, Iowa State University Press, Ames (2000).
3. B. Delmas, J. Gelfi, and H. Laude, "Antigenic structure of transmissible gastroenteritis virus. II. Domains in the peplomer glycoprotein," J. Gen. Virol. 67(7), 1405-1418 (1986).
4. L. S. Sturman, C. S. Riehard, and K. V. Holmes, "Proteolytic cleavage of the E2 glycoprotein of murine coronavirus by trypsin and separation of two different 90K cleavage fragments," J. Gen. Virol. 56(3), 904-911 (1985).
5. R. A. Moxley, and L. D. Olson, "Clinical evaluation of transmissible gastroenteritis virus vaccines and vaccination procedures for inducing lactogenic immunity in sows," Am. J. Vet. Res. 50(1), 111-118 (1989).
6. R. Mout, D. F. Moyano, S. Rana, and V. M. Rotello, "Surface functionalization of nanoparticles for nanomedicine," Chem. Soc. Rev. 41(7), 2539-2544 (2012).
7. R. Bhattacharya, and P. Mukherjee, "Biological properties of "naked" metal nanoparticles," Adv. Drug Del. Rev. 60(11), 1289-1306 (2008).
8. E. C. Dreaden, A. M. Alkilany, X. Huang, C. J. Murphy, and M. A. El-Sayed, "The golden age: gold nanoparticles for biomedicine," Chem. Soc. Rev 41(7), 2740-2779 (2012).
9. L. A. Dykman, and N. G. Khlebtsov, "Gold nanoparticles in biomedical applications: recent advances and perspectives," Chem. Soc. Rev. 41(6), 2256-2282 (2012).

10. L. A. Dykman, S. A. Staroverov, V. A. Bogatyrev, and S. Yu. Shchyogolev (eds.), Gold nanoparticles as an antigen carrier and an adjuvant, Nova Science Publishers, New York (2010).
11. S. A. Staroverov, I. V. Vidyasheva, K. P. Gabalov, O. A. Vasilenko, V. N. Laskavyi, and L. A. Dykman, "Immunostimulatory effect of gold nanoparticles conjugated with transmissible gastroenteritis virus," Bull. Exp. Biol. Med. 151(4), 436-439 (2011).
12. S. A. Staroverov, A. A. Volkov, S. V. Larionov, P. V. Mezhennyy, S. V. Kozlov, A. S. Fomin, and L. A. Dykman, "Study of transmissible gastroenteritis virus antigen-conjugated immunogenic properties of selenium nanoparticles and gold," Life Science J. 11(11), 456-460 (2014).
13. G. Frens, "Controlled nucleation for the regulation of the particle size in monodisperse gold suspensions," Nature Phys. Sci. 241(105), 20-22 (1973).
14. N. G. Khlebtsov, and L. A. Dykman, "Optical properties and biomedical applications of plasmonic nanoparticles," J. Quant. Spectrosc. Radiat. Transfer. 111(1), 1-35 (2010).

1 Introduction

For the past few years, there has been a rapid development in designing nanovaccines which are to solve relevant problems of prevention and treatment of human and animal diseases. The use of nanovaccines implies the delivery of protective antigens to immune cells with the help of nanoscale carriers. Nanoparticles produced according to the methods of chemical and biological synthesis are used in designing nanovaccines. Metal nanoparticles seem of great interest. Affecting the immune system, they mimic the properties of natural pathogens eliciting a maximum immune response and do not have side effects.

Transmissible gastroenteritis of pigs (TGE) is a highly contagious acute disease in pigs of all age groups with such symptoms as vomiting, excessive diarrhea, dehydration. It has high mortality rate, especially among piglets in their first 10 days of life. The disease greatly harms hog-raising farms [1, 2].

TGE pathogen is a RNA virus belonging to the family *Coronaviride*, genus *Alphacoronavirus*, species 1a. The virion is circular in shape with a diameter ranging from 75 to 160 nm. The nucleocapsid is a flexible spiral that contains a single strained RNA and a great number of nucleocapsid protein molecules [3, 4]. The virus replication takes place in the cytoplasm of mature epithelial cells located on the tips of villi in the small intestine.

Vaccination is the essential protection of animals against TGE. A veterinary drug market provides a high number of commercial vaccines preventing TGE. However, traditional inactivated vaccines have a range of disadvantages: they contain 99% of ballast substances which make the vaccine reactogenic; vaccines contain toxic agents used to inactivate microbial cells (phenol, formaldehyde). Also, inactivated vaccines are known to be less immunogenic because empty viral particles are unable to initiate cellular immunity. Therefore, vaccination against TGE is still considered to be a significant problem in veterinary [5].

Nowadays, there is a great number of research works dedicated to the study and use of various nanometer structures as universal carriers of biologically active substances to target cells [6, 7]. To reach the target cell *in vivo*, a nanoparticle has to overcome a lot of obstacles which are natural barriers against nonshared antigens in the animal body [8]. Gold nanoparticles as antigens and therapeutic agent carries, as well as structures synthesized on their base, are widely used in contemporary medicine and biology in immunological and therapeutic ways [9]. The ability of gold nanoparticles to provoke a humoral immune response to weak immunogenic antigens and haptens seem of great interest [10]. There are some data on immune stimulating ability of gold nanoparticles conjugated with a TGE virus [11, 12].

This research is aimed at the study of immunogenic qualities of colloidal gold (CG) nanoparticles conjugated to TGE virus antigens.

2 Materials and Research Methods

The research used the capsid protein of a TGE virus as an antigen. The protein was obtained in a virological laboratory of the Saratov veterinary research institute of Russian Academy of Sciences.

Gold nanoparticles of a circular shape with an average diameter of 15 nm were obtained according to Frens [13] method, with the use of balancing redox reaction of chloroauric acid (Sigma-Aldrich, USA) and sodium citrate (Fluka, Switzerland). The balancing was conducted when 242.5 ml of 0.01% of water solution of chloroauric acid were heated in an Erlenmeyer flask on a magnetic stirrer with a reverse water refrigerator up to 100°C. Then, 7.5 ml of 1% sodium citrate solution were added.

The diameter of the synthesized AuNPs was measured with the help of UV-Vis spectrometer Specord S 250 (AnalytikJena, Germany), the transmission electron microscope Libra 120 (CarlZeiss, Germany) and the particle size and Zeta potential analyzer ZetasizerNano-ZS (Malvern, UK); see the reference [14].

There were formed 3 groups of animals (guinea pigs), 9 heads in each, in order to do an immuno-biological research based on analogue principle. The animals were immunized subcutaneously (along the spine) twice with an interval of 10 days.

The first group of guinea pigs were injected a solution of TGE virus antigen in a dosage of 1 ml. The second group was injected a conjugated antigen of TGE

and CG in a dosage of 1 ml. The third group was injected a physiological solution in a dosage of 1 ml.

Euthanasia of guinea pigs was carried out 10 days after the last shot. Then, the serum was taken for the immunological research.

The concentration of interleukins in the serum was measured with the help of the reagent kit for the enzyme immunoassay detection of IL-1β, IL-6 and INF-γ (Vector-Best, Russia) on an immunoassay analyzer Plate Screen (Hospitex Diagnostics, Italy).

The titer of the obtained antibodies in the blood serum was measured with the help of enzyme-linked immunosorbent assay (ELISA) with the use of antibodies marked with horseradish peroxidase to IgG of guinea pigs (Jackson ImmunoResearch, UK); synthetic peptide was used as a fixed antigen. The reaction results were registered on a microplate spectrometer Plate Screen (Hospitex Diagnostics, Italy). Shortly, the antigen dissolved in a 0.01 M PBS in the ratio 1:100 was adsorbed, and then it was incubated during the night at +4°C. The unbound sites in the hole were blocked with 200 µl of 2% dried milk in a 0.01 M PBS for 1 hour in a shaker. 100 µl of animal serum dissolved in PBS 1:10 were brought in and then dissolved twice in PBS and incubated for 1 hour on a thermoshaker at 37°C; later it was washed with 200 µl of PBS three times with 10 minute intervals in a shaker. 100 µl of antigens marked with horseradish peroxidase (Jackson ImmunoResearch, UK) and dissolved in BS 1:500 were inserted into the holes and incubated for 1 hour on a thermoshaker at 37°C. Then, a triple washing was carried out with 200 µl of PBS with 10 minute intervals in a shaker. The antigen-antibody reaction was performed with the help of 100 µl of 0.006% o-Phenylenediamine (OPDA) in 0.1 M citrate buffer adding 0.01% hydrogen superoxide. The reaction was stopped with 100 µl of 0.1 M sulfuric acid.

Accommodation and care of animals as well as their euthanasia were conducted according to the guidelines of the Ministry of Healthcare of the Russian Federation for experimental biological clinics and in accordance with "European Convention for the protection of vertebrate animals used for experimental and other scientific purposes".

The obtained results were statistically processed by the standard procedures integrated in Excel 2007 software (Microsoft Corp., USA). After the arithmetic mean and the standard deviation for a given data sample had been found, we determined the standard error of the arithmetic mean and its confidence limits with account of Student's t coefficient (n, p) [number of measurements n=3, significance level=95% (p=0.05)]. These results are presented as histograms. The significance of differences between individual samples was evaluated by a two-sample unpaired Student's t test with unequal variances. Differences were considered significant when the experimentally found pexp value was ≤0.05. The reliability of the changes recorded in the results of each of the experiments described above for the entire set of antigen formulations examined was assessed by one-way analysis of variance (ANOVA) by using Fisher's ratio test. The dependences found were considered significant at $F > F_{crit}$, where the critical value F_{crit} at n=3 and m=4-5 (number of data sets) corresponded to p =0.05 (with the number of degrees of freedom (df) lying between 4 and 14) and the effective value peff was <0.05.

3 Results and Discussion

The diameter of the synthesized gold nanoparticles was measured by the methods of spectrophotometry, transmission electron microscopy (TEM) and dynamic light scattering (DLS) (see figure 1). The absorption spectrum maximum of the obtained sol was λ_{max} =529.1 nm at the optical density of A_{520} =1.2. According to TEM and DLS data, the average diameter of the obtained nanoparticles was 15.7 nm.

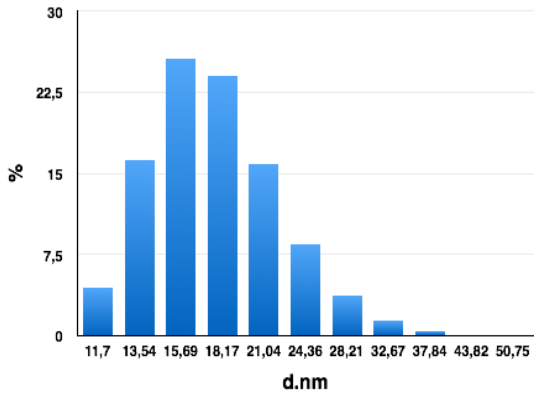

(a)

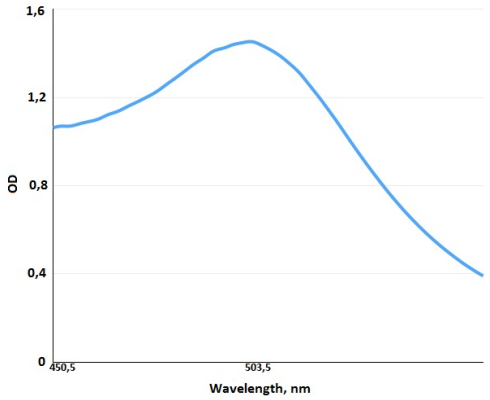

(b)

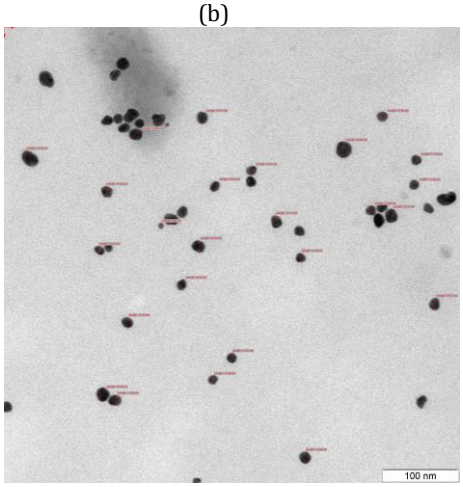

(c)

Fig. 1 The distribution of particle sizes (a), absorption spectrum (b) and TEM image (c).

Table 1 Cytokine concentration in the blood serum of the guinea pigs immunized with different drugs.

Group	Indices		
	IL-1β, pg/ml	IL-6, pg/ml	INF-γ, pg/ml
Solution of TGE virus antigen	6.93±0.91	6.68±0.46	45.06±1.69
TGE virus antigen and CG conjugate	8.10±0.74	8.59±1.01	60.44±9.91
Physiological solution	4.93±0.71	4.75 ± 0.66	34.10±6.65

Table 2 Antiviral Antibody Titre.

	TGE virus antigen	Antigen and CG conjugate
Antibody titres	1:8192	1:16384

The data show that the highest concentration of INF-γ is observed in animals immunized with the antigen conjugated to gold nanoparticles (60.44±9.91 pg/ml).

The study of interleukin-1 beta (IL-1β) concentration in the plasma of the animals demonstrates (table 1) that the highest IL-1β concentration was also observed in the group immunized with the antigen conjugated to gold nanoparticles. It was 8.10±0.74 pg/ml. The IL-1β concentration in the group immunized with the native antigen was 6.93±0.91 pg/ml.

The highest level of IL-6 was observed in the group of animals immunized with the antigen conjugated to CG. It was 8.59±1.01 pg/ml. The IL-6 concentrations in the group immunized with the native antigen and in the control group were 6.68±0.46 pg/ml and 4.93±0.71 pg/ml respectively.

Analyzing the titres of the obtained antibodies, one can notice that the antibody titre of the animals immunized with the CG conjugate is 1:16384, which is twice higher than the antibody titer of the animals in the control group (see table 2).

Thus, based on the undertaken research, it seems possible to conclude that the vaccination of animals with the TGE virus antigen conjugated with CG activates antibody production. Besides that, this carrier stimulates interferon and cytokines production what provokes a full and balanced immune response of cellular as well as humoral immunity at prophylactic immunization. The collected data allow suggesting that colloidal particles functioning as nanocarries induce the increase of antigen expression on the surface of antigen-presenting cells and likewise they favor the effective presentation of viral peptides for cytotoxic T lymphocytes and natural killer cells.

4 Acknowledgments

This study was supported by the Russian Science Foundation (grant no. 15-14-00002).

Investigation of albumin-fullerenol interaction using laser correlation spectroscopy: the algorithm

Elina Nepomnyashchaya*, Ekaterina Savchenko, Elena Velichko, and Evgenij Aksenov
Peter the Great Saint-Petersburg Polytechnic University, 29 Polytechnicheskaya st., St.Petersburg 195251, Russia

***e-mail:** elina.nep@gmail.com

Abstract. A new algorithm for the solution of the inverse problem of laser correlation spectroscopy is proposed. The algorithm allows the analysis of nanoparticle sizes in polydisperse solutions. Experimental results of the albumin-fullerenol interaction study demonstrating the efficiency of our approach are presented.

Keywords: Tikhonov regularisation, laser correlation spectroscopy, albumin, fullerenol, scattering.

Paper #3126 received 2016.11.20; accepted for publication 2016.12.29; published online 2016.12.31. doi: 10.18287/JBPE16.02.040309. [Saratov Fall Meeting 2016 Special Issue].

References

1. N. N. Pshenkina, "Serum albumin: structure and carrying function", Pharmacology 12, 1067–1091 (2011) [in Russian].
2. M. A. Orlova, T. P. Trofimova, A. P. Orlov, O. A. Shatalov, A. A. Svistunov, Yu. K. Napolov, and V. P. Chekhovin, "Fullerene derivatives as modulators for the cell proliferation and apoptosis processes", Oncohematology 4, 7–10 (2012) [in Russian].
3. L. B. Piotrovsky, M. Yu. Eropkin, E. M. Eropkina, M. A. Dumpis, and O. I. Kiselev, "Mechanisms of biologic action of fullerenes — dependence on aggregate state," Psychopharmacol. Biol. Narcol. 7(2), 1548–1554 (2007) [in Russian].
4. I. I. Grynyuk, S. V. Prylutska, N. S. Slobodyanik, O. Yu. Chunikhin, and O. P. Matyshevska, "The aggregate state of C60-fullerene in various media," Biotechnologia Acta 6(6), 71-76 (2013).
5. V. A. Shipelin, E. N. Trushina, L. I. Avren'eva, S. Kh. Soto, S. Yu. Batishcheva, G. Yu. Mal'tsev, I. V. Gmoshinski, S. A. Khotimchenko, and V. A. Tutel'yan, "Toxicological and Sanitary Characteristics of Fullerenol (Hydroxylated Fullerene C_{60}) in 28 Day In Vivo Experiment," Nanotechnologies in Russia 8(11-12), 799–809 (2013).
6. K. L. Linegar, Applications of Dynamic Light Scattering in Chemical Engineering: Polymers, Proteins, and Liquid Crystals, Thesis submitted to the Faculty of the Graduate School of the University of Maryland (2008).
7. J. Stetefeld, S. A. McKenna, and T. R. Patel, "Dynamic light scattering: a practical guide and applications in biomedical sciences," Biophys Rev. 8(4), 409–427 (2016).
8. R. Finsy, P. Groen, L. Deriemaeker, E. Geladé, and J. Joosten, "Data analysis of multiangle photon correlation measurements without and with prior knowledge," Part. Part. Syst. Charact. 9(1-4), 237–251 (1992).
9. R. Finsy, P. Groen, L. Deriemaeker, and M. van Laethem, "Singular value analysis and reconstruction of photon correlation data equidistant in time", J. Chem. Phys. 91(12), 7374–7383 (1989).
10. R. Finsy, N. Jaeger, R. Sneyers, and E. Gelade, "Particle sizing by photon correlation spectroscopy. part III: Mono and bimodal distributions and data analysis," Syst. Charact. 9(1-4), 125–137 (1992).
11. M. Shuai, J. Shen, J. C. Thomas, X. Zhu, W. Liu, and X. Sun, "Improved inversion procedure for particle size distribution determination by photon correlation spectroscopy," J. Appl. Opt. 51(25), 6220–6 (2012).
12. E. K. Nepomniashchaia, E. N. Velichko, and E. T. Aksenov, "Solution of Inverse Problem of Laser Correlation Spectroscopy by Regularization Method," Humanities & Science University Journal 13, 13–23 (2015).

1 Introduction

Albumin is the main blood protein, responsible for the transport of organic and inorganic substances (ligands), biologically active agents, fatty acids, ions, as well as medicinal preparations and their metabolites [1].

The binding function of serum albumin is caused by the structural features of this protein, the presence of active polar and hydrophobic areas on its surface. The albumin molecule, being not large in size, has two binding centres that determine the variety of its binding capacities. Under different environment conditions the protein can change its structure and lose the capability of binding with other molecules. For example, under strong variation of the solution pH or temperature the protein denaturation occurs, i.e., the globule unfolding and the transition from the tertiary structure to the primary one.

In relation with the active investigation of the protein transport function, the search is carried out for possible test molecules, the probes for activating this function. The probes are sensitive indicators of conformation transitions and other restructuring in the protein molecule. The methods using test probes are based on recording the variations of physical and chemical parameters, reflecting the process of interaction of the specific or test ligand with albumin. It is assumed that the fullerenol nanoparticles can be used for this purpose.

Fullerenol is one of the carbon modifications. It is a firm, hydrophilic, supramolecular complex, consisting of a fullerene molecule (in our case C_{60}), and the hydrate shell, enclosing the molecule [2]. Tis fullerene compound $C_{60}(OH)_{24}$ is well solvable in water, which makes it possible to use it in the study of protein solutions [3]. In the aqueous phase the fullerenol can be presented not only by free molecules, but also by multimolecular clusters, comprising 10--50 molecules, which can affect its biochemical properties.

To date the fullerenol is a promising object for nanobiotechnologies [4], particularly in the investigation of the albumin properties directly in the organism. However, the effect of fullerenols introduced into the organism on the human health is insufficiently studied, and further research is necessary to quantify these effects for complete risk estimation [5]. The characterisation of fullerenol toxic properties is of great importance, since it is expected to be used not only in laboratory diagnostics, but also in medicine, e.g., for efficient delivery of drugs, as nutrition and cosmetic supplements [5].

Thus, the study of albumin-fullerenol binding has two-fold purpose: the determination of albumin capacity of binding and transporting the substances under different conditions of environment, and the determination of the toxicity of the fullerenol itself for humans. In our paper, the solutions of albumin with fullerenol were studied by means of laser correlation spectroscopy. The developed algorithm of the experimental data analysis, based on the Tikhonov regularisation method, provides the required high accuracy of the results.

2 Experimental setup

The method of laser correlation spectroscopy is based on recording and analysing the light field scattered by the particles performing Brownian motion in a solution. The schematic diagram of measurements is presented in Fig. 1. As a source of radiation, we used the single-mode laser module with the power of continuous-wave radiation to 2.5 mW in the spectral range near 650 nm. The parasitic aureole was eliminated using the screen with a hole. The radiation is focused by the aspheric short-focus lens built in the module that allows the diameter of the beam to be 50 μm in the focus of the lens. The calculated caustic length in the solution amounts to 5 mm. The power supply of the radiation source was organised from storage cell, which provides the stability of power. The radiation scattered at the angle of 90° is detected using the photomultiplier. The diaphragm and the aperture of the single-mode optical fibre determine the angle of view for the scattered radiation detection. The length of the scattering volume, calculated for the scattering angle 90°, amounts to 4.8 mm. The signal for the photomultiplier is digitised by the ADC board at the frequency 50 MHz and was processed with a computer.

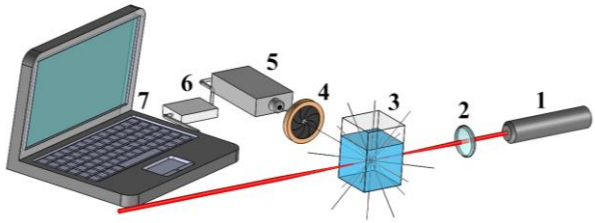

Fig. 1 Schematic diagram of laser correlation spectrometer. 1 – laser, 2 – lens, 3 – cuvette with the studied solution, 4 – diaphragm, 5 – photomultiplier, 6 – ADC, 7 – computer.

The recorded signal is a pseudorandom time dependence of the scattered radiation intensity. The spectrum of this signal is determined by the coefficients of diffusion of particles in the solution. To find the characteristic frequencies one can use the Fourier transform. However, due to the huge number of scatterers and random components in the signal, it is rather hard to select the characteristic frequencies from the spectrum. To reveal the regularities in the signal, the time-domain representation of the signal spectrum is used rather than the frequency-domain one, i.e., the correlation function of the signal is calculated.

3 Mathematical processing

According to the dynamic light scattering theory, the autocorrelation function can be described by the following expression [6]:

$$\left|g^{(1)}(\tau)\right| = \int_0^\infty F(\Gamma)e^{-\Gamma\tau}\,d\Gamma, \quad (1)$$

where Γ is the diffuse spectrum broadening, F(Γ) is the contribution from the particles of one size into the total intensity of scattering. The diffuse broadening is related to the diffusion coefficient D as:

$$\Gamma = Dq^2, \quad (2)$$

where $q = (4\pi n/\lambda)\sin(\theta/2)$ is the scattering vector, n is the refractive index of the medium, λ s the wavelength, θ is the scattering detection angle.

Making use of the Stokes-Einstein formula

$$D = k_b T/6\pi\eta R \quad (3)$$

(η is the medium viscosity, k_b is the Boltzmann constant, T is the temperature, R is the radius), it is possible to calculate the hydrodynamic radius of the studies particles.

Thus, the solution of Eq. (1) is the main problem in the mathematical processing of the light scattering signal. This equation is an integral Fredholm equation of the first kind, and due to the presence of random noise in the experimental data, its solution belongs to the class of ill-posed problems. This means that the presence of even small error in the initial data will cause the accumulation of error in the process of common solution, and the result may strongly differ from the real one.

To date a variety of methods for solving the equations like Eq. (1) exists. Up to now, the most widespread in the commercial production is the method of cumulants. This method is rather simple in implementation, fast and convenient in application, thanks to which it is included into the International Standard ISO 13321. However, in the absence of a priori information this method allows the determination only of some mean values of the diffusion coefficients and their moments. Moreover, the method of cumulants provides reliable particle size only for monomodal distributions and for polydisperse solutions often yields wrong results [DLS: practical guide 2016]. In our case, the polydispersity of the mixture plays a crucial role in the study of the albumin binding properties, which makes it impossible to use simple monomodal methods.

To solve the inverse problem in the case of polydisperse solutions it is possible to use the methods of nonlinear optimisation (the Levenberg-Marquardt method). Unfortunately, they require rather exact a priori information about the shape and the number of components in the distribution, and, therefore, are not always convenient in the processing of real signals.

The methods that do not require the knowledge of the distribution shape (with reasonable physical requirement of non-negativity of results) include the NNLS (Non-Negative Least) method and its different modifications based on regularisation, e.g., CONTIN (Constrained Regularization Method for Inverting Data) [DLS: practical guide 2016], as well as the SVR (Singular Value Analysis and Reconstruction) method and MEM (Maximum Entropy Method). In a number of papers, the results of applying the above methods to different polydisperse and monodisperse systems are compared [8 – 10]. As a rule, SVR yields higher precision of results than the other above methods do. However, the existing requirement of equidistant time intervals [10] between the points in the solution does not allow the study of solutions with large and small particles present simultaneously with similar accuracy.

The methods of regularisation and the entropy maximum allow the results close in accuracy, the regularisation methods operating almost twice as fast as the entropy maximum method [9]. At the same time, none of these methods yields "non-blurred" distributions in the case when many closely spaces peaks are present in the solution.

In this connection, the necessity appeared to develop an original algorithm for processing the data of laser correlation spectroscopy. As a base, we took the regularisation methods that possess greater stability against the errors and potentially can provide more information than the entropy maximum method [9].

Among the variety of regularisation methods, the CONTIN method was most popular until recent time. Unfortunately, it is very exacting with respect to the choice of regularisation parameter and, as already mentioned above, does not allow the resolution of narrow peaks. In this connection, we decided to use a more advanced modification, the Tikhonov regularisation, which was rarely used before because of complexity of algorithmisation. In recent years different modifications of Tikhonov regularisation were described in scientific literature, however, when the number of components in the signal is large, the accuracy of the solutions is low [11]. In spite of this fact, the potentialities of the method are undoubtful.

The numerical solution of Eq. (1) is presented as a set of N points. Thus, we arrive a system of N equations, which in the matrix form can be written as

$$A\boldsymbol{f} = \tilde{\boldsymbol{g}}, \quad (4)$$

where $A_{ij} = e^{-\Gamma_j\tau_i}$, $\boldsymbol{f} = F(\Gamma_j)$, $\tilde{\boldsymbol{g}} = g^{(1)}(\tau)$.

When using the regularisation, certain a priori conditions are imposed on the solution of this system of equations, depending on the problem under solution. The commonly accepted conditions are that the solutions should be non-negative (bounded within the compact set $M \geq 0$), as well as the condition of smoothness, i.e., the absence of spikes.

To find the approximate solution of the system of equations (4) stable with respect to small variations of the right-hand side, in the Tikhonov methods the system of linear algebraic equations (SLAE) (4) is replaced with the minimisation problem with the addition of regularising term:

$$||A\boldsymbol{f} - \tilde{\boldsymbol{g}}||^2 + \alpha\Omega(\boldsymbol{f}) \to min, \quad (5)$$

where $\alpha > 0$ is the smoothing parameter, $\Omega(\boldsymbol{f})$ is the stabilising functional, individually chosen for each problem. In order to get smooth solutions in laser correlation spectroscopy, the stabilising functional is chosen to reduce the jumps of zero derivative, i.e., $\Omega(\boldsymbol{f}) = ||\boldsymbol{f}||^2$. This is because the size distribution of particles as a rule is Gaussian. Such minimisation stabilises the solution of the system, improving its conditionality and increasing the consistency of real and desired solution.

The regularisation parameter α is chosen basing on the input data: too large α leads to the appearance of extra-smoothed solutions, while too small α makes the problem unstable. In our algorithm the parameter α was chosen to be 1% of the maximal diagonal element of the matrix A. After the first solution of the system (5) the discrepancy $||A\boldsymbol{f} - \tilde{\boldsymbol{g}}||^2$ was calculated, the parameter α was reduced by 90% and the system was solved again. After the second iteration, the discrepancy was calculated again and compared with that obtained at the previous iteration. If the difference was greater than 10%, the parameter α was again reduced by 90%, and the next iteration was performed. In the proposed algorithm due to the comparison of discrepancies, it is not necessary to specify the noise level in the experiment, which is often not exactly known.

The system of equations (5) is solved using the upgraded Gauss method, in which the eigenvalues of the matrix are shifted towards greater values at the expense of introducing the regularising term, which makes the solution more stable with respect to noises, inevitably present in real experiments.

After completing the solution cycle and getting the final distribution $\boldsymbol{f}$, the check for negative solution components is performed. The programme implies the possibility of using two different methods of excluding the negative solutions. In the first method if $f_j < 0$ we set $f_j = 0$ for all extreme values j in the present Gaussian and exclude these points from further calculations. Then we return to the specification of the initial values of α. In the second method f_j with the values > 60% of the minimal value are excluded from the calculations, rather than the extreme points. This calculation operates faster, but yields less precise results, therefore, it is more suitable for preliminary analysis of the size distribution of particles. The recalculation of (5) is continued until the elimination of all negative components.

Setting rather large α could lead to smoothing and broadening of narrow distributions. However, besides the elimination of negative values, the process of excluding positive values is introduced into the algorithm. One at a time, the extreme points are excluded from the Gaussian until the given width is achieved, which allows the calculation of sizes in strongly polydisperse mixtures with the error ±0.5 nm, P = 95%.

Finally, the used algorithm can be formalised as follows:

1. setting the initial (large enough) value of α;
2. solution of the system of equations (5) and calculation of the solution $\boldsymbol{f}$;
3. calculation of discrepancy $||A\boldsymbol{f} - \tilde{\boldsymbol{g}}||^2$ (after the first iteration reducing α by 90% and return to 1);
4. comparison: $||A\boldsymbol{f} - \tilde{\boldsymbol{g}}||_i^2 < 0{,}1 \cdot ||A\boldsymbol{f} - \tilde{\boldsymbol{g}}||_{i-1}^2$, if yes, then reduce α by 90% and go to 1, if not, then go to 5;
5. check for the presence of negative components in the solution $\boldsymbol{f}$: if $f_i < 0$ then set $f_j = 0$ and return to 1. The corresponding component is excluded from further calculations;
6. if there are no components $f_i < 0$, then check the number of distribution points n > N (specified before starting the algorithm), if yes, then set $f_{min} = 0$ and return to 1, if no, then the end of calculation.

Before one begins the calculation, in order to accelerate the process one has to specify the domain of the expected solutions and the desirable accuracy. The search in the entire domain of admissible solutions is also possible, but requires much more time because of the cubic dependence of the time consumption upon the number of points in the Gaussian method. It is also necessary to specify the method of excluding negative solution components, as described above, and the number of points left in the peak (more points are taken in the presence of weak components). For better accuracy, the possibility is provided to perform the averaging of correlation, obtained from the experimental data.

The precision of experimental data processing was checked in model solutions, the mixtures of microspheres having different diameters. The results have shown that for single-component solutions the proposed algorithm does not yield in precision to the known commercial analogues with built-in processing (the spectrometers Zetasizer Nano ZS and Photocor) [12]. However, for three and more different sizes of particles the precision of the developed algorithm is by 30-60% higher. Thus, the programme of processing the results of laser correlation spectroscopy based on Tikhonov regularisation, described in the present paper, allows the study of polydisperse biological solutions.

4 Results

In the first series of experiments, we performed control measurements of the albumin molecule size in water and saline. The albumin concentration in the initial sample amounts to 100 g/l, which is close to physiological concentrations of this protein in the human blood plasma.

Under different diseases, the pH of the organism cam change both to the acidic and the alkalotic side. Therefore, we performed the study of the dependence of the protein hydrodynamic radius on the pH of the solution. The results are presented in Fig. 2. It is seen that at pH = 4.5 - 5 (the albumin isoelectric point) the hydrodynamic radius of the molecule is maximal, i.e., its spatial structure changes. The albumin molecule actively reacts to the smallest changes of the environment, including the pH variation. In particular, it can shrink, stretch, untwist, twist its spirals, or prepare the sites for a contact with ligands.

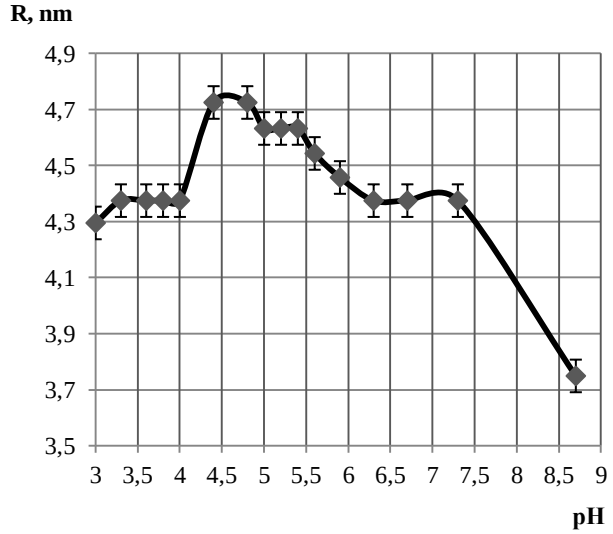

Fig. 2 Dependence of the size of a single albumin molecule on the pH of the solution.

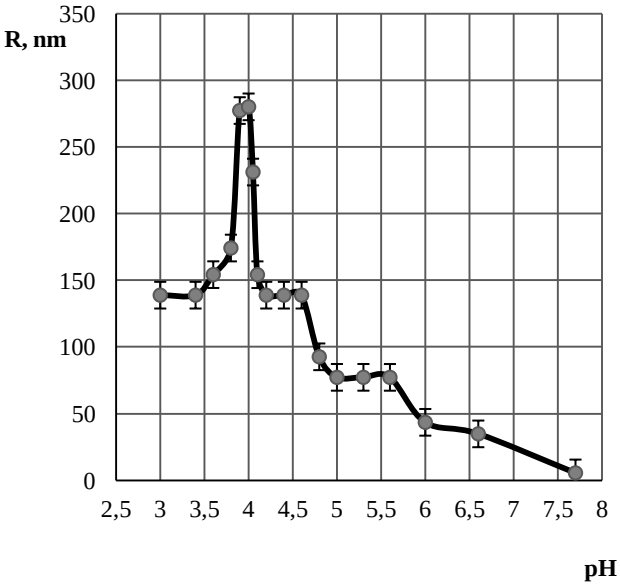

Fig. 3 Conglomerate radius versus pH for the binding of fullerenol and albumin.

In the second series of experiments, we studied the binding capacity of albumin with fullerenol under the variation of the solution pH. It was found that the optimal concentration ratio for binding two molecules is albumin : fullerenol=1:3. With growing acidity of the solution, the characteristic dimensions of the formed clusters increased. The obtained dependence of the albumin+fullerenol hydrodynamic radius on the solution pH is presented in Fig. 3.

From the plot it is seen that the maximal size of conglomerates is observed at pH = 4, which differs from the albumin isoelectric point. In the course of binding fullerenol, bilirubin, fatty acids, etc., the globule structure can change. In this case the conformation restructuring is possible both in the entire molecule and in the binding site at other pH values, too. As a result, the number of binding centres can change, and the binding of different number of molecules is possible. Hence, the obtained results may evidence in favour of both the swelling of the protein molecule itself at pH = 4, and the strong interaction with the fullerenol particles. Moreover, the fullerenol itself can lose stability in acidic solutions and form both own aggregates and the multilayer structures on the albumin surface.

Under the change of pH towards strong acidity (< 3 pH), the cluster size is decreased, which is due to the albumin denaturation. In this case, almost no aggregation is observed due to the global restructuring of the molecule and the reduction of the number of binding centres and their activity.

At pH = 7.5 the albumin molecule has its characteristic size R = 6 nm and binds the individual fullerenol particles with R = 2 nm without the formation of double layers, which is confirmed by the observation that the maximal size of the particles, found in the solution, amounted to 8 – 10 nm.

5 Conclusions

We proposed and implemented as a programme the algorithm for processing the information signals, obtained suing the method of laser correlation spectroscopy, based on Tikhonov regularisation. The algorithm allows the study of polydisperse solutions with high accuracy. The result of experimental approbation confirmed the expected accuracy of the calculations using the proposed algorithm in the analysis of biomolecular polydisperse solutions. By the example of albumin interacting with fullerenol, the specific features of the interaction of two molecular solutions under the action of different factors were shown. The experimental results have demonstrated that under normal conditions (physiological temperature and acidity of solutions) the interaction of albumin with fullerenol leads to the formation of bonds between the individual fullerenol molecules and albumin. The minor change of pH towards the greater acidity causes strong clustering of molecules. It is possible to suggest that the albumin becomes surrounded by the fullerenol particles and loses the binding capacity to other substances. Besides, a trend to the change of conglomerate sizes under the pH variation is observed, which allows

conclusions about the restructuring of albumin and the formation of multiple binding centres. Thus, fullerenol can be used as a probing substance for the analysis of structural changes in proteins. The observed effects require further studies aimed at specifying the mechanisms of interaction between albumin and fullerenol and assessing the possibility of using fullerenol as transport agent.

Photosensitizing properties of supramolecular systems based on chlorin e_6

Inna V. Klimenko[1*], and Anton V. Lobanov[2]

[1] Emanuel Institute of Biochemical Physics of Russian Academy of Sciences, 4 Kosygin str., Moscow 119334, Russia

[2] Semenov Institute of Chemical Physics of Russian Academy of Sciences, 4 Kosygin str., Moscow 119334, Russia

*** e-mail:** inna@deom.chph.ras.ru

Abstract. The novel supramolecular systems based on chlorine e_6 (Ce_6) are presented, and their optical absorption and fluorescence have been investigated. The influence of different excipients as poly-N-vinylpyrrolidone (PVP), polyethyleneglycol (PEG), bovine serum albumin (BSA), chitosan, Triton X-100 (TX-100) on spectral characteristics of these systems has been studied. The obtained spectral-fluorescence characteristics of Ce_6-PVP, Ce_6-PEG, Ce_6-BSA, Ce_6-TX-100 indicate disaggregation of chlorine e_6 molecules and their consecutive interaction with excipients in solutions and formation of molecular associates and molecular complexes. The system Ce_6-chitosan is characterized by aggregation of pigments in solution that reduces photochemical activity of a photosensitizer. The fluorescence quantum yield φ_k of mentioned above supramolecular systems has been calculated. The results can be useful during the new method of controlled aggregation of photosensitizers as a part of supramolecular complexes development as well as for the purposes of new medicines of predictable photodynamic activity creation.

Keywords: chlorin e_6, photodynamic therapy, supramolecular systems, spectral characteristics, optical absorption, fluorescence

Paper #3122 received 2016.11.20; accepted for publication 2016.12.29; published online 2016.12.31. doi: 10.18287/JBPE16.02.040310. [Saratov Fall Meeting 2016 Special Issue].

References

1. A. B. Uzdensky, Cellular and molecular mechanisms of photodynamic therapy, Science, SPb, Russia (2010).
2. A. L. Akopov, N. V. Kazakov, A. A. Rusanov, and A. Karlson, "The mechanisms of photodynamic action for treating of cancer patients," Photodynamic therapy and photodiagnostics 4(2), 9-16 (2015) [in Russian].
3. E. V. Pinyaskina, "Photodynamic processes in cells. Primary mechanisms," Bulletin of DSPU 1, 60-67 (2010) [in Russian].
4. E. Zenkevich, E. Sagun, V. Knyukshto, A. Shulga, A. Mironov, O. Efremova, R. Bonnett, S. P. Songca, and M. Kassem, "Photophysical and photochemical properties of potential porphyrin and chlorin photosensitizers for PDT," J. of Photochemistry and Photobiology B: Biology 33(2) 171-180 (1996).
5. M. V. Parkhats, V. A. Galievsky, A. S. Stashevsky, T. V. Trukhacheva, and B. M. Dzhagarov, "Dynamics and efficiency of the photosensitized singlet oxygen formation by chlorin e6: the effects of the solution pH and polyvinylpyrrolidone," Optics and Spectroscopy 107(6), 974–980 (2009).
6. C. T. H. Yen, G. V. Ramenskaya, and N. A. Oborotova, "Chlorin derivatives in cancer photodynamic therapy," Rus. J. of Biotherapy 8(4), 99-104 (2009) [in Russian].
7. M. V. Parkhats, V. N. Knyukshto, H. A. Isakau, P. T. Petrov, and B. M. Dzhagarov, "Photophysical properties of photosensitizer chlorin e6 incorporated into polyvinylpyrrolidone," Proc. SPIE 6727, 67272L (2007).
8. T. E. Zorina, I. V. Yankovsky, I. E. Kravchenko, T. V. Shman, M. V. Belevtsev, and V. P. Zorin, "Evaluation of Phototoxicity and cytotoxicity for chlorin e6 ester derivatives and their liposomal forms," Biophysics 60(5), 759-766 (2015).
9. E. A. Genina, Biophotonics methods: Phototherapy, New Wind, Saratov, Russia (2012).

10. H. A. Isakau, M. V. Parkhats, V. N. Knyukshto, B. M. Dzhagarov, E. P. Petrov, and P. T. Petrov, "Toward understanding the high PDT efficacy of chlorin e6–polyvinylpyrrolidone formulations: Photophysical and molecular aspects of photosensitizer–polymer interaction in vitro," J. of Photochem. and Photobiol. B: Biology 92(3), 165-174 (2008).
11. A. K. Visheratina, A. O. Orlova, V. G. Maslov, A. V. Fedorov, and A. V. Baranov, "Optical properties of conjugates of CdSe/ZnS quantum dots and chlorin e6 in aqueous solution," J. of Opt. Tech. 82(11), 738-742 (2015).
12. S. L. Fiedaruk, T. V. Trukhacheva, S. N. Sokolov, K. A. Frolenko, and V. P. Kheidorov, "The study of spectral properties of dimethylester of chlorin e6 in the presence of polyvinilpyrrolidone," Vestnik farmacii 3(65), 82-88 (2014) [in Russian].
13. V. Yu. Plavskii, V. A. Mostovnikov, G. R. Mostovnikova, A. I. Tret'yakova, and A. V. Mikulich, "Spectral-luminescent properties of chlorin e6 and malate dehydrogenase complexes," J. of Appl. Spectroscopy 71(6), 818-828 (2004).
14. G. P. Gurinovich, A. I. Sevchenko, and K. N. Solov'ev, Spectroscopy of a chlorophyll and related compounds, Science and technology, Minsk, USSR (1978).
15. H. Podbielska, A. Ulatowska-Jarza, G. Muller, I. Holowacz, J. Bauer, and U. Bindig, "Silica sol-gel matrix doped with Photolon molecules for sensing and medical therapy purposes," Biomolecular Engineering 24(5), 425-433 (2007).
16. A. A. Krasnovsky, "Photodynamic action and singlet oxygen," Biophysics 49(2), 289-306 (2004) [in Russian].
17. G. V. Golovina, V. A. Ol'shevskaya, V. V. Vargin, V. A. Kuzmin, and A. B. Shevelev, "Solubility of porphyrine derivatives in vivo affected by aggregate formation and complexes formation with serum albumin," Health of the population and habitat 12, 41-43 (2013) [in Russian].
18. N. H. Karapetyan, and V. N. Madakyan, "The Interaction of new pyridylporphyrins with bovine serum albumin," Russ. J. of Boiorganic Chemistry 30(2), 172-177 (2004) [in Russian].

1 Introduction

Photodynamic therapy (PDT) is clinically used as a nonsurgical treatment in oncology, ophthalmology, dermatovenerology, and others, for various diseases, for example, cancers and bacterial cells. It is based on the use of a special chemical agent – photosensitizer (PS), which is accumulated in pathological target cells and initiated by laser light of an appropriate wavelength, corresponding photosensitizer absorption maxima. As a result, photochemical reactions between PS and oxygen, leading to the formation of cytotoxic agents in tumor tissue, damaging a tumor, take place. At this, photosensitizer transits into exited state, and PS molecule undergoes or oxidation-reduction reactions with electrons or protons transfer and formation of intermediate products - the radicals, further interacting with oxygen, or transfers excess of energy to the molecule of oxygen transiting at the same time into the excited singlet state [1].

In real biological systems both mechanisms can take place. Their relative contribution to bioprocesses depends on the PS identity, a concentration and a nature of the oxidized reagents, a concentration of oxygen and some other factors.

Nowadays most of the clinically used and experimentally tested PSs belong to the class of porphyrines or their reduced analogues, chlorins [2]. In biosystems in the presence of oxygen they usually enter photochemical reactions of the II type as the first triplet state energy of porphyrines (200 kJ/mol) is sufficient for $^1O_2$ (95 kJ/mol) development [3].

Chlorin e_6 (Ce_6) belongs to the class of the plant porphyrines purchasing from chlorophyll a. It is anticancer immune response modifier, activating the system of cell-mediated immunity and it possesses the following spectral and energy characteristics: the maximum of absorption is in the region of 660±5 nm that corresponds to the region of the greatest optical transparency for biological tissue, and a quantum yield of singlet oxygen reaches 0.7 [4, 5]. Three COOH groups provide the Ce_6 molecule hydrophilic properties, effective transport and accumulation in tumour tissue. High photodynamic activity when using small doses and low toxicity are also characteristics of Ce_6. Moreover, the availability of raw materials (microalgae *Spirulina platensis* or leaves of a nettle) plays a large role in the development of compounds based on chlorin.

Such "second-generation" photosensitizers as Radachlorine, Photolon, Potoditazin and others of chlorin alignment are in medical application in Russia. Various physical, chemical and pharmacological properties, and also various commercial costs are the characteristic of all these medicines [6]. However, these PSs have the high degree of phototoxicity connected with a high quantum yield of the singlet oxygen which is formed under the light influence when carrying out PDT. Besides, Ce_6, as a substance, has a number of shortcomings limiting its broad consumption, for example, a small period of storage and a loss of optical properties, elimination within 48 hours or more. It should be noted that chlorin molecules also tend to form aggregates in water solutions that leads to considerable decrease in photodynamic activity [5, 7]. Besides, the aggregation processes of the porphyrine pigments take place in polar solvents because of hydrophobic and π-π interactions of tetrapyrrol structures [8]. To avoid these

it's reasonable to develop and study the new effective systems with the optimum photophysical and pharmacological properties.

In this work the novel supramolecular systems based on chlorin e_6 have been obtained and the influence of various excipients on spectral characteristic of these systems as well as the influence of intermolecular interactions on aggregation behavior of chlorin e_6 in solutions have been studied.

2 Materials and methods

Ce_6 (Fig. 1) was kindly provided by the colleagues from Moscow Technological University (Preobrazhensky Department of chemistry and technology of biologically active compounds). Basic Ce_6 solutions with the concentration of $2.0 \cdot 10^{-3}$ mol/l were prepared by dissolution of Ce_6 dry sample weight in 20 ml of dimethylformamide (DMF) double-distilled. The received concentration was specified on electron absorption spectrum. Solutions stored in the dark at +4 ^{0}C. Purity and identity of Ce_6 were confirmed with the MALDI - mass spectrometry method on the Thermo Scientific DSQ II single quadrupole mass spectrometer (Thermo Scientific, USA)

The choice of water-soluble polymers (Fig. 1) is explained by the fact that they are the most widespread biologically-compatible substances which are the part of physiological solutions applied as a part of pharmacological drug. Supramolecular systems based on Ce_6 ($2 \cdot 10^{-5}$ M) in various excipients were studied: poly-N-vinylpyrrolidone (PVP) - Ce_6, polyethyleneglycol (PEG) - Ce_6, Triton X-100 (TX-100) - Ce_6 , bovine serum albumin (BSA) - Ce_6, chitosan - Ce_6. Water solutions of Triton X-100 micelles (TX-100, $C_{34}H_{62}O_{11}$, LAB-SCAN analytical sciences, Poland) of concentration $2.5 \cdot 10^{-4}$ mol/l, and 2% (weight) solutions of poly-N-vinylpyrrolidone (PVP, (M=26500), Sigma-Aldrich, Germany) and polyethyleneglycol (PEG, (M=1000) MERCK, Germany) were prepared separately.

Absorption spectra (200-900 nm) were recorded with TU-1901 UV-Vis spectrophotometer from Beijing Purkinje General Instruments Co Ltd. Poorly resolved spectra were analyzed by decomposing the spectra into their Gaussian constituents.

The fluorescence spectra in the range of 550-800 nm were recorded with Fluorat-02-Panorama spectrofluorimeter (Lumex, Russia). The excitation wavelength was 410 nm. All measurements were conducted at 20 °C in standard K10 quartz cuvettes with optical path lengths of 1 cm. Registration of singlet oxygen was carried out by the method of "chemical traps"; 1,3-diphenylisobenzofuran was used as a "trap".

3 Results and discussion

Obtained in this experiment optical absorption spectrum of Ce_6 aqueous solution practically corresponds to the data of Ce_6 optical absorption spectrum presented in [9-13]. It is characterized by a strong Soret band with a peak at λ=403 nm, typical for all porphyrines [14] and weaker Q-band in the region of 450-750 nm, which include a plateau at λ=450-615 nm with small peaks at 504, 533 and 599 nm, and also high-intensity peak at λ=653 nm. It should be noted that the penetration depth of light is limited by absorption and scattering in tissue [15]. Besides, the Ce_6 line shift to the long-wavelength region increases tissue permeability for visible light and at the same time reduces light absorption by blood pigment at 500-600 nm. All of these play an essential role for increase of PDT effectiveness [9].

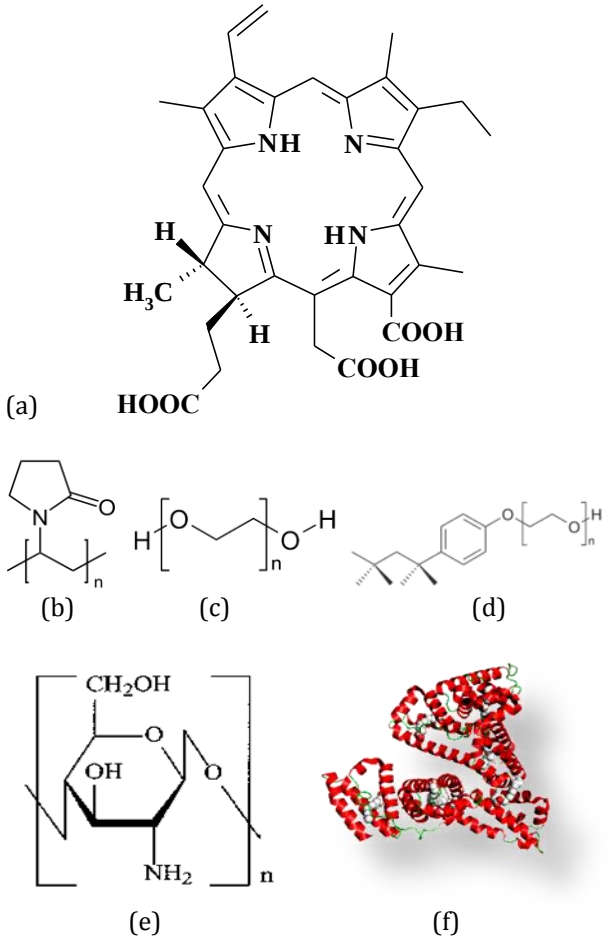

Fig. 1 Structures of chlorin e_6 (a), poly-N-vinylpyrrolidone (b), polyethyleneglycol (c), Triton X-100 (d), chitosan (e), bovine serum albumin (f).

When studying spectral properties of all presented supramolecular systems based on Ce_6, the hypsochromic shift in the field of Soret peak wasn't revealed (Fig. 2). According to the ideas of spectral shifts in biopolymers [12], the hypsochromic shift is connected with the transition of chromophore to more polar environment, and in our case, polar aqueous solvent. Absence of hypsochromic shift in the field of Soret peak testifies the identical hydrophobic behavior of all supramolecular systems, similar to hydrophobic behavior of Ce_6.

As illustrated in the Fig. 2, a small shift of Soret band to the long-wavelength region of optical

absorption spectra of Ce_6-PVP and Ce_6-BSA systems by 2 and 5 nanometers, respectively, in comparison to one of Ce_6, is observed. Besides, some broadening of spectral band can be seen for the Ce_6 – PVP system. The system of Ce_6 – PEG shows a sharp splitting of Soret band with a form of Gaussian distribution and broadening by $\Delta\lambda^{1/2}_{Soret}$ =13%. On the basis of absorbency fall in the region of Soret band for all systems and according to [16] one can say of single oxygen formation in all presented supramolecular systems. Besides, hypsochromic effect can be connected with the strengthening of intermolecular interactions (including interactions between the chromophores which are in more ordered form in comparison with the free state), and, as a result, the formation of molecular complexes takes place. This statement is consistent with the conclusions made by the authors of [5, 12], showed that, upon interactions, Ce_6 forms complexes with PVP. Moreover, the results of [17, 18] devoted to the investigation of porphyrines-serum albumin systems also confirm our hypotheses.

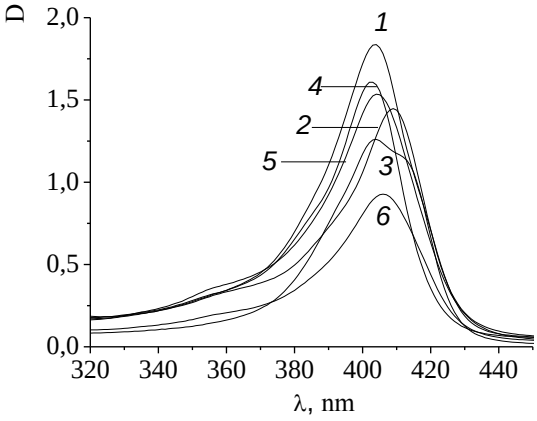

Fig. 2 Absorption spectra of supramolecular systems based on Ce_6 ($2\cdot10^{-5}$ M) in the region of the Soret peak: *1* - Ce_6 in aqueous solution, *2* - Ce_6-BSA, *3* - Ce_6-PEG, *4* - Ce_6-chitosan, *5* - Ce_6-TX-100, *6* - Ce_6-PVP.

Optical absorption spectra (Q-band region) of supramolecular systems based on Ce_6 ($2\cdot10^{-5}$ M) in various excipients are shown in Fig. 3. When comparing the received data with the data for Ce_6 aqueous solution, we have revealed that in a case of chitosan, PVP, TX-100 and BSA addition to Ce_6 the maximum of long-wavelength Q-band absorption (λ = 653 nm) undergoes bathochromic shift (1 nm, 10 nm, 12 nm and 13 nm, correspondingly), whereas in the Ce_6 – PEG system the hypsochromic shift of the Q-band maximum (14 nm) is observed. As a result, the maximum of Q-band absorption changes in row: PEG (639 nanometers) < chitosan (654 nm) < PVP (663 nm) < TX-100 (665 nm) < BSA (666 nm). Thus, absorption maximum shift to the red region of spectrum demonstrates that when performing photodynamic therapy with the systems having PVP, TX-100 and BSA as excipients there is a high probability of penetrating light absorption and big prospects for invasion these systems through tissues in comparison with Ce_6.

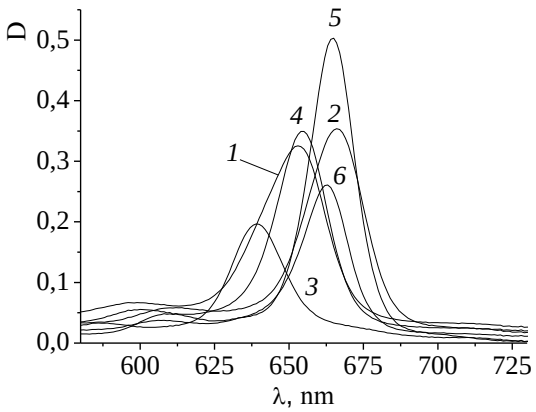

Fig. 3 Absorption spectra of supramolecular systems based on Ce_6 ($2\cdot10^{-5}$ M) in the region of the Q-band: *1* - Ce_6 in aqueous solution, *2* - Ce_6-BSA, *3* - Ce_6-PEG, *4* - Ce_6-chitosan, *5* - Ce_6-TX-100, *6* - Ce_6-PVP.

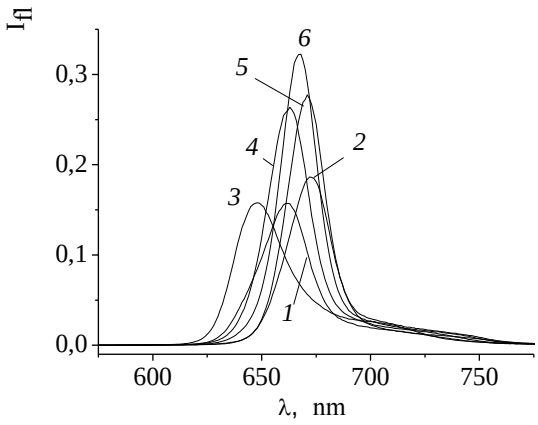

Fig. 4 Fluorescence spectra of supramolecular systems based on Ce_6 ($2\cdot10^{-5}$ M): *1* - Ce_6 in aqueous solution, *2* - Ce_6-BSA, *3* - Ce_6-PEG, *4* - Ce_6-chitosan, *5* - Ce_6-TX-100, *6* - Ce_6-PVP.

The spectral changes in the Q-band region of absorption spectrum connected with the bathochromic shift of a long - wavelength absorption band of a sensitizer and essential reduction of half-width of a line also demonstrate disaggregation of Ce_6 molecules, their interaction with excipients in solutions and formation of a molecular complex. The appearance of a porphyrine molecular complex with TX-100, BSA and PVP absorption band at 615 nm (Fig. 3) is the confirmation of this assumption. Moreover, the disappearance of absorption in the region of 680-700 nm for Ce_6 – PEG system, specific for porphyrine aggregates, is also the confirmation of the porphyrine aggregates destruction and transition of a PS to molecular associates, and at a later stage, possibly, molecular complexes [17].

The specific characteristic of fluorescence spectra of all supramolecular systems is their overlap with Q-band of absorption spectra (Fig. 4), that allows considering the formed molecular associates and complexes as donors of photoexitation energy for Ce_6 molecules. As can be seen from the Fig. 4, the addition of all studied excipients into Ce_6 aqueous solution leads to the increase of fluorescence intensity of Ce_6. The greatest increase in fluorescence intensity is observed in the presence of PVP. Moreover, the determined by a relative method [13] (the free form of the dye in the absence of the enzyme was as a standart with $\varphi_0 = 0.15$) quantum yield φ_k of the fluorescence is depends on the excipients, changing from 0.12 for TX-100 and 0.13 for chitosan to 0.16, in PEG and PVP. Such supramolecular compound as Ce_6-BSA shows the value of the fluorescence quantum yield as 0.15 equal to the fluorescence quantum yield for Ce_6.

Some increase in φ_k value for Ce_6 – PEG and Ce_6 – PVP in comparison with φ_k value for Ce_6 aqueous solution confirms the data of optical absorption spectra and demonstrates consecutive destruction of Ce_6 aggregates and a complex formation. It should be noted that aggregates degradation rate in the aqueous environments is various in the presence of different excipients. Probably, the calculated for Ce_6-BSA system value of a quantum yield, equal to the same value for Ce_6, can be explained by this. Low φ_k value for Ce_6 – TX-100, possibly, is connected with the partial aggregation of a pigment which is due to low solubility and the formation of another type complex characterized by a low fluorescence quantum yield. As far as fluorescent characteristics of the Ce_6 – chitosan system, it is seen that they remain almost invariable in comparison with similar characteristics of Ce_6 aqueous solution, and some decrease in φ_k is explained, perhaps, by aggregation of dye in solution that reduces photochemical activity of a PS.

With the help of the method of "chemical traps" the registration of singlet oxygen was carried out. From this, one can assume that as a part of the supramolecular complexes, Ce_6 is an effective photosensitizer of singlet oxygen generation with a quantum yield 0.53 (Ce_6-PVP), 0.50 (Ce_6-PEG), 0.62 (Ce_6-TX-100) and 0.56 (Ce_6-BSA).

4 Conclusion

To sum up, the conducted study of spectral and fluorescent characteristics of various supramolecular systems on the basis of chlorin e_6 allows us to conclude promising method of controlled aggregation of photosensitizers in the composition of supramolecular complexes to create medicines of predictable photodynamic activity. The obtained Q-band absorption maxima are in a row: PEG (639 nanometers) < chitosan (654 nm) < PVP (663 nm) < TX-100 (665 nm) < BSA (666 nm), which clearly demonstrates the disaggregation of Ce_6 molecules in systems with TX-100, BSA and PVP. The appearance of a porphyrine molecular complex absorption band at 615 nm for Ce_6-TX-100, Ce_6-BSA and Ce_6-PVP systems also shows the Ce_6 molecules disaggregation. As far as Ce_6-PEG system, the absence of absorption in the region of 680-700 nm testifies the porphyrine aggregates destruction. In addition, the obtained from fluorescence spectra value of φ_k=0.16 for Ce_6 – PEG is consistent with the absorption data and confirms the appearance of disaggregated Ce_6 molecules fraction. A quantum yield of singlet oxygen generation falls in the range from 0.5 for PEG up to 0,62 for TX-100. According to [5], values received are close or exceed the corresponding value for chlorin e_6 in the aqueous solution (0.5±0.05 at the medium of pH 6.3), which confirms the assumption on the disaggregating action of excipients.

Though, the presented systems call for the further investigations, spectral and fluorescence data clearly demonstrate the absence of aggregation in such systems as Ce_6-PVP, Ce_6-PEG, Ce_6-BSA and Ce_6-TX-100 and the prospects of use of these systems for diagnostics (and, as possible, therapy) are evident.